UNIVERSITAT DE BARCELONA

Implications of phase coexistence in VO_2 thin-films across the metal-insulator transition

Laura Rodríguez Domínguez

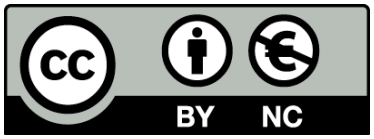

Tesi doctoral

Implications of phase coexistence in VO_2 thin-films across the metal-insulator transition

Laura Rodríguez Domínguez

UNIVERSITAT DE BARCELONA

Implications of phase coexistence in VO_2 thin-films across the metal-insulator transition

Programa de doctorat en Nanociències

Autora:

Laura Rodríguez Domínguez

Directors:

Prof. Gustau Catalan Bernabé

Dr. José Santiso López

Tutor:

Prof. Manuel Varela Fernández

Institut Català de Nanociència i Nanotecnologia

UNIVERSITAT DE BARCELONA

This work was supported from the Spanish Ministry of Economy, Industry and Competitiveness (project: MAT2016-77100-C2-1-P). ICN2 is funded by the CERCA programme/Generalitat de Catalunya and by the Severo Ochoa programme (SEV-2017-0706).

ABSTRACT

A Metal-insulator transition (MIT) is the ability of some materials to change between metal and insulator electric behaviours as a function of some external stimuli such as temperature, stress, voltage, magnetic field or light. The Fermi level position with respect to the band structure determines one character or the other, and in some materials this band structure is very sensitive to electron-electron correlations, whereby Coulomb repulsions rule the distribution of electrons within the orbitals (like Hund's rules) as well as the hop of electrons between atoms that, in the end, defines the material's electronic characteristics and charge transport –and the Mott insulator concept. This is the case of some transition metal oxides, which despite having partially filled bands allowing, in theory, metallic conduction, electron-electron interactions are strong enough to split the half-filled band in a lower energy band that is full first and a higher energy sub-band still empty, resembling an insulator.

An archetypical example of this is vanadium dioxide (VO_2), a system with a $3d^1$ electronic configuration –from the $4s^2$ $3d^3$ of V, which leads to a first-order MIT in the oxide. Although there are other materials (inorganic but also organic) presenting MITs, VO_2 is a reference in this topic mainly because the electronic switch happens near room temperature (~68 ºC) with a change in conductivity of several orders of magnitude and it is accompanied by a structural phase transition (SPT) that occurs simultaneously. This duality results in a high-temperature state given by a metallic rutile (tetragonal) phase that turns into a Mott insulator (semiconductor) with monoclinic M1 structure at the low-temperature state. Thus, the electronic and structural elements of the transition in VO_2 are tightly entangled. The Mott-Hubbard and Peierls models explain the electric and structural transitions respectively, and in both cases, the key resides in energy instabilities at the shortest V-V chains –along the c_R-axis of the rutile structure (or the a_{M1}-axis in M1). The debate of which mechanism triggers first

the MIT in VO_2 is still controversial, reason why there are works claiming a Mott, Peierls or a collaborative Mott-Peierls transition.

Mechanical stress induces lattice deformations in the crystal that distort the surroundings of V atoms (V-O in oxygen octahedron and V-V bonds). This affects the orbital properties within the unit cell (overlapping, occupancy, shape, etc.), and also the lattice's electrostatic potential field and vibrational modes. Therefore, the energy gap of either the electronic or the structural instabilities could be overcome/activated to induce the VO_2 transition. At the same time, mechanical stress is all but inevitable in thin films, where growth on lattice-mismatched substrates induces biaxial strains that modify the phase stability of the films. In recent times, epitaxial strain has gradually been turned from a nuisance into a tool for exploring and modifying the film's properties (not just in VO_2 but in other complex oxides as well), in so-called "strain engineering".

This epitaxial strain engineering is already a mature discipline for some families of oxides, notably those with the perovskite structure, where there is a large variety of substrate and film materials that share the same pseudo-cubic lattice structure and can be carefully matched to continually and predictably tune the strain-induced properties. By contrast, in binary oxides such as VO_2 there are fewer substrate options, and in addition, strongly correlated electron systems are not easily amenable to first-principles calculations, all of which has conspired to make our understanding of the effect of strain on VO_2 films less complete than would be the case for perovskites. It is in this context that the present work is located.

This thesis explores in detail the consequences of in-plane tensile strain in epitaxial VO_2 thin films grown on rutile (001)-oriented TiO_2 substrates by the pulsed laser deposition (PLD) technique, how the strain relaxes as film thickness increases, and how the strain relaxation itself gives raise to new phases and phase coexistence phenomena of interest. What makes this work novel with respect to other strain studies is the focus on the relation between local

properties and global behaviour. As the thesis will show, space-averaged measurements of transport properties or X-ray diffraction (XRD) can miss out on a lot of interesting and important physics that happens on a local, nanoscopic level, including nano-tweeds or phase coexistence in the form of metal-insulator (M-I) phase boundaries. This work has used various microscopy techniques effective at different scales, from optical microscopy (micron scale) to scanning-probe microscopy (nanoscale) to transmission electron microscopy (atomic scale), yielding a very complete picture of the MIT in strained VO_2 films across the different scales.

After a brief introductory chapter contextualizing the thesis, chapter one describes the growth and average structural characteristics of the films, including their strain relaxation and the samples' evolution due to aging. In order to control strain in our films (in-plane tensile strain inducing out-of-plane c_R-axis compression), it was grown a thickness set from ~2 nm up to ~150 nm –being the samples useful only from ~5 to 120 nm (below 5 nm the MIT was not clearly defined and below 120 nm the films peeled off). Surprisingly, the films do not relax with thickness neither conventionally nor progressively, resulting in crack formation, M-I phase separation toward the cracks and strong-strain gradients within the film related to structural deformations, and phase coexistence. This phase coexistence is explored in detail in subsequent chapters.

The microstructure far from crack-edges (and therefore in the more strained parts of the film) is presented in chapter two. It shows that the strained VO_2 regions, despite showing a seemingly metallic rutile phase in macroscopic measurements (transport and x-ray diffraction), are not stabilized in the standard high-temperature rutile phase but in a metrically tetragonal structure that triples the rutile periodicity with monoclinic (2/m) symmetry. Moreover, the orientational variants of this new phase (x3M) coexist forming tweed patterns of few nanometers in size.

Chapter three explores the functional consequences of the coexistence between strain-relaxed insulating phase near the films' cracks and metallic phase away from them. The peculiar pattern induced by strain-induced crack formation leads to the introduction of the concept of "self-pixelation", whereby each island of VO_2 bounded by insulating cracks behaves de facto as a "pixel" whose MIT can be individually triggered independently of the rest of the film.

Finally, the last chapter contains the general conclusions and outlook for future work. Some of the topics that are touched include the collective dynamics of the phase transition, with emerging evidence for avalanche phenomena, and the possibility of using thickness gradients as a way to stabilize and study static phase boundaries in thin films. The study of the interface between M-I nanoregions was in fact one of the driving forces of this thesis, as it is worth exploring both from fundamental and functional points of view: a metal-semiconductor junction defines an electrostatic potential barrier known as a Schottky barrier leading to many useful applications such as diodes in conventional electronics, and materials having a MIT give the chance of scaling these junctions to nanoscopic sizes. Compressive strain along the c_R-axis of VO_2 lowers the temperature of the MIT (T_{MIT}) and, strain relaxes with thickness, meaning that thickness gradients offer an alternative way to stabilize the M-I phase boundary that was already observed near the strain-relaxed (near-crack) areas of our films.

The experimental conditions used along this thesis are included as annexes at the end of the manuscript. These include details of the X-ray diffraction (XRD) equipment to measure around the symmetric 002_R and asymmetric $\bar{1}\bar{1}2_R$ reflections of the rutile (R) TiO_2(001) substrate; X-ray reflectivity (XRR) to estimate thicknesses, transmission electron microscopy (TEM) and micro-Raman spectroscopy to study local symmetry. The features of the samples' surface were checked by atomic force microscopy (AFM) and at some few cases, complemented with scanning electron microscopy (SEM). Local electrical properties such as

work function, conductivity and current-voltage curves were probed by AFM electrical modes: scanning Kelvin probe microscopy (SKPM) and conducting AFM (CAFM), respectively. Temperature-dependent macroscopic electrical features were measured by 4-probe methods and optical microscopy was also used as a tool to preview the M-I state of the samples (optical transmission is very different for the metallic and insulating phases of VO_2).

Most of the published works on the stress-induced MIT have focused on the engineering of VO_2 properties or their characterization. This includes also part of this thesis. However, based on my own experience during this doctoral research I feel it is important to also report and expose all the problems and technical difficulties inherent in achieving pure highly coherent VO_2 films. For this reason, I have also wanted to highlight these less glamorous issues in my thesis, in the hope that they will help future scientists, students or interested in getting started in research on VO_2 thin films.

RESUM

Una transició metall-aïllant (MIT) es la habilitat d'alguns materials per canviar el seu comportament elèctric de metall a aïllant en funció d'estímuls externs com la temperatura, estrès, voltatge, camp magnètic o la llum. La posició del nivell de Fermi respecte a l'estructura de bandes determina un o altre caràcter, i en alguns materials aquesta estructura de bandes és molt sensible a correlacions entre electrons, fent que les repulsions coulombianes governin la distribució d'electrons dins dels orbitals (com descriurien les regles de Hund) i els salts d'electrons entre àtoms que, al final, és el que acabarà definint l'estat de conducció del material –i el concepte d'aïllant tipus Mott. Aquest és el cas d'alguns òxids de metalls de transició, els quals malgrat tenir bandes d'energia parcialment ocupades permetent, en teoria, conducció metàl·lica, les interaccions electró-electró són prou fortes com per dividir aquesta banda parcialment ocupada en una d'energia més baixa que s'omple primer i una altra banda d'energia major que queda buida, semblant a un aïllant.

Un exemple d'això és el diòxid de vanadi (VO_2), un sistema amb una configuració electrònica $3d^1$ –que prové dels $4s^2$ $3d^3$ del V, portant l'òxid a una MIT de primer ordre. Tot i haver altres materials (inorgànics però també orgànics) que presenten MITs, l'VO_2 és un referent en aquest tema bàsicament perquè el canvi de fase electrònic succeeix a prop de temperatura ambient (~68 ºC) amb un canvi de conductivitat de varis ordres de magnitud, produint-se també una transició de fase estructural (SPT) simultàniament. Aquesta dualitat resulta en un estat d'alta temperatura metàl·lic amb estructura rutil (tetragonal) que es transforma en un aïllant de Mott (semiconductor) amb estructura monoclínica M1 en el seu estat de baixa temperatura. Per tant, els elements electrònics i estructurals de la transició al VO_2 estan estretament entrelligats. Els models de Mott-Hubbard i Peierls expliquen la transició electrònica i estructural respectivament, i en ambdós casos, la clau resideix en inestabilitats

energètiques a les cadenes de V-V més curtes –al llarg de l'eix c_R de l'estructura rutil (o de l'eix a_{M1} a l'M1). El debat sobre quin és el mecanisme que inicia la MIT del VO_2 encara es obert, raó per la qual hi ha treballs que proclamen un transició de Mott, de Peierls o una contribució de les dues.

L'estrès mecànic indueix deformacions a la xarxa del cristall que distorsiona els voltants dels àtoms de V (enllaços V-O als octaedres d'oxygens i els V-V). Això afecta les propietats orbitals dins de la cella unitat (hibridació, ocupació, forma, etc), així com al camp de potencial electrostàtic i modes vibracionals. Per tant, el salt d'energia que genera la inestabilitat tant electrònica com estructural podria ser sobrepassat/activat per induir la transició del VO_2. Al mateix temps, l'estrès mecànic en capes primes és inevitable, on el creixement sobre substrats amb diferent paràmetre de xarxa hi indueix una deformació biaxial que modifica la fase estable de les pel·lícules. Recentment, l'enginyeria de deformacions per epitàxia s'ha convertit en una eina per explorar i modificar les propietats de les pel·lícules (no només en VO_2, sino en altres òxids complexos també).

Aquesta enginyeria epitaxial ja és una disciplina ben establerta per algunes famílies d'òxids com són els d'estructura perovskita, on hi ha una gran varietat de substrats i materials en capa prima amb la mateixa estructura pseudo-cúbica, trobant un ajust continu en les propietats induïdes per la tensió a la xarxa. En canvi, en els òxids binaris tals com en l'VO_2 hi ha menys opcions de substrat en aquest sentit, on s'hi afegeix el fet de que els sistemes d'electrons altament correlacionats no son fàcils de modelitzar per càlculs teòrics, la qual cosa fa més difícil entendre l'efecte de la tensió en capes de VO_2 que en el cas de les perovskites. És aquest el context en el que es troba el treball present.

Aquesta tesi explora en detall les conseqüències de la tensió en el pla, en capes primes epitaxials de VO_2 crescudes sobre substrats rutil de TiO_2 orientats en (001), per la tècnica de dipòsit de làser polsat (PLD), així com la tensió es relaxa a mida que augmenta el gruix de les

pel·lícules, i com la pròpia relaxació dóna lloc a noves fases i a la fenomenologia pel fet de d'estar en coexistència. El que fa que aquest treball sigui diferent respecte la resta d'estudis amb estrès mecànic és la focalització en la relació que hi ha entre propietats locals i comportament global del material. Com es mostrarà a la tesi, mesures espacials mitjana de transport elèctric o de difracció de rajos-X (XRD) poden perdre's un munt de processos físics importants que ocorren en escala local, a nivell nanoscòpic, on s'inclouen nano-tweeds o coexistència de fases en forma de fronteres metall-aïllant (M-I). Les he caracteritzat amb varies microscòpies a diferents escales, des de microscòpia òptica (microescala) a microscòpies de sonda de rastreig (nanoescala) a microscòpia de transmissió d'electrons (escala atòmica), aconseguint una visió completa de la MIT in capes tensionades de VO_2 al llarg de les diferents escales.

Després d'un curt capítol introductori contextualitzant la tesi, al capítol u es descriu el creixement i mitjana de les característiques estructurals de les capes, incloent la seva relaxació de tensió i l'evolució de les mostres degut a "envelliment". Per tal de controlar la tensió en les nostres capes (tensió en el pla que indueix compressió en la direcció fora del pla, al llarg de l'eix c_R), s'ha crescut un conjunt de mostres variant el gruix des dels ~2 nm fins a ~150 nm –sent només d'interès les mostres entre ~5 i 120 nm (per sota de 5 nm la MIT no era definida i per sobre de 120 nm les capes s'escamaven). Sorprenentment, les pel·lícules ni relaxen amb el gruix ni ho fan progressivament o de forma convencional, el que dóna lloc a formació de cracks, separació de fases M-I al voltant dels cracks, i forts gradients de relaxació de tensió dins la capa relacionats amb deformacions estructurals, i amb la coexistència de fases. Aquesta coexistència de fases s'explora en detall en els capítols subseqüents.

La microestructura lluny de la bora dels cracks (i per tant a les parts més tensionades de la pel·lícula) es presenta en el capítol dos. Es mostra que les regions de VO_2 tensionat, malgrat veure aparentment la fase rutil metàl·lica en mesures macroscòpiques (transport i

difracció de rajos-X), no és estabilitzada en la fase rutil estàndard d'alta temperatura sino que ho fa en una estructura amb mètrica tetragonal que triplica la periodicitat del rutil fent ús d'una simetria monoclínica (2/m). A més, les diferents orientacions d'aquesta nova fase (x3M) coexisteixen formant un patró tipus tweed de uns pocs nanòmetres de tamany.

El capítol tres explora les conseqüències funcionals de la coexistència entre la fase aïllant més relaxada a prop dels cracks i la fase metàl·lica lluny d'ells. El peculiar patró induït per la formació de cracks (que és al seu cop induïda per la tensió a la capa) ens porta al concepte d' "auto-pixel·lació", on cada illa de VO2 delimitat per cracks aïllants es comporta en realitat com a un píxel, la MIT del qual pot ser activada de forma individual i independent de la resta de la pel·lícula.

Finalment, l'últim capítol conté les conclusions generals i la perspectiva de treball futur. Alguns dels temes tractats inclouen la dinàmica col·lectiva de la transició de fase, amb evidències emergents de fenòmens d'avalanxa, i la possibilitat d'utilitzar gradients de gruix com a mètode per estabilitzar i estudiar parets de fase estàtiques en capa prima. L'estudi de la intercara entre nanoregions M-I va ser en realitat una de les motivacions d'aquesta tesi, ja que val la pena d'explorar tant des d'un punt de vista fonamental com funcional: una unió metall-semiconductor defineix una barrera de potencial electrostàtic coneguda com a barrera Schottky que porta moltes aplicacions d'èxit en l'electrònica convencional tals com díodes, i materials que presentin MIT obren oportunitats a escalar aquestes unions fins mides nanoscòpiques. Compressions de l'eix c_R del VO_2 fan disminuir la temperatura de la MIT (T_{MIT}), i la tensió relaxa amb el gruix, volent dir que els gradients de gruix ofereixen una alternativa per estabilitzar les fronteres de fase M-I que s'han observat a prop de les àrees més relaxades (a prop dels cracks) de les nostres capes.

Les condicions experimentals utilitzades al llarg de la tesi estan incloses a l'annex que hi ha al final del manuscrit. Aquestes contenen els detalls de l'equip d'XRD amb el que s'ha mesurat al voltant de les reflexions simètrica 002_R i asimètrica $\overline{1}\overline{1}2_R$ dels substrats TiO_2(001)

rutil; de la reflectivitat de rajos-X (XRR) per estimar els gruixos, de la microscòpia de transmissió d'electrons (TEM) i de l'espectroscòpia de micro-Raman pels estudis locals de simetria. La superfície s'ha caracteritzat amb microscòpia de força atòmica (AFM) i en alguns pocs casos, complementat amb microscòpia de rastreig d'electrons (SEM). Propietats electròniques locals tals com la funció de treball, conductivitat i corbes de corrent-voltage s'han fet amb modes elèctrics d'AFM: microscòpia de rastreig de sonda Kelvin (SKPM) i conducció AFM (CAFM), respectivament. Mesures elèctriques macroscòpiques dependents de la temperatura s'han fet amb mètode de 4-puntes, i també s'ha utilitzat microscòpia òptica com a eina per visualitzar l'estat M-I de les mostres (la transmissió òptica del VO_2 en fase metàl·lica és molt diferent a la de la fase aïllant).

La majoria de treballs publicats sobre la MIT induïda per estrès s'han centrat en l'enginyeria de les propietats del VO_2 o en la seva caracterització, on també s'inclou part d'aquesta tesis. Tot i així, basant-me en la meva pròpia experiència durant aquesta recerca doctoral, crec que també és important explicar tots els problemes i dificultats tècniques inherents en l'obtenció de capes pures, altament coherents d'VO_2. Per aquest motiu, també he volgut subratllar a la meva tesi aquestes qüestions no tant atractives, amb l'esperança de que siguin útils per a futurs investigadors, estudiants o interessats en començar amb la recerca de VO_2 en capa prima.

INTRODUCTION.

VO_2 structure and physical properties

Vanadium dioxide (VO_2) is a transition metal oxide referent of strong correlated materials due to its first-order metal-insulator transition (MIT) close to room temperature (RT) –this is, in bulk, at ~ 68 ºC. Below this critical temperature (T_c) VO_2 is a semiconductor with a band gap energy of ~0.6-0.8 eV [1-6], therefore insulating. Above T_c, the electronic behaviour turns into metallic and despite the small band gap, the change in resistivity is abrupt and large (from 3 to 5 orders of magnitude [7]), which results in important changes of its optical properties at the infrared range, making VO_2 promising not only for electronic devices but also in thermochromic applications [8-10] (figure I.1).

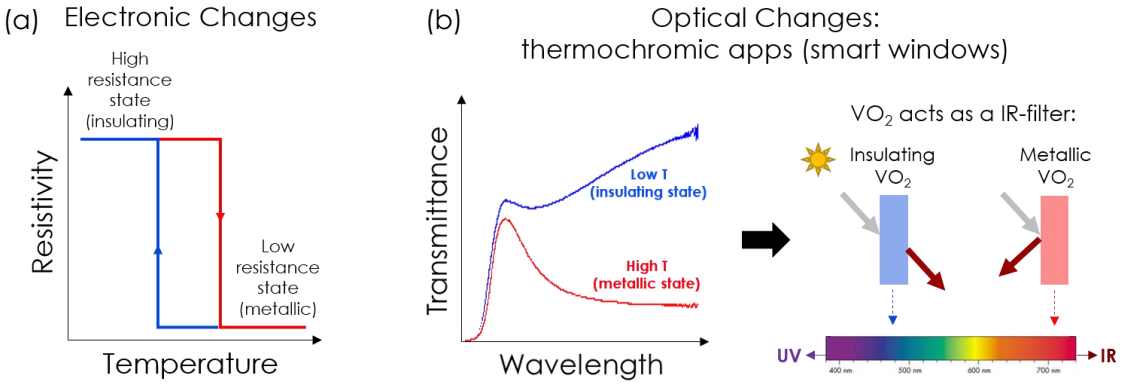

Figure I.1. Representation of electronic and optical changes of bulk VO_2 across its metal-insulator transition. Scheme of **(a)** change in resistivity with temperature and **(b)** change in optical transmittance depending on wavelength, at the high and low temperature (T) states (red and blue curves, respectively). Since metallic VO_2 blocks infrared light, it can be used in smart windows.

On the other hand, at the same time that the electronic transition takes place, a (displacive) structural phase transition (SPT) also occurs, from a monoclinic phase (M1, with space group $P2_1/c$) at the low-temperature insulating state to a tetragonal phase (rutile R with a space group $P4_2/mnm$) at the high-temperature metallic state (see figure I.2a). Rutile VO_2, which is the parent phase (thus, the highest symmetry), has straight equidistant V-V chains along its c_R-axis (|| a_{M1}-axis). However, they dimerize in M1, changing to zig-zag chains that deviates from the central position of rutile VO_6 octahedra columns, resulting in two distances

along the c_R direction –the short V-V distance forming the dimer and the long dimer-dimer distance (figure I.2b-c).

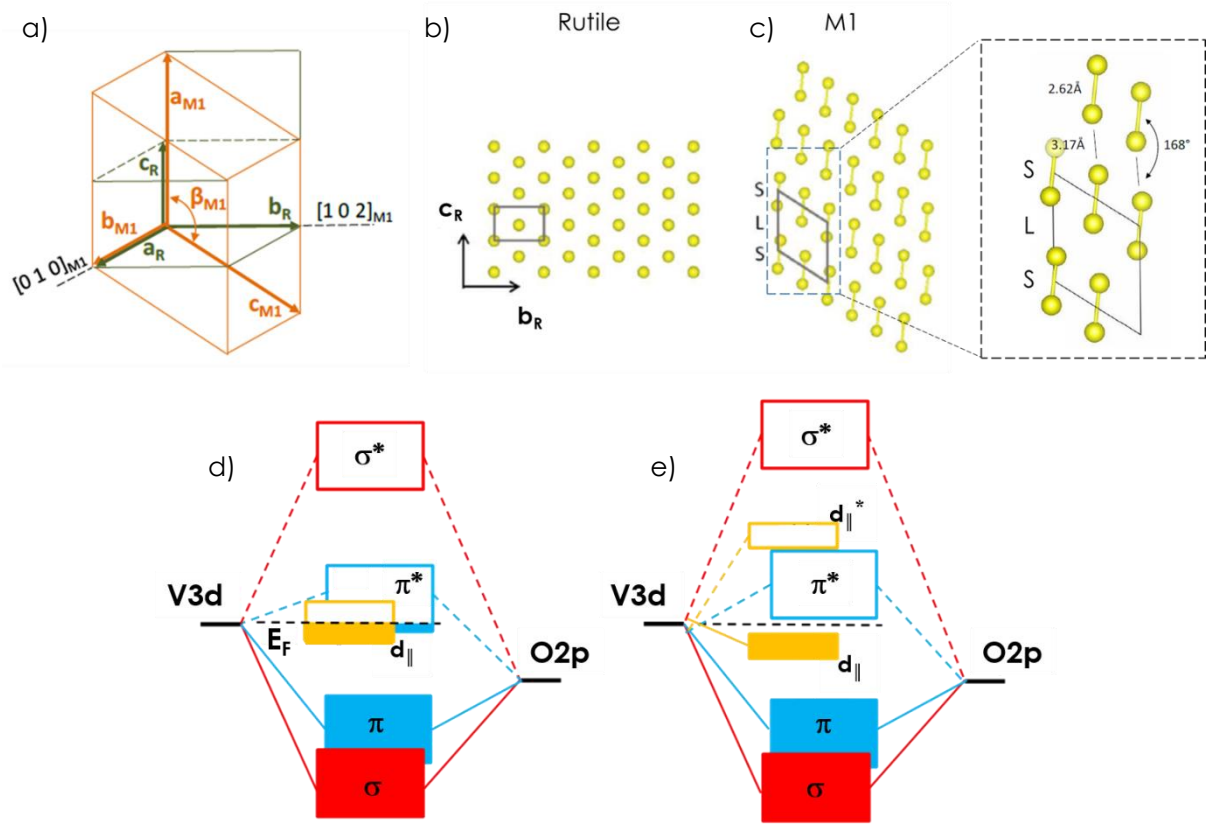

Figure I.2. Rutile and M1 VO_2 structures (modified from [11]). **(a)** Overlapped schemes of Rutile and M1 unit cells showing their equivalent directions and lattice vectors. Front-view of V-atoms in **(b)** rutile and **(c)** M1 structures. The inset details the short (S) and long (L) distances of the zig-zag V-V chains typical of M1. The band structure diagrams of the metallic **(d)** and insulating **(e)** states are depicted (modified from [12]).

The zig-zag distribution and length of these V-V distances define if electrons are localized within the crystal, and therefore, open the band gap energy (fig. I.2d-e). Hence, the origin of this electronic-lattice coupling relies on the orbital occupancy resulting from the dimerization state of the structure [2, 13-14]. However, the discussion about which mechanism starts the MIT is still open –Mott-Hubbard (electronic), Peierls (lattice) or a combined Mott-Peierls transition [3, 15-16].

Besides the stable M1 and R phases, VO_2 has other metastable polymorphs appearing under certain conditions like doping, strain, temperature or pressure. The most known are the monoclinic M2, triclinic T (sometimes treated as a distorted monoclinic named M3), monoclinic B and tetragonal A [17-22] –there is also an orthorhombic phase rarely mentioned, and in thin-films, a tetragonal-like and a new monoclinic phase which is the basis of chapter 2 (see table I.1).

Moreover, V adapts very well to the environment by changing its oxidation state (V metallic, +2, +3, +4, +5), which enlarges the family of V-oxides (VO_x) beyond the Magnéli Phases (V_nO_{2n-1}) [15, 24-26]. Therefore, since VO_2 has not the most stable oxidation state of vanadium at RT in air, it is likely its reoxidation to V_2O_5.

This scenario gives a clue about how difficult could be to stabilize VO_2 in a system where there is a large amount of phases in connection with the oxidation number (see, for instance, phase diagrams reported [10, 20, 22, 27]). Nevertheless, within the large family of V oxides, bulk VO_2 is the only compound undergoing a MIT close to room temperature [10, 26].

Table I.1. VO_2 polymorphs and their structural features reported in literature.

VO_2 Polymorphs found reported											
Structure	Common Labels	Space Group	a (Å)	b (Å)	c (Å)	α (°)	β (°)	γ (°)	V (Å^3)	ρ (g/cm^3)	ICSD Code/ Reference
Tetragonal	**R**	P42/mnm (136)	4.5546	4.5546	2.8514	90	90	90	59.15	4.66	4110
	A	P42/ncm (138)	8.4336	8.4336	7.6782	90	90	90	546.12	4.03	57155
		P4/nccZ (130)	8.4403	8.4403	7.6660	90	90	90	546.12	4.03	51213
		I4/m (87)	8.476	8.476	3.824	90	90	90	274.73	4.01	51214
Tetragonal-like	T-like or T	-	4.527	4.527	2.876	90	90	90	58.94	-	Qiu et al. [22]
Monoclinic	**M1**	P121/c1 (14)	5.755	4.525	5.386	90	122.61	90	118.15	4.66	602360
	M2	C12/m1 (12)	9.083	5.763	4.532	90	90.3	90	237.23	4.64	89470
		P12/m1 (10)	9.060	5.800	4.522	90	91.85	90	237.48	2.32	1503
	x3M	-	8.40	4.71	5.49	90	120.7	90	217.21	-	Sandiumenge et al. [11]
	B	C12/m1 (12)	12.030	3.693	6.420	90	106.1	90	274.03	4.02	199
Orthorhombic	-	Pbnm (62)	4.890	9.390	2.930	90	90	90	134.54	4.09	22303
		F222 (22)	13.015	12.597	5.795	90	90	90	950.09	4.64	34419
Triclinic	T	P-1 (2)	9.0600	5.7721	4.5203	89.99	91.4	89.83	236.32	2.33	1501

▪ OBJECTIVE AND APPROACHES

Although VO_2 has been (and still is) widely studied from many perspectives (from first principles to explain the MIT's physics to the most applicative research) the aim of this work was novel. So far, the main objective of previous (non-theoretical) investigations about VO_2 has been to study the material's response to different external stimuli, but less attention though, was paid on the phase coexistence itself. For this reason, the motivation of this thesis was to explore the functional properties of the metal-insulator phase boundaries of VO_2 at the nanoscopic and mesoscopic scales. Since a semiconductor-monoclinic region is completely different from a metallic-rutile region, one would expect to find new arrangements and/or behaviours to save the apparent discontinuity in this highly correlated scenario –analogously to domain walls in ferroelectrics.

Once defined the playground, we chose the players: among all the possible candidates known to trigger the MIT (such as magnetic field, electric field, optical excitation, stress, doping, etc. [10, 27-28]), the strategy here was to take advantage of epitaxial strain to control the T_c of the MIT. It is known that T_c decreases when a compressive stress is applied along the c_R direction of the V-V zig-zag chains, and contrary, T_c increases when these chains are elongated by tensile stress [29-30].

Using the appropriate substrate, T_c can be shifted towards RT, as requested for many applications. In addition, since strain may force the M1/R transition to pass through intermediate phases, it pairs with the interest of this thesis. As detailed in next chapter, the chosen morphology of the samples was thin-films and the substrate selected to grow them was rutile (R) titanium dioxide (TiO_2), isostructural with the high-temperature VO_2 parent phase. R-TiO_2, one of the typical substrates used to grow VO_2, has larger lattice parameters (see table I.2), thus, epitaxial VO_2 will always be in-plane tensile strained forcing the

compression along the out-of-plane direction, regardless of the substrate's orientation. For this reason, to decrease T_c of VO_2 down to room temperature (compressed c_R) the TiO_2 orientation must be (001), with a_R and b_R as elongated in-plane lattice parameters.

It is worth noting that, because of the different mismatch along the in-plane axes in M1, this configuration adds epitaxial strain across the R-to-M1 SPT, which has tremendous consequences explained in chapter one and two. At the high-temperature R-phase, the strain along the a_R and b_R axes is symmetric; however, this is not the case at the low-temperature M1-phase, where the strain along one of the in-plane axis is slightly larger (see table I.2).

Table I.2. Comparison of structural parameters between rutile TiO_2, rutile VO_2 and monoclinic M1 VO_2. The M1-phase lattice parameters are also expressed in terms of pseudo rutile unit cell, used to give the mismatch values.

		LATTICE PARAMETERS (Å)			ANGLES (°)			MISMATCH (%)	REFERENCE
	Space Group	a	b	c	α	β	γ	In-plane	ICSD Code
R-TiO_2	$P4_2/mnm$ (136)	4.594	4.594	2.959	90	90	90	-	23697
R-VO_2	$P4_2/mnm$ (136)	4.555	4.555	2.851	90	90	90	0.9	4110
M1-VO_2	$P12_1/c1$ (14)	5.743	4.517	5.375	90	122.61	90	+1.7(b_{M1}); +1.4(c_{M1})	15889
(in pseudo-R cell)		4.517	4.528	2.872					

This fact could be contributing (if not the reason) to the gradual transformation across the SPT through the mentioned intermediate phases upon strain conditions, especially in our films where, surprisingly, there is no strain-relaxation as thickness increases (see table I.3 and figure I.3). It is common that strained films relax with thickness progressively by forming misfit dislocations above a certain critical thickness –as a mechanism to release the stored elastic energy.

However, this is not what seems to happen in our samples, which are epitaxial (see chapter 1). Table I.3 contains the mean value and its standard deviation of the structural parameters appearing in figure I.3a-b, measured by XRD. These values are compared with a

rutile VO_2 bulk (relaxed) reference from the ICSD database (code 4110), and the strain mean value of our samples was calculated with respect to that reference. The structural parameters of our films (which are the c_R and a_R lattice parameters, their c_R/a_R ratio, and the $\bar{1}\bar{1}2_R$ interplanar distance) were obtained at room temperature, from reciprocal space maps (RSMs) around the $\bar{1}\bar{1}2_R$ reflection of the substrate, within a thickness range from ~ 10 to 120 nm. As an example, fig. I.3c-d shows the RSMs of thinnest and thickest films, where a white dashed line links the two RSMs by the substrate's peak position.

Table I.3. Comparison of relaxed and strained rutile VO_2 structural parameters. Relaxed values were taken from the ICSD database (code 4110) as reference. The experimental mean values of c_R (out-of plane) and a_R (in-plane) lattice parameters, and the $\bar{1}\bar{1}2_R$ interplanar distance, were calculated from data of fig. I.3a-b.

	R-VO_2 (ref.)	VO_2 films (experimental)		Strain (ε)
	ICSD 4110	mean value	st. Dev	$\varepsilon_\perp/\varepsilon_\parallel$
c_R (Å)	2.8514	2.8496	0.0138	0.0841
a_R (Å)	4.5546	4.5888	0.0086	
c_R/a_R	0.6260	0.6210	0.0035	
$d(\bar{1}\bar{1}2)_R$ (Å)	1.3037	1.3046	0.0052	

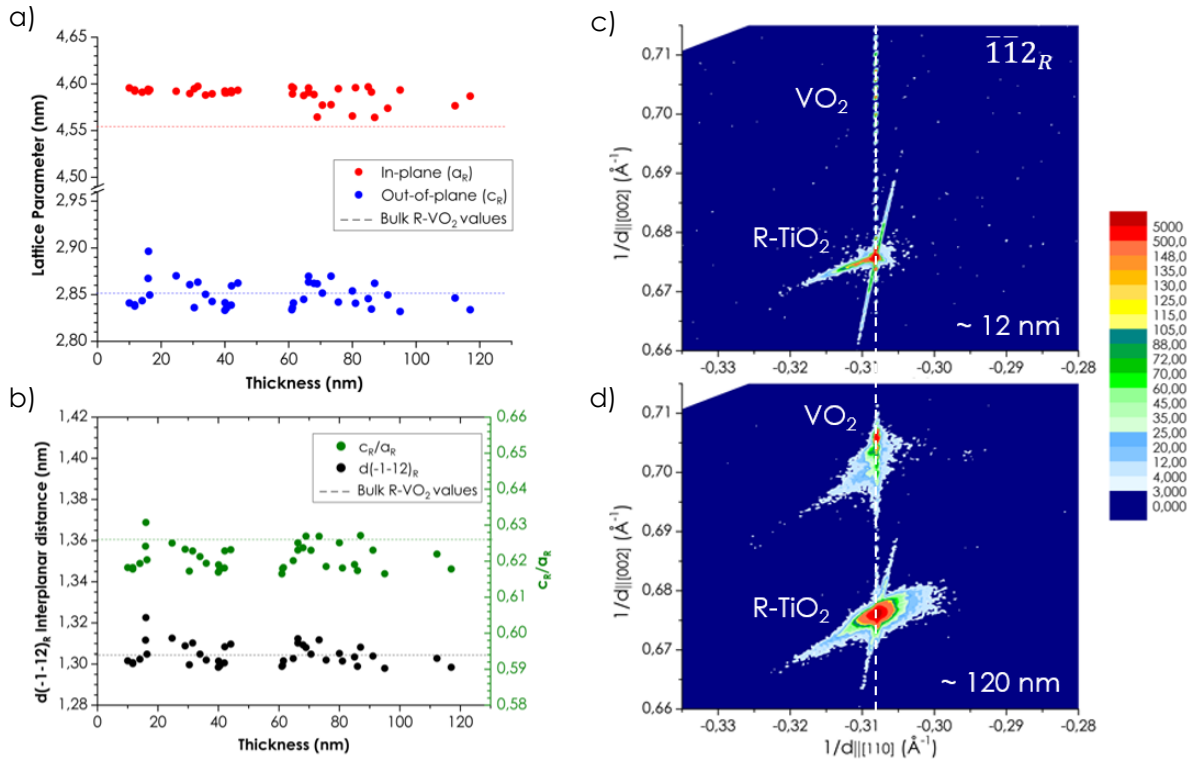

Figure I.3. Structural parameters of our VO_2 films versus thickness, calculated in terms of rutile structure, from the position of the VO_2 peak present at the RSMs around the $\bar{1}\bar{1}2_R$ reflection of rutile TiO_2(001). **(a)** Experimental a_R in-plane (red dots) and c_R out-of-plane (blue dots) lattice parameters of some of our films. Dashed lines mark the rutile VO_2 bulk reference values. Values above the references reveal tensile strain, while below means compressive strain along that direction. **(b)** Representation of the c_R/a_R lattice parameters ratio (green dots) and the experimental $\bar{1}\bar{1}2_R$ interplanar distance (black dots). Dashed lines mark the rutile VO_2 bulk reference values. Two RSMs of films of **(c)** ~12 nm and **(d)** ~120 nm thick, show the VO_2 fully in-plane tensile strained. A white dashed line aligns the TiO_2 peaks to ease the comparison of the VO_2 peaks position in the maps.

One can see that the maximum intensity position of the rutile VO_2 peaks are perfectly aligned with the substrate, meaning that they are mostly in-plane fully tensile strained. In fact, as revealed by fig. I.3a-b, the structural parameters are quite constant around their mean values. Hence, they do not show any dependence with thickness (dashed lines mark the rutile VO_2 bulk reference values).

Such large amount of stored elastic energy, especially in thicker films, must be released somehow, and as explained in next chapters, this is by cracks formation and settling a new phase, which is arranged at the nanoscale, undistinguishable by conventional average techniques. Our measurements were performed by standard techniques commonly used to characterize thin films. For instance, atomic force microscopy (AFM) and scanning electron microscopy (SEM) to check the surface of the samples; raman, X-ray diffraction (XRD) techniques and transmission electron microscopy (TEM) to determine the structure in average and at the atomic scale; X-ray photoelectron spectroscopy (XPS) to ensure the V^{+4} oxidation state of vanadium; scanning Kelvin probe microscopy (SKPM) and conducting AFM to study the local electronic properties; 4-wire macroscopic electrical transport to monitor the MIT; and last but not least, optical microscopy, which by changes in optical density and birefringence, allows to identify in a glance the electronic state [31] of the film, changes in structure and density of cracks.

Unfortunately, it was not possible to find an appropriate technique with enough spatial resolution to characterize locally and systematically "phase walls" as entities in VO_2 films. Nevertheless, this work gives a comprehensive view of their footprint, suggests a conceptual application and exposes the difficulties of growing and working with this promising material in presence of strain, which is the key of both, the pros and cons of VO_2 thin films.

CHAPTER 1.

Film growth and crystal structure

1.0. INTRODUCTION

Since the metal-insulator transition (MIT) of VO_2 was predicted by Mott in 1949 [32] and reported by Morin in 1959 [33], mounting interest around the inherent properties of this material has led to the use of many different fabrication methods to obtain different VO_2 morphologies from bulk single crystals and ceramic material, to thin films and nanoobjects. Nano [34-40]/microbeams [41], nanoplatelets [31], needle-like nanocrystals [42-43], membranes [44], microcantilevers [45] and specially films [46-51] are the most common morphologies reported in literature, and the diversity of results depending on their geometrical constraints demonstrates that boundary conditions in VO_2 can determine the phase stability as well as the MIT path to follow.

Despite of being a first order transition, the high and low temperature phases of VO_2 coexist across its MIT by defining domains or regions in the samples and the strain fields induced by the geometrical constrains may affect the distribution of those phase domains, type and their evolution during transition.

For instance, $[001]_R$-uniaxial strain along single-crystal nanobeams clamped to a substrate results in a self-ordered chain of metal-insulator domains because of the elastic interaction with the substrate [52, 29]. The spatial periodicity of these domains depends on the nanobeam thickness and the Young's modulus of the substrate [52]. If the strain is produced by bending in non-clamped beams, a triangular pattern of co-existing metal-insulator domains along the nanobeams takes place and the domains become highly mobile when changing the bending conditions. However, if the beams are wider than 5 um the domain pattern turn into irregular (possibly due to biaxial or non-uniform strain) like happens in films [29]. In any case, these patterns respond to the lowest-energy state of the system, which finds a way to reduce its elastic energy by forming domain walls [52].

Stability in VO_2 systems is not only achieved by domains formation but also by the presence of intermediate phases [11, 13, 17-18, 22-23, 38, 53-59], twinning [31, 44, 60-66] or even cracking [12, 44, 67-68]. Upon certain conditions like $[110]_R$-uniaxial strain or doping with Cr, Al or W, the monoclinic M2 and the triclinic T phases have been described as mediators across the monoclinic M1 to rutile (R) structural phase transition [69-70], and a triple point in the Stress-Temperature [39] and Temperature-Pressure [22] phase diagrams of VO_2 is reported (sometimes the Triclinic phase is termed M3 in literature [17]).

Despite the fact that biaxial strain in VO_2 induces more complicated domain patterns and intermediate phases, thin films probably are the most popular morphology of this compound because (i) it eases the implementation of VO_2 in electronics and (ii) strain engineering through epitaxial growth allows to tune VO_2's MIT. Techniques such as the sol-gel method, chemical vapour deposition (CVD), atomic layer deposition (ALD), molecular beam epitaxy (MBE), sputtering or pulsed laser deposition (PLD) are used to grow VO_2 films [47]. For the present thesis, the chosen technique has been PLD, which we have used to grow epitaxial thin films on rutile titanium dioxide (TiO_2) single-crystal substrates.

However, the growth and achievement of pure VO_2 could be difficult due to the large family of VO_x available, especially in epitaxial films, where defects at the substrate's surface, interdiffusion or induced by strain may locally change the oxidation state of V-ions.

Rutile TiO_2 (R-TiO_2) has the same structure and only slightly larger lattice parameters than rutile VO_2 (R-VO_2). This ensures epitaxial growth of crystallographically coherent films, where the substrate-imposed strain can modify the phase stability and the pathway for both the structural and the electronic transition of the samples. More concretely, in this work we demonstrated that such VO_2 epitaxial films evolve from the pristine state to degradation by several mechanisms that may be given at the same time: cracking, formation of nanotweeds

involving a non-reported metallic-monoclinic phase and severe distortions of the monoclinic structure that, eventually, are irreversible and could cause the loss of order in the film.

1.1. GROWTH CONDITIONS

The samples studied in this thesis were obtained by means of the physical vapour deposition technique of PLD. The targets and substrates used, as well as the deposition conditions and their optimization are detailed along this section.

1.1.1. The V_2O_5 targets choice

The films were grown using two different V_2O_5 targets (see table 1.1). The first one was sintered in the laboratory by the Solid-State reaction method using V_2O_5 powder (the procedure is specified in section A1.1 of annex A). In order to compare to a commercial dense pellet, a second target was purchased from Kurt J. Lesker and it was used for growing most of the samples. Instead of VO_2 or metallic V pellets, it is interesting to work with V_2O_5 because this is the most stable V-oxide (highest oxidation state, V^{5+}) and from which VO_2 can be stabilized during growth in a low oxygen pressure atmosphere.

Table 1.1. Comparison between the two V_2O_5 targets used to grow VO_2 samples.

V_2O_5 TARGET	PURITY (%)	DIAMETER (cm)	THICK (cm)	WEIGH (g)	DENSITY (g/cm^3)	DENSITY (%)	COLOUR
Homemade	≥ 99.9 ?	3.14	0.49	7.35	1.94	~ 58	Orange
Purchased	99.9	2.54	0.63	9.73	3.05	~ 91	Dark grey

Figure 1.1 shows the X-ray diffraction (XRD) pattern of the two targets and the powder used to sinter the homemade one. Comparing the results with some vanadium oxides patterns reported in the ICSD database, they suggest that the two targets consist mostly of V_2O_5 with a small fraction of V_6O_{13} and V_3O_5. Star symbols with different colours are used to differentiate the characteristic peaks of these compounds present in our patterns (the ICSD patterns used to do so are shown in fig. A2 of annex A). There is an unknown peak appearing at the homemade target that might be characteristic of V_3O_7 (ICSD code #2338).

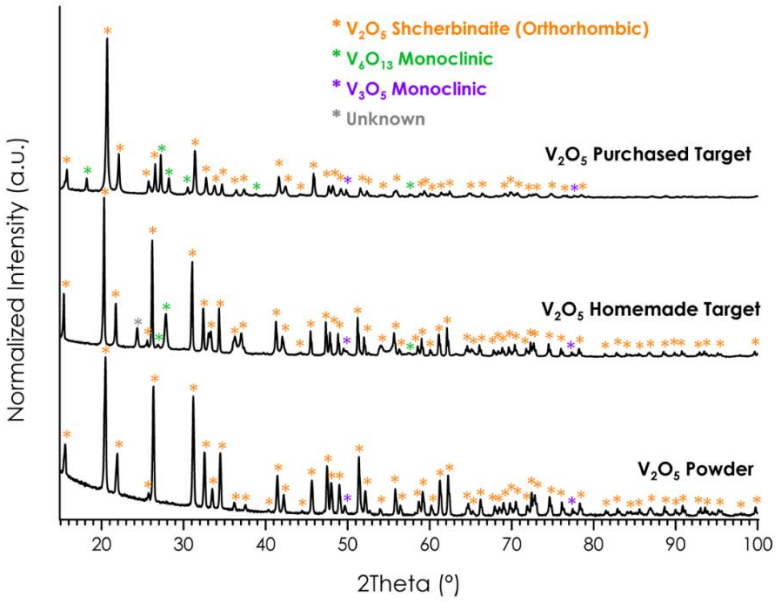

Figure 1.1. Comparison of experimental XRD patterns obtained from the purchased V_2O_5 target, the homemade V_2O_5 target (sintered in the laboratory) and the powder used to make the latter. Star symbols are used to classify most of the peaks, which comparing to ICSD data (see fig. A2), have been identified as V_2O_5, V_6O_{13} and V_3O_5.

The XRD patterns of commercial and homemade targets did not show large differences other than a residual presence of other VO_x secondary phases, the identified V_6O_{13} and V_3O_5. A low-density target is prone to eject large particulates, which would affect the film quality. Surprisingly, the differences in density between the two targets (see table 1.1) do not seem

to affect the quality of the resulting films (see fig. A3). Thus, from now on, either the samples or targets will not be differentiated in this sense.

1.1.2. The TiO_2 substrates

The VO_2 films studied in this thesis were grown on (001)-oriented rutile TiO_2, supplied by CrysTec GmbH (more technical details in section A2). Rutile TiO_2 was chosen as substrate because it is isostructural and has similar lattice parameters to the high-temperature VO_2 phase; hence, it is a suitable candidate to achieve epitaxial strained VO_2 (see introductory chapter). Rutile TiO_2 is a semiconductor with a band gap energy of ~ 3.0 eV [71] and a resistivity > 10^7 Ω·cm [72-73], therefore acting as an insulating substrate. In those experiments where electrical measurements required a bottom electrode, we used Nb-doped TiO_2 substrates. In that case, the doping level specified by CrysTec was 0.5 wt% (that is 0.43 at.%), which is enough to make it conductive [72-75] (see fig. A4).

The quality of a substrate-film interface may depend on the surface of the substrate, and consequently, it can affect the resulting films in terms of crystallographic quality and surface flatness among others [76]. In order to optimize these aspects, five substrate treatments have been tested (see details in section A2.4). They can be grouped in (1) no-treatment, (2) cleaning treatments and (3) thermal treatments. The roughness of a thermally treated substrate is expected to be lower due to reduction of surface's defects –since high-temperature treatments may favour surface diffusion and reconstruction [76]; and this is what we observed when comparing the surface of a non-thermally treated with a thermally treated substrate at 700 ºC during 15h and 100 sccm of oxygen (see figure A5). On the other hand, figure 1.2 compares the structural features of films with different thicknesses grown on substrates previously treated following the three procedure types. All films look similar at room

temperature up to ~ 35-40 nm thick, being rutile (R) independently on the substrate treatment. However, for larger thicknesses above ~ 70 nm, most of the pristine films grown on thermally-treated substrates stabilized the monoclinic (M1) phase (films on Nb-doped TiO_2 had a similar behaviour, see fig. A6) while most of the films deposited on non-thermally treated substrates presented rutile-monoclinic phase coexistence. Moreover, within the non-thermally treated group, the no-treated substrates have mostly grown films with a higher ratio of R/M1 volume fraction (the R-peak is more intense). Thus, non-thermally treated substrates lead to the most interesting films for our purposes –note that the basis of this thesis is to work on a phase coexistence regime, especially in a broad thickness range. No-treated substrates had given the best results regarding this aspect.

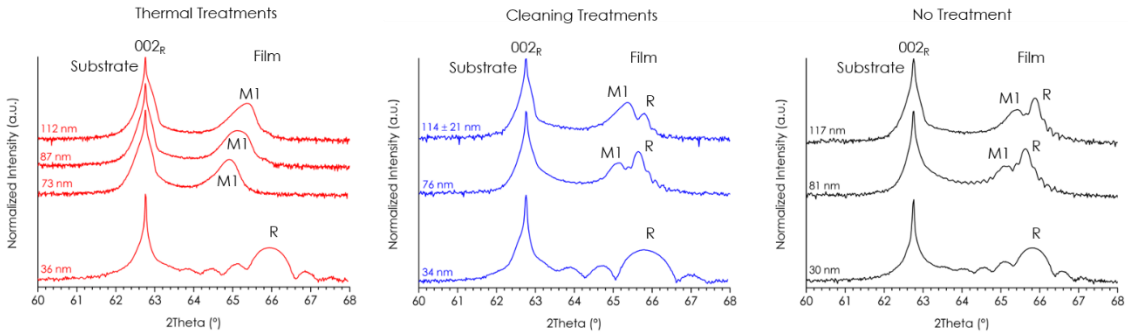

Figure 1.2. Comparison of substrate treatment effect on the resulting VO_2 films. Some representative 2theta-theta scans of VO_2 films with different thicknesses depending on the substrate treatment used: thermal (red curves), cleaning (blue curves) and no treatment (black curves). Thicknesses with error refer to calculated values from the growth rate mean value when samples had not been measured by X-ray reflectivity (XRR) (the complexity of thickness determination in these films is explained in section 1.2 and section A3 of the annex).

It is known that annealing under certain conditions reduces V/Ti interdiffusion between film and substrate, and lowers defects such as vacancies and Ti interstitials in substrate (which behave as dopants), increasing the resistivity of TiO_2 [76]. All this, suggests that the presence of defects on the surface of TiO_2 might favours rutile (metallic) VO_2 films, maybe triggered by

electronic contributions more than structural reasons –at least at our growth conditions (see below next section).

1.1.3. Film deposition conditions

The VO_2 films of this thesis were grown at a deposition temperature of 400 ºC, 10 mTorr of O_2 pressure, nominal fluence of 0.8 J/cm^2 (0.96 ± 0.21 J/cm^2 experimental value), 2 Hz repetition rate and a working distance of 55 mm between target and substrate, similarly to the conditions used by Martens et al. [76]. Second order parameters such as the heating and cooling rate, base pressure, O_2 mass flow, laser spot size and target rotation were 15 ºC/min, ~ (8 ± 2)·10^{-3} mTorr, ~ 1.5 ± 0.2 sccm, 8 ± 1.8 mm^2 and 15 rpm, respectively.

Optimization of deposition conditions

In order to check if those nominal conditions were optimal, some other films were grown under different temperatures (350, 450 and 500 ºC) and different oxygen pressures (1, 5, 20 and 50 mTorr), which are expected to be the most influential parameters in the VO_2 stoichiometry. These two sets were grown by shooting 1500 pulses. The temperature study was performed at a single O_2 pressure of 10 mTorr, and the pressure study was performed at a single temperature of 400 ºC. Figure 1.3 shows the XRD 2Theta-Theta scans of these films.

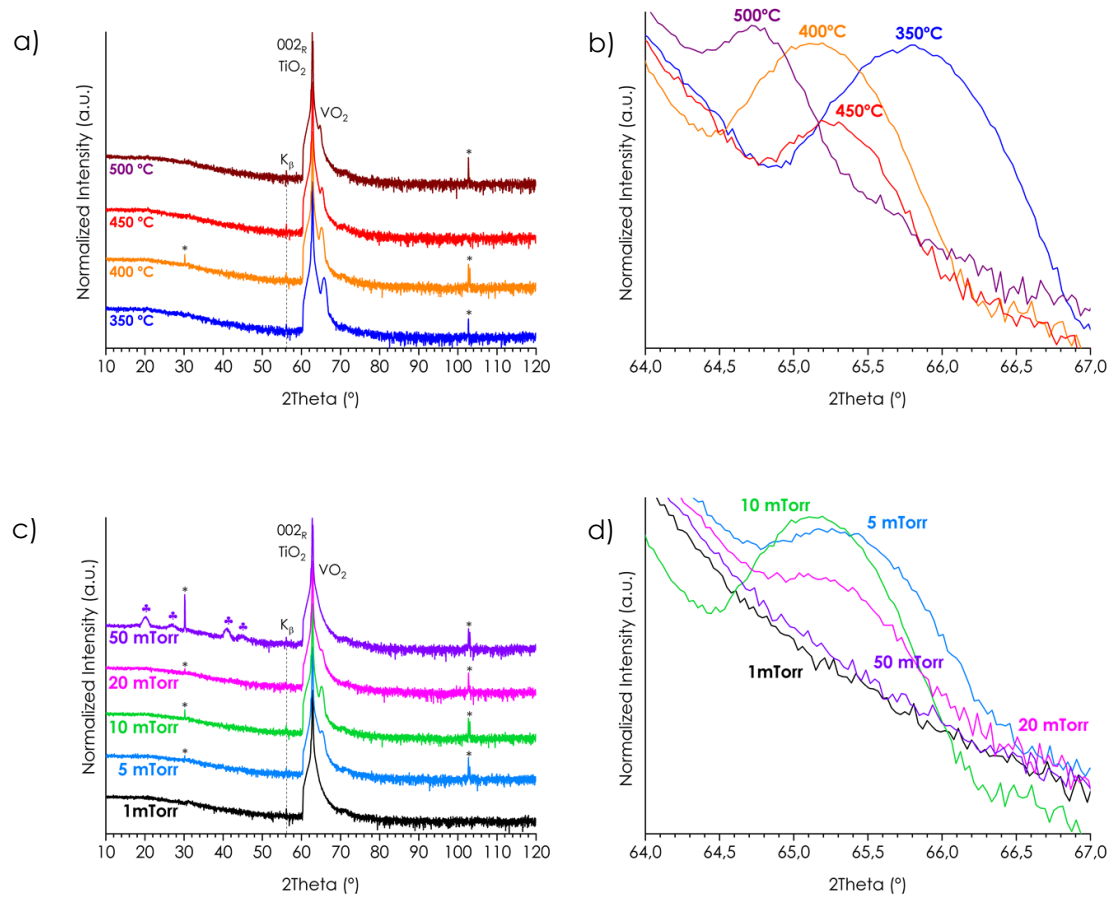

Figure 1.3. Optimization of deposition temperatures and O_2 pressures. XRD 2Theta-Theta scans comparing VO_2 films grown in 10 mTorr of O_2 at **(a)** 350 °C (blue), 400 °C (orange), 450 °C (red) and 500 °C (brown) and **(b)** their detail around the VO_2 peak. XRD 2Theta-Theta scans comparing VO_2 films grown at 400 °C in an O_2 atmosphere of **(c)** 1 mTorr (black), 5 mTorr (light blue), 10 mTorr (green), 20 mTorr (pink) and 50 mTorr (violet) and **(d)** their detail around the VO_2 peak. A dashed line marks the Cu-K_β peak, asterisks mark forbidden extinction peaks related to the substrate and clovers mark peaks of other VO_2 phases or V-oxides.

i. Temperature of the substrate

The temperature optimization-set was performed between 350 ºC and 500 ºC. Within that range, the XRD patterns show only 00L peaks corresponding to a pure c_R-axis orientation of the films (figure 1.3a). The 002_R reflection of VO_2 is detailed in figure 1.3b. Here, one can see that above 400 ºC the peak intensity decreases, what is as a sign of either loss of crystallinity, polycrystallinity, formation of other polymorphs or V-oxides. On the other hand,

below 400 ºC the peak intensity remains similar and maximal. However, the peak position shifts to higher angles as T decreases which corresponds to smaller out-of-plane c_R-axis parameter. Oxygen vacancies typically increase cell volume, shifting XRD peaks to lower angles, and they are more probable when temperature increases. Although the temperature and oxygen pressure used in our optimizations seems to be far from the conditions required for having oxygen deficit in VO_2 films [7, 77], changes in oxygen content cannot be discarded. In addition, taking into account that thermally induced reduction of V_2O_5 into VO_2 under vacuum occurs at ~400 ºC [78] and other VO_2 phases may grow below 430 ºC [21], the chosen substrate temperature to deposit was 400 ºC instead of 350 ºC.

ii. Oxygen pressure (during deposition)

Similarly, the pressure optimization-set was grown between 1 mTorr and 50 mTorr of O_2. At 50 mTorr, symbols in figure 1.3c point several peaks related to the film, which are compatible with having a mixture of VO_2 phases or polycrystalline triclinic VO_2. Figure 1.3d details the 002_R film's peak evolution, revealing how narrow the oxygen conditions are: c_R-axis oriented VO_2 only grows between 5 and 20 mTorr, and the maximum peak intensity is achieved at 10 mTorr.

Note that in both figure 1.3a,c are present several narrow peaks marked with starts. They are the 001_R and 003_R reflections of the rutile TiO_2 substrate (forbidden peaks or extinctions that appear under certain conditions by the multiple diffraction effect, also known as Umweganregung effect, reported in other substrates like silicon) [79-80].

In order to verify the monocrystalline character of films grown under the chosen conditions, grazing incidence scans have been performed (fig. 1.4). With this measurement the epitaxially oriented part of film is generally out from Bragg diffraction conditions, and therefore, only peaks coming from any randomly oriented part of the sample are analysed.

No peaks are present in this type of scans, which confirms that under the mentioned optimal growth conditions, the films have no other orientations but the (001). Thus, making unlikely the coexistence of VO_2 with other Magnéli phases or other VO_2 structures.

For all these reasons, the growth conditions given by Martens et al. (400 ºC, 10 mTorr, 0.8 J/cm^2, 2 Hz) were also the ones mostly used in this work.

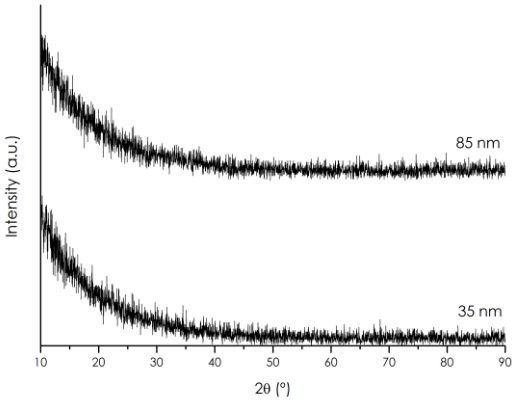

Figure 1.4. Grazing incidence scans (omega = 0.5 º) of an 85 nm and 35 nm thick VO_2 films on rutile TiO_2(001). Samples obtained under the optimal growth conditions used along the thesis.

iii. Oxygen Pressure (post-deposition)

It is known that VO_2 films are very sensitive to oxygen. When VO_2 films are exposed to air conditions, the surface tends to the most stable form, the V_2O_5 compound [81]. Hence, beyond the deposition parameters, the cooling procedure after depositing could be critical in the results, and for that reason, two different methods were tested in this thesis (figure 1.5a). The first one was a 1-Step process, where the samples cooled down at a constant O_2 pressure of 10 mTorr –the same as during the growth. Although the resulting films were crystalline, there were some incongruences related to thickness determination (see next section 1.2 and section A3 of annex). A possible origin was thought to be the film's surface oxidation from VO_2 to V_2O_5. So in that case, the oxygen content during cooling should be even lower than 10

mTorr to avoid oxidation at low temperatures, but at the same time, enough to preserve stoichiometric VO_2. In this sense, taking into account that VO_2 still grows at 350 ºC in 10 mTorr of O_2 gas (seen in fig. 1.3d) and considering the reported V_2O_5 growth conditions (it grows at 220 ºC in ~100 mTorr of O_2 gas [82] but starts to reduce above 400 ºC under vacuum [78]), a second cooling procedure was designed. It is a 2-Step process where the samples cool down at 10 mTorr from 400 ºC down to 300 ºC, and below that temperature, the oxygen flow is interrupted to make the O_2 pressure suddenly decrease down to the minimum achievable ($<10^{-4}$ mTorr). Figure 1.5b contains the XRD scans comparing representative thick films of ~ 80 nm, cooled by these two processes. Note that this comparison was only carried out in samples with non-thermally treated TiO_2, which lead to the most interesting films (discussed in fig. 1.2). The results do not show much differences between the two cooling procedures but Laue oscillations at thicker samples. Films on no-treated TiO_2 (upper curves) had similar Laue oscillations for both methods; while on cleaned TiO_2 (bottom curves), the 2-step cooling (blue) led to a larger number and sharper Laue oscillations in films grown. Since Laue oscillations indicate high crystal coherence in films, the 2-step cooling could help to improve even more the crystallinity of the samples.

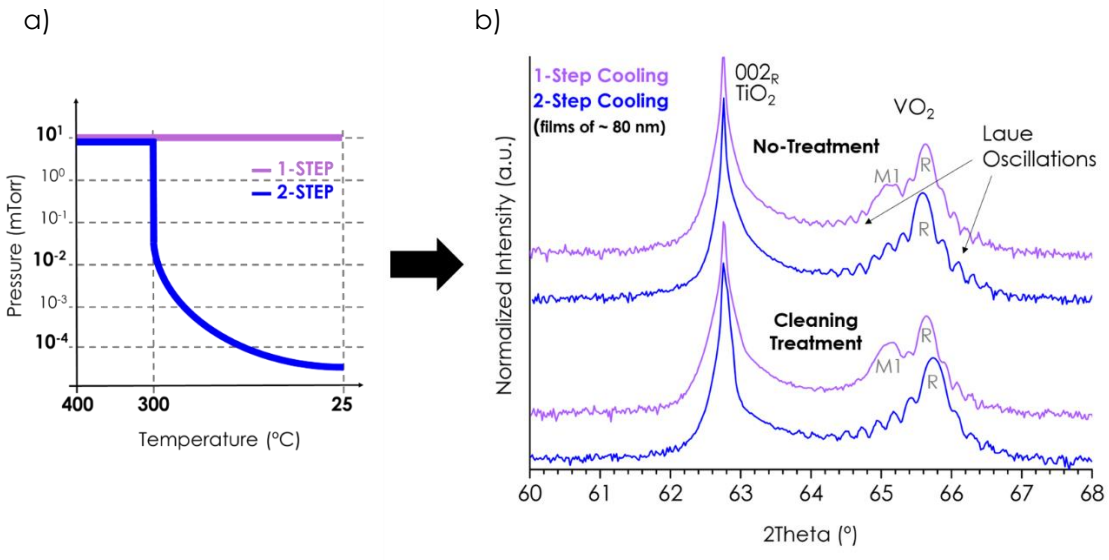

Figure 1.5. Comparison of 1-step and 2-step cooling procedures. **(a)** Scheme of oxygen pressure versus cooling temperature depicting the 1-step (lilac) and 2-step (blue) procedures. In the latter case, just after depositing the film, the temperature decreases from 400 ºC down to 300 ºC while the O_2 atmosphere is kept constant at 10 mTorr. From 300 ºC down to room temperature, the O_2 flow is stopped while gas is evacuated at the possible maximum rate. In our case, at 300 ºC pressure decreases 3 orders of magnitude (from 10 mTorr down to ~$5 \cdot 10^{-2}$ mTorr). When the sample is ready to take out, at room temperature, the pressure reaches ~$5 \cdot 10^{-4}$ mTorr. **(b)** XRD 2Theta-Theta scans show representative films around 80 nm, grown on HPLC-cleaned and no-treated TiO_2 substrates, comparing the two cooling procedures.

1.2. FILM THICKNESS DETERMINATION

The thickness determination of epitaxial films with a single layer structure is commonly obtained from Laue oscillations (in XRD scans) or from Kiessig fringes (in XRR scans). However, the thickness and growth rate determination was not straightforward in the studied films. To understand the relation between thickness and laser pulses required a large number of samples, among others, because of the increasing uncertainty of thickness with pulses. In particular, our statistics have been carried out using the low-angle XRR data of 45 samples. The peculiarities toward this topic will be explained in this section.

In many cases, the results of low-angle XRR were compared to the thicknesses obtained by the Laue oscillations present around the diffraction peaks in 2Theta-Theta scans. Remarkably, the thickness resulting from the latter was often smaller –only some samples cooled following the 2-Step cooling process showed the same result as XRR. While low-angle reflectivity depends mostly on electron density (and thus on composition), Laue fringes around diffraction peaks only reflect the thickness of the crystalline c-oriented layer –and its strain state by applying strain relaxation models [83]. When the intensity of these satellites is asymmetric with respect to the main peak, it is evidence of a gradual change of the interplanar distance along the c-axis. Moreover, if the asymmetry leads to suppression of high-angle

satellites, indicates a large strain-gradient close to substrate while the rest remains coherent and uniform [83]. The discrepancy between the thicknesses obtained from both methods therefore suggests either the loss of such high coherence without need of losing crystallinity, polycristallinity, the presence of an amorphous layer, or the combination of these three; which the 2-Step cooling might be helping to prevent.

Our discrepancies are large (normally more than 10 nm in thicker films) but it cannot be attributed to a layer with other orientation within the film since figure 1.3 showed that our samples have a pure c-axis orientation. On the other hand, the intensities of the Laue oscillations are not symmetric with respect to the main peak and many samples showed its fast decay of the oscillation amplitude –which could be consistent with crystal coherence loss along the c-axis.

Also, as already commented, it is known about the film's surface oxidation forming a V_2O_5 layer of several nm in depth [81]. This would be consistent with having an amorphous layer on surface. Nevertheless, in many cases its thickness would not be enough to cause the whole discrepancy.

Transmission electron microscopy (TEM) studies in cross-section performed during this thesis with other purposes (see chapter 2) did not show significant evidences of interdiffussion, defects, changes in the quality of the crystal or similar justifying this point. At the end of this work, the explanation is not clear yet although the strain relaxation mechanisms and microstructure described in chapter 2 might play some role.

At the end of a comprehensive analysis, the film's deposition conditions used in this thesis have a growth rate of ~ (0.030 ± 0.006) nm/pulse (see section A4).

1.3. CRACKS AND ELASTIC ENERGY IN THE FILMS

Cracks are considered an elastic energy-release mechanism. When stress is applied to a material, it deforms storing the transferred energy into elastic energy. However, all materials can eventually reach mechanical failure when the transferred energy overcomes the maximum energy that the material can store –beyond the elastic and plastic regime. In this mechanical sense, thin films are described by eq. 1, where their strain ε (deformation) is due to mismatch stress induced by the substrate, and the stored elastic energy through that deformation increases with the strain depending on the film thickness τ.

$$E_{elastic} = \frac{1}{2} k \varepsilon^2 \quad \text{(eq. 1)}$$

Where $E_{elastic}$ is the stored elastic energy of a film with a certain strain ε and elastic constant k, which actually depends on film thickness, k(τ).

Many materials relax their strain as thickness increases by, for instance, dislocation generation within the films. This leads to accumulate less elastic energy at thicker films and in principle, they are less prone to mechanical failure. Even so, there are materials that despite the dislocations, still crack [84], and by the given relaxation mechanism, the crack's density decreases as thickness increase. As shown at the introductory chapter (and remarked in chapter 2), our films grow fully or partially strained irrespective of thickness, and this, as it is discussed later, leads to the opposite scenario (with respect to the density of cracks and the thickness relation).

Figure 1.6 and figure 1.7 show that in our VO_2 samples, tensile epitaxial stress induces the films to crack when films are thicker than a critical thickness of ~15 nm. The accumulated elastic energy is released partially relaxing the local strain by cracking along $<110>_R$ directions, and parallel to the $\{110\}_R$ planes. The regions surrounding the cracks show a slightly different contrast from the rest of the material (fig. 1.6c-f). These cracks propagate

all through the film's thickness and penetrate into the substrate (see fig. 1.6c,e-f), generating dislocations there. The possibility of cracks being induced by those dislocations or other defects present in the substrate is discarded though, because cracks appear above a certain critical thickness and their density depends on the film's thickness (fig. 1.7) irrespective of the substrate's batch.

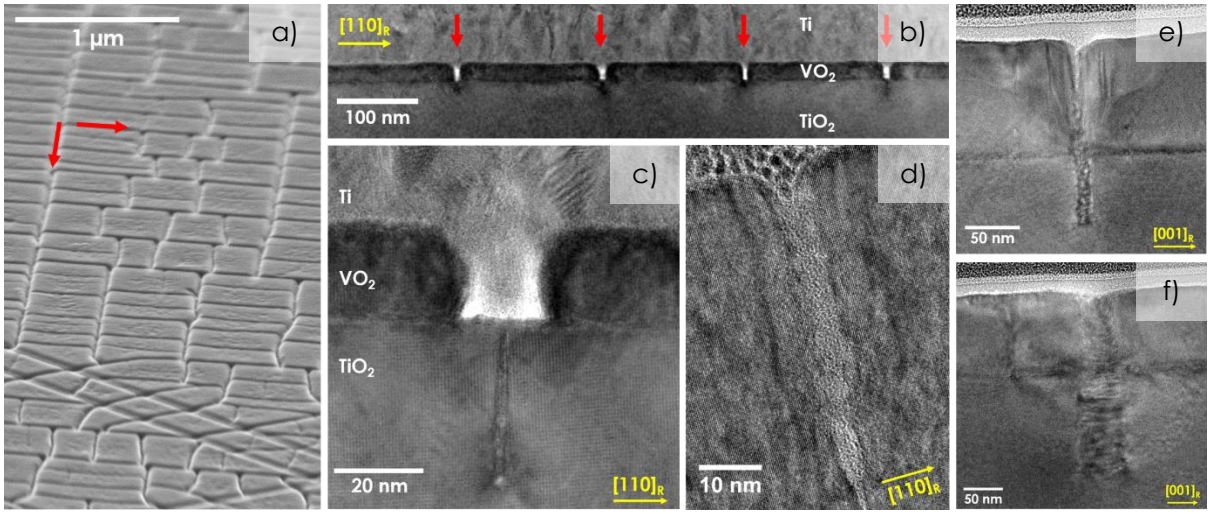

Figure 1.6. Images of cracks. **(a)** SEM image in tilted view with a scale bar of 1 µm. Red arrows mark crack's directions, the $<110>_R$. Some line defects are also present. **(b)** Low magnification STEM cross-section image of a film 20 nm thick in $<110>_R$ zone axis, thus cutting perpendicularly several cracks (marked with red arrows). The scale bar is 100 nm. **(c)** Higher magnification of one of the cracks shown in (b). The fissure even penetrates ~ 30 nm into the substrate. The scale bar is 20 nm. **(d)** HRTEM cross-section image of a film 55 nm thick, along the $<110>_R$ zone axis and a scale bar of 10 nm. **(e-f)** STEM cross-section images of different cracks in an 80 nm thick film along the $<100>_R$ zone axis, therefore cutting the cracks obliquely. Here the fissures penetrate up to 100 nm. The scale bars are 50 nm.

Since there are not misfit dislocations within our films, the concentration of cracks is proportional to thickness and, as just described, the underlying cause is that the thicker the film the larger the mechanical energy to release, hence, larger amount of cracks by unit area [68, 85]. Figure 1.7 clearly depicts this behaviour.

Misfit dislocations are generally produced during film growth, at high temperature. If they (or other strain-release mechanism) are not generated –like seems to happen in our samples, the films would remain fully strained. It is during the cooling down from deposition temperature to room temperature, when VO_2 changes from rutile to monoclinic, and the difference in cell parameters at T_c generates a sudden increase in the elastic energy, which is partially released by the formation of cracks that locally relax the strain. Therefore, the first cracking takes place inside the PLD chamber, while the film cools down after the growth across the first phase transition of the film.

Depending on the sample's history the cracks may be broaden. For instance, thermal cycles make the cracks to open (fig. 1.6a-c shows crack gaps of ~20 nm width) while pristine samples keep narrower closed cracks around 5 nm width (fig. 1.6d). Thermal cycles in cracked VO_2 (which means repeated expansion and compression of the film) has an analogous effect than water in mud-cracking during drying cycles [86-87].

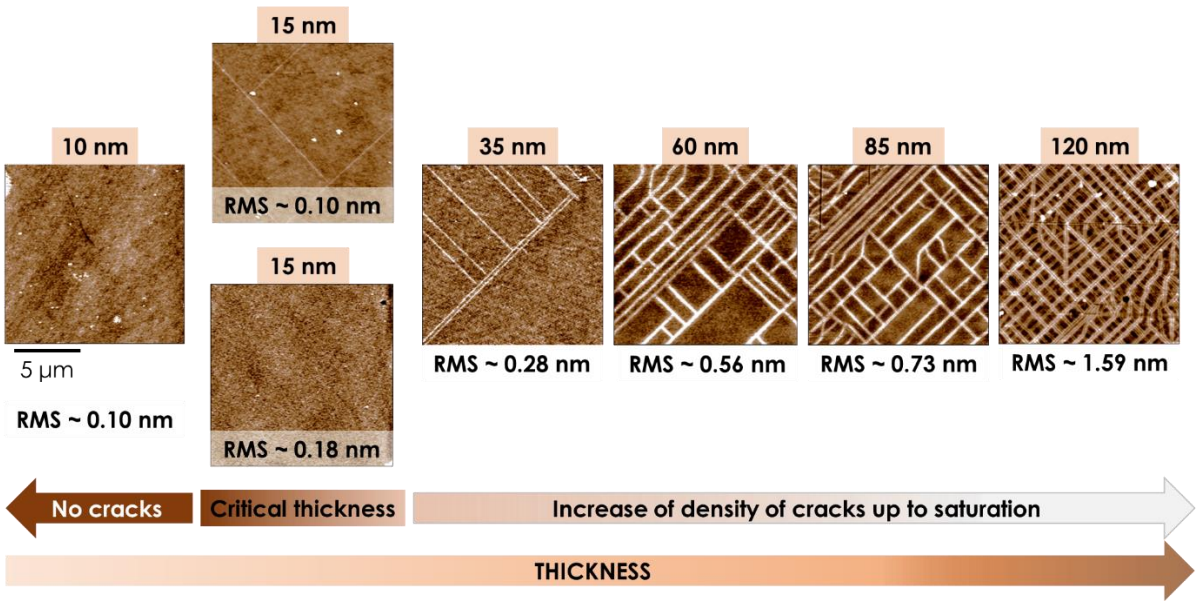

Figure 1.7. Cracks versus film's thickness. Below the critical thickness of 15 nm, cracks are not present in the films. When films are 15 nm thick, small strain variations may trigger the cracking. Above 15 nm, the cracks' density increases with thickness, what also makes the roughness to increase in the same way.

When samples are pristine or submitted to a tensile strain, they can keep on cracking, so the cracking pattern may only be in a "transient state". Room temperature optical images in figure 1.8a-b show how a region of a 20 nm thick film re-cracked after a few thermal cycles. Many domains are still strained (dark-metallic domains), therefore able to carry on cracking. Even in the absence of thermal cycling, tiny variations in environmental conditions may trigger this cracking phenomenon spontaneously in extremely stressed films. For instance, optical images of a sample ~120 nm thick, show it had big strained (dark-metallic) domains just after being grown (fig. 1.8c). After 3 months, with no thermal cycling history yet, having been stored in vacuum with temperatures between ~20ºC and 25ºC, the sample presented a much higher density of cracks and turned into more relaxed and insulating (no dark regions anymore) (fig. 1.8d).

Although the presence of a thermal expansion mismatch between film and substrate could be considered critical in crack's formation, figure 1.8e-f shows evidences that it might be not contributing since new cracks were created in a film by only applying voltage –without involving temperature. The AFM image of figure 1.8e revels the topography of a film at 15 ºC before applying on its surface a tip voltage of ±2V, at several points (marked with different colours). After touching the surface with the biased tip during 10 seconds, it had been originated two cracks for the two bias (marked with red arrows) and in a few cases, it left a hole (yellow arrows) (fig. 1.8f). Since the substrate was in this case a non-doped TiO_2 (insulating), there was not any current density flowing through the VO_2 that could increase locally the temperature of the film by Joule effect –thus, no thermal mismatch triggering the cracking. As the basis of chapter 3, the insulator-to-metal transition of VO_2 can be induced by charge injection applying a voltage. These facts could suggest that crack formation and metal-insulator phase boundaries might be related –either through an extra tensile-strain at the interface due to changes in the unit cell or through electronic reasons only.

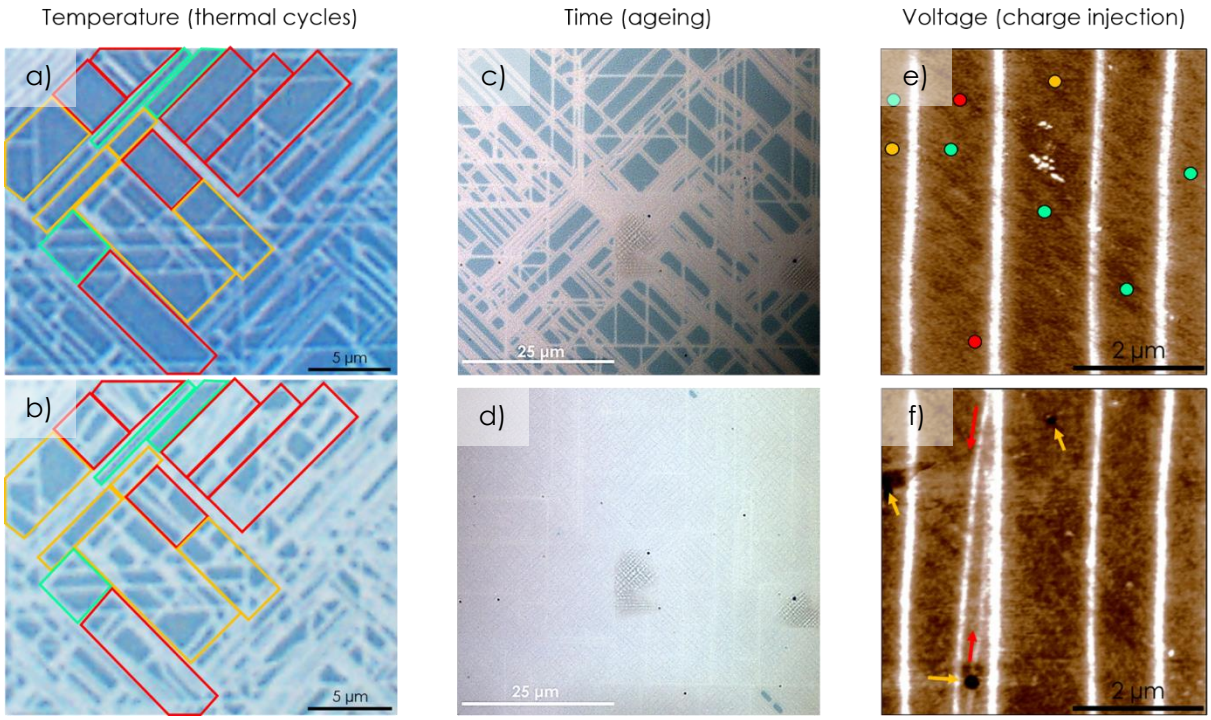

Figure 1.8. Cracking mechanisms. Optical images of a 20 nm thick film **(a)** before and **(b)** after several thermal cycles to induce the MIT. Green rectangles mark regions that have not changed, yellow rectangles mark regions that have cracked but are still recognizable and red rectangles enclose regions that have increased considerably the density of cracks. The scale bars are 5 µm. Optical images showing spontaneous re-cracking of a film 120 nm thick in its **(c)** pristine state and **(d)** 3 months later. The scale bars are 25 µm. AFM images showing the topography of a film 80 nm thick **(e)** before and **(f)** after applying a voltage of ±2V with the tip of the AFM. Green circles mark the points where the voltage had not induced changes on the surface, yellow circles mark the points where a hole (yellow arrows) has been generated after applying a voltage and red circles mark the points where a crack (red arrows) has appeared after applying the voltage (for both positive and negative bias).

Since cracks are discontinuities in the volume of a film, they will alter the electrical transport properties by hindering the in-plane pass of the current. Depending on how open and wide the cracks be, it may happen to have a film in its metallic state presenting a resistance higher than the resistance of another film at the insulating state. Besides, the regions adjacent to cracks are more relaxed than the rest because of the local strain-energy release. This fact leads to monoclinic regions, which are in principle, insulating.

Cracks have an important structural and electronic role in our samples, and for this reason, this thesis will base on how they affect the properties of VO_2 thin films.

1.4. FILMS DEGRADATION

During this work, either with the pass of the time or the performance of some experiments, it has been observed the degradation of the samples. Besides crack formation, another consequence of such high elastic-energy is the peeling of the films above a certain thickness. Also and probably due to strain, films lose coherence with time or after thermal cycles. On the other hand, the film thickness might reduce by some kind of chemical etching when cleaning the samples. Therefore, the VO_2 films were in constant evolution, which made difficult to study this material, to replicate samples and experimental conditions, or to compare results in order to draw conclusions.

1.4.1. Peeling

A couple of films with thicknesses between 120 and 150 nm had peeled just after growth. The optical microscopy image in figure 1.9 shows the surface of the thickest sample (~145 nm) taken immediately after removing it from the PLD chamber. Tensile strain may be so high that above a certain critical thickness (> 120 nm), the accumulated energy not only cracks the film but also makes the still-strained domains peel off from the substrate.

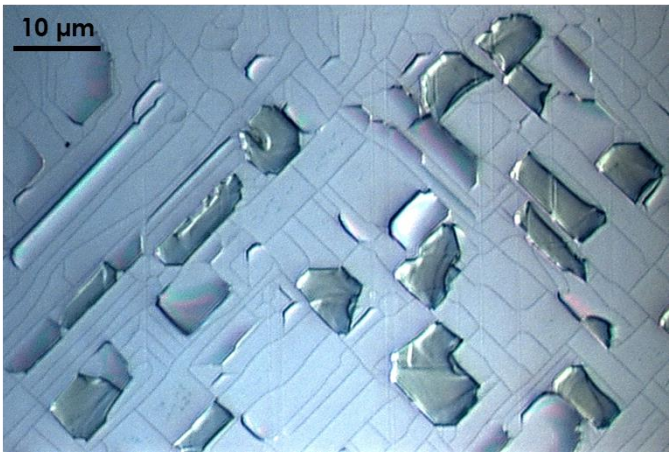

Figure 1.9. Peeling in films above 120 nm. The high elastic-energy stored and released in the film can make the material to unstick, partially or totally, from the sample.

1.4.2. Structural disorder

After thermal cycles, certain beam exposures or simply the pass of time, it is possible to observe the aging of the VO_2 films, from a high-coherent crystal in its pristine state until being totally disordered, losing its properties. Two representative samples of ~120 nm and ~10 nm are shown in figure 1.10 evidencing this effect, which is therefore independent of thickness (like strain in these films). The RSMs series at room temperature (fig. 1.10a-c) around the rutile $\bar{1}\bar{1}2_R$ reflection reveals the structural evolution of the thickest sample across its aging (an optical view of this sample is also in fig. 1.8c-d). The film, which has grown rutile (R) due to the in-plane tensile strain (fig. 1.10a), start changing toward monoclinic through a tetragonal-like structure (M1 in fig. 1.10b) with the pass of time –and also due to crack formation in this case (fig. 1.8c-d). It happened after 3 months being stored in a desiccator in low vacuum, with the rest of samples, at room temperature (in other cases this evolution took months longer, without noticing an increase in crack's density). Two white dashed lines mark the initial R and final M1 peaks position to follow their evolution. The performance of thermal cycles across the MIT accelerates this structural evolution (fig. 1.10c), that eventually results in the extinction of the diffraction peaks (not shown). Hence, a disordered structure. It worth noting that during degradation the VO_2 structure remains in-plane strained, either R or M1 (tetragonal-like), because the VO_2 peaks are vertically aligned with the substrate while their intensity decreases.

Figure 1.10d, on the other hand, contains two 2Theta-Theta scans of a thinnest film (10 nm), single R and below 15 nm (no crack formation), around the 002_R reflection before (blue curve) and after starting its degradation (orange curve) due to the pass of time (none experiment or thermal cycles were performed in this sample).

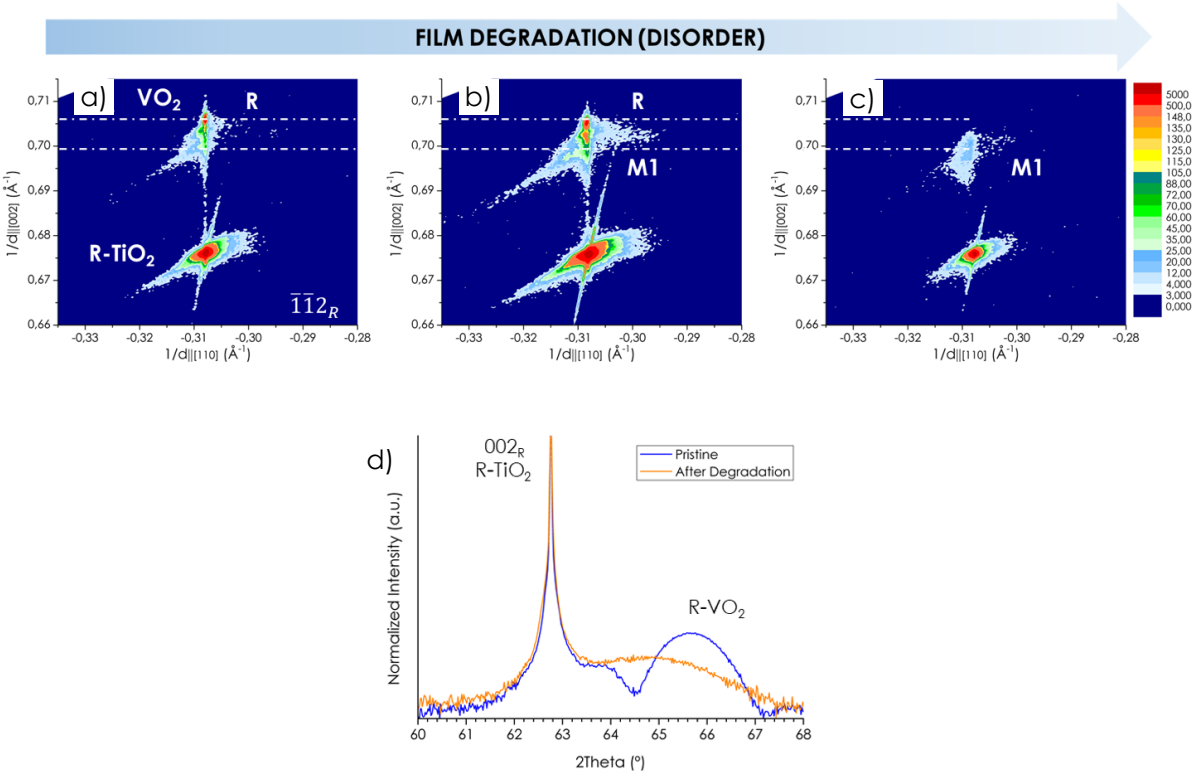

Figure 1.10. Degradation of VO_2 films by structural disorder. RSMs at room temperature around the $\bar{1}\bar{1}2_R$ reflection of a 120 nm thick film showing **(a)** its pristine state, **(b)** after 3 months and **(c)** after many thermal cycles. White dashed lines mark the initial rutile (R) and final monoclinic (tetragonal-like) M1 peak positions to follow the structural evolution across the film's aging. **(d)** 2Theta-Theta scans of a 10 nm thick film being pristine (blue) and after 6 months, once started its degradation (orange).

A hypothesis to explain this behaviour is that, the tensile stress applied by the substrate induces a sustained strain in the film that might surpass the elastic limit of VO_2, inducing permanent deformations in the interatomic bonds within the structure that irreversibly, makes the film disordered. Eventually, the samples losing their crystallinity and electronic properties. Thermal cycles across MIT would enhance the disorder effect because temperature increases lattice vibrations, but also because the stress induced at the phase boundaries during phase coexistence contributes to increase the stored elastic energy in the film.

On the other hand, since cracks formation implies to reach the mechanical failure point of the material, it would be reasonable to expect the previous plastic deformation toward the

cracks' regions (contributing to disorder), following the strain-relaxation gradient perpendicular to a crack direction.

1.4.3. Etching

As mentioned in previous sections 1.1.3 and 1.2, it is expected to have a certain V_2O_5 thin layer on the films' surface due to VO_2 oxidation. V_2O_5 is soluble in concentrated acids and alkalies, slightly soluble in water, insoluble in alcohols [88], and it is reported to dissolve away in dilute aqueous solutions of sodium carbonate (Na_2CO_3) or ammonia (NH_3) [42]. Nothing was found reported about the V_2O_5 solubility in acetone, though. In many cases, before performing certain characterizations that required a very clean surface, the VO_2 samples were cleaned following the same HPLC procedure used with substrates (detailed in section A2). With the pass of the time it was observed an "apparent" decrease in thickness of some films, reason why it is plausible to think that chemical reactions with acetone during the cleanings, somehow wash off or dilute the superficial V_2O_5 layer. An example is explained below, shown in figure 1.11.

A $VO_2/TiO_2(001)$ thin film of ~10 nm was grown to carry out some experiments outside our laboratories[a,b]. After several months performing thermal cycles to characterize the film across the MIT the sample changed losing its optical, electrical and structural features. When the sample was back to our laboratory, its pristine and aged states were compared. Figure 1.11a shows the 2Theta-Theta XRD scans of the film as-grown (blue curve) and degraded (orange curve), which has lost the 002_R diffraction peak. Thus, either VO_2 has changed to other oxide or has lost its c-axis order or both. At this degraded state, X-ray Photoelectron Spectroscopy (XPS) had revealed the film to be mostly V^{5+} (at least within the depth

[a] Institute of Applied Physics, Technische Universität Dresden, Germany; and
[b] ct.qmat: Dresden-Würzburg Cluster of Excellence - EXC 2147, Technische Universität Dresden, Germany,
in collaboration with Prof. Lukas M. Eng[a,b].

penetration of the X-rays), hence V_2O_5 (fig. 1.11b, courtesy of Maximillian Obst[a]). After cleaning the sample by the HPLC-procedure, XRR (fig. 1.11c) and a new XPS measurement were performed in our laboratory (fig. 1.11d). The comparison of the XRR scans before (blue) and after degradation (orange) showed a thinner film of ~6.5 nm after the cleaning (pristine was ~10 nm). Moreover, the new XPS measurement revealed a V^{4+} oxidation state (VO_2).

This sequence of facts therefore suggests that the HPLC-cleaning procedure might be somehow washing off or dissolving the surface of the film, which is supposed to be V_2O_5. The discrepancy in thickness (~3.5 nm) is consistent with the reported depths of this layer [81]. In the case of having this V_2O_5 etching effect, the film could be vanishing until being completely off. The cyclic process of removing the oxidized layer and exposing the surface to oxidizing air-temperature conditions repeatedly, might lead to the film's disappearance. This hypothesis would explain the case of one of our samples, which pristine was ~40 nm thick by XRR but after many experiments in air, thermal cycles and HPLC cleanings, a TEM cross-section showed, surprisingly, a thickness of ~20 nm (sample in fig. 1.6b-c). With no doubt, this chemical etching effect would be somehow a way of sample's degradation.

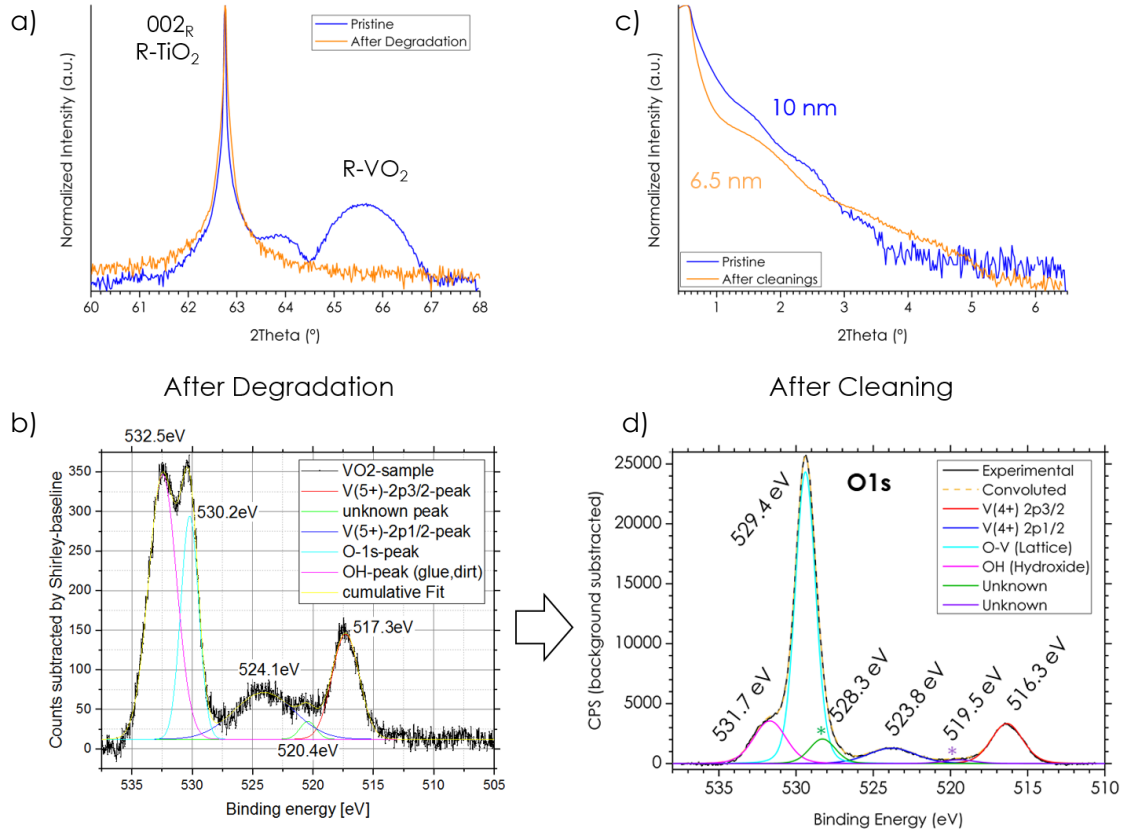

Figure 1.11. HPLC-cleaning effect after sample's degradation. **(a)** 2Theta-Theta XRD scans around 002_R reflection of a 10 nm thick film before (blue curve) and after its degradation (orange curve). When the film is pristine the diffraction rutile (R) peak is present with a few Laue oscillations, but it disappears once the film has lost its properties (degradation). **(b)** Experimental XPS (black curve) around the O1s region and its deconvolution (coloured curves). The fitting positioned the V $2p_{1/2}$ and $2p_{3/2}$ levels at ~524.1 eV and ~517.3 eV respectively. Thus, most of the vanadium within the depth penetration (less than 10 nm) is V^{5+} (V_2O_5). A comparison of XRR before degradation (blue curve) and after cleaning (orange curve) is presented in **(c)**. The thickness related to the pristine state was ~10 nm, while after the degradation and cleaning the thickness resulted in ~6.5 nm. The XPS performed after cleaning (corresponding to the orange XRR curve) is depicted in **(d)**. The experimental spectrum around the O1s region (black curve) is also fitted (coloured curves). In this case, the V $2p_{1/2}$ and $2p_{3/2}$ levels were positioned at ~523.8 eV and ~516.3 eV, respectively. Comparing to XPS references from NIST database[c], this result is consistent with V^{4+}; thus, VO_2 after cleaning the sample.

[c] http://www.xpsfitting.com/2008/09/vanadium.html

1.5. SUMMARY

Since the 60's, the VO_2 properties have been investigated in many morphologies from bulk single crystals to nanoobjects. So far, the most popular type is thin films, likely because they allow to tune the MIT by epitaxy engineering as well as the easy implementation in electronics. Among all the methods used to obtain VO_2 thin films, the samples in this work had been grown by PLD.

It is complicated to achieve pure VO_2 samples because there is a large VO_x family available, where VO_2 polymorphs and the V oxidation state are correlated. This is especially critical in thin films as the epitaxial stress may stabilize other VO_2 phases, besides the interface with the substrate may locally change the oxidation state of the V-ions –due to defects or interdiffusion, for instance. Thus, the substrate used and its surface conditions are important.

In this thesis the films were grown on rutile TiO_2 single crystals (which were 0.5 wt% Nb-doped when electrical measurements required a bottom electrode). Rutile TiO_2 has slightly larger lattice parameters than rutile VO_2 –the high-temperature phase across the MIT; and because of being isostructural, epitaxy under tensile or compressive stress is ensured, which reduces or increases the temperature of the metal-insulator transition by modifying the V-V distance along the c_R-axis direction. More concretely, the (001)-oriented R-TiO_2 substrates used in this work induce an in-plane tensile strain that compresses enough the c_R lattice parameter along the out-of-plane direction, to lowering the T_{MIT} down to room temperature.

The aim of this chapter has been to detail the growth process of the samples, from raw material to high crystallographic quality of VO_2 films. It has shown that,

- The samples were grown from two different V_2O_5 targets. The first one was homemade, sintered in the laboratory following a simple process by the Solid State Reaction method using V_2O_5 powder; and the other one was purchased, commercial. Both targets mostly consisted of V_2O_5 with some residual V_6O_{13} and V_3O_5 oxides. Despite the large difference

in density (homemade ~ 58% and commercial ~91%), they resulted in identical films from a crystallographic quality point of view.

- The TiO_2 substrates were treated following 3 types of procedures: (1) no-treatment, (2) cleaning treatments and (3) thermal treatments. All of them led to R-VO_2 films for thicknesses below ~35-40 nm. However, above ~70 nm the thermal treatments stabilized the M1-VO_2 phase while the non-thermal treatments presented R/M1 coexistence. The R/M1 volume ratio seems bigger in samples grown on no-treated substrates.
- Substrate temperature and oxygen pressure (the most influent film deposition conditions) were optimized using 10 mTorr of O_2 pressure from 350 ºC up to 500 ºC, and a substrate temperature of 400 ºC in a O_2 pressure range from 1 mTorr to 50 mTorr. The film was, partially or in its totality, (001)-oriented VO_2 for all temperatures but not for all O_2 pressures –only within a narrow window ranging from 5 to 20 mTorr. A temperature of 400 ºC in 10 mTorr of O_2 resulted in the optimal deposition conditions to obtain pure (001)-oriented VO_2.
- The film deposition conditions used to grow the samples were a substrate temperature of 400 ºC, 10 mTorr O_2 pressure, nominal fluence of 0.8 J/cm^2 (0.96 ± 0.21 J/cm^2 experimental value), 2 Hz repetition rate and a working distance of 55 mm between target and substrate. Other second order parameters were the heating and cooling rate of 15 ºC/min, base pressure of ~ $(8 \pm 2)\cdot 10^{-3}$ mTorr, O_2 mass flow of ~ 1.5 ± 0.2 sccm, a laser spot size of ~ 8 ± 1.8 mm^2 and target rotation of 15 rpm.
- It has shown that a post-deposition cooling process where oxygen pressure decreases with temperature might improve the crystallographic quality of the films.
- The thickness determination of the films is not straightforward and requires an especial care. The thickness uncertainty increases with the number of pulses and the thickness

value of a given film is often different depending on the method used. The most reliable thickness is normally obtained by XRR (indeed, it is the direct observation by TEM cross-section but this is not an average value). The explanation it is not clear but the microstructure and the strain relaxation mechanisms described in next chapters may play some role. The mean value of the growth rate resulted in (0.030 ± 0.006) nm/pulse.

- Contrary to other materials, in our samples there are not misfit dislocations acting as strain relaxation mechanism. Hence, the films are strained irrespective of thickness. When the accumulated elastic energy exceeds the maximum storable by the film, the tensile epitaxial stress induces the films to crack above a critical thickness of ~15 nm, and from that moment, the density of cracks increases with thickness up to a saturation limit. Cracks follow the $<110>_R$ in-plane directions and propagate inside the film from surface to substrate. Therefore, cracks are parallel to $\{110\}_R$ planes.
- Depending on the history of a sample its cracks evolve over time. Thermal cycles make the cracks to open due to the expansion-compression of the film. So that, cracks in pristine samples may be closed and narrower; and strained films, since they are not yet relaxed, may be able to keep on cracking (so the density of cracks would be in a "transient state").
- It has shown that cracks can also be created by just applying a voltage with a tip of an AFM, without any current flow that could induce Joule effect. Therefore, in this case, thermal expansion mismatch between film and substrate may not be contributing to crack formation.
- Since cracks are discontinuities in the film's volume, they are expected to hinder the percolation of the current, affecting the electrical transport.
- It is difficult to compare and study this material because the samples are in constant evolution from their pristine state until their complete degradation, what is likely caused

by structural disorder. In addition, peeling (above ~120nm) and chemical etching after multiple cleanings of the samples can occur.

CHAPTER 2.

Strain effect on film's microstructure

2.0. INTRODUCTION

The canonical metal-insulator transition of VO_2 in bulk form is described by a simultaneous electronic and structural abrupt change in the material around 68 ºC. The dimerization of V-V chains in the monoclinic M1 structure causes the insulating character of VO_2. However, above the critical temperature, the stable structure is rutile (R). This high-symmetry phase has equidistant V-V chains that allow the metallic behaviour [1] (see the introductory chapter).

When a rutile substrate like TiO_2(001) is used to grow VO_2 films, the metallic-rutile VO_2 phase is favoured, and consequently, the critical temperature of the transition decreases [30, 59, 89-93]. Temperature-dependent XRD shows this fact by revealing the structural M1 to R transition. Figure 2.1 collects the case of an 85 nm VO_2 film grown on rutile TiO_2(001). Below 30 ºC and above 60 ºC, the X-rays show single VO_2 peaks corresponding, respectively, to the M1 and R phases. However, between 30 ºC and 60 ºC there is coexistence of both M1 and R, being the peaks equally intense around 35 ºC – 40 ºC (there is hysteresis). This is below the bulk's critical temperature of 68 ºC.

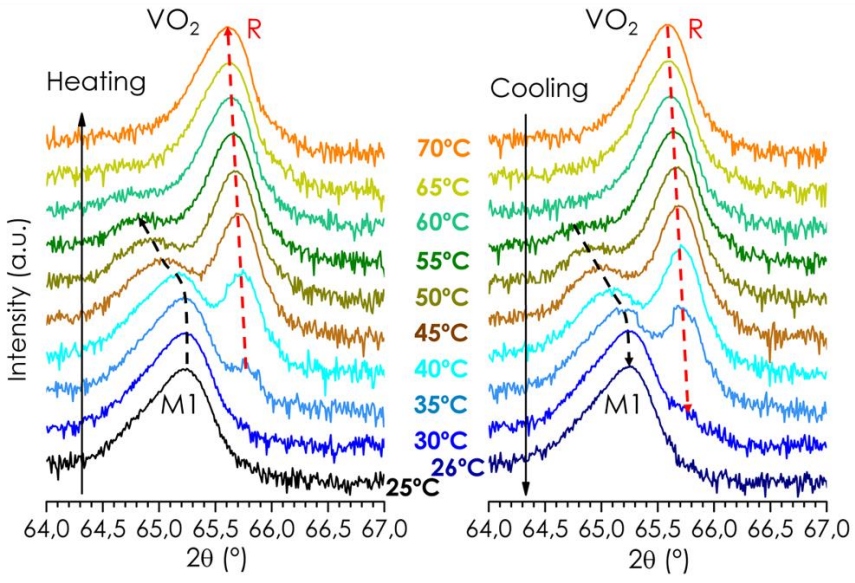

Figure 2.1. Structural phase evolution across the metal-insulator transition of VO_2 grown on R-TiO_2(001), depending on temperature. The coexistence of two diffraction peaks

corresponding to the R and M1 VO_2 phases, takes place well below 68 °C, the critical temperature of bulk material. Dashed arrows point the evolution of the peaks across the 2theta-theta scans.

The shift of the structural phase transition is a consequence of the strain induced by the substrate, which does not relax with film's thickness conventionally. The way in which strain relaxation proceeds is important, resulting in a mesoscopic phase separation that will be structurally described in this chapter and functionally exploited in the next chapter. The other consequence of the introduction of strain is the stabilization of a new, previously undescribed phase in VO_2, which forms a fine tweed structure. All these structural effects are described in the present chapter.

2.1. STRAIN RELAXATION AND MESOSCOPIC PHASE SEPARATION DUE TO CRACK FORMATION

In epitaxial films, there are mechanisms known to release strain, such as point defects –like oxygen vacancies, or dislocations –like misfit dislocations. Normally, the strain it is expected to relax continuously with thickness above a certain critical thickness [94]. However, as shown at the introductory chapter, the studied VO_2 films do not progressively relax mismatch strain with thickness –the lattice parameters keep partially (tensile) strained. This is because instead of other mechanisms, the main one to release the stored elastic energy is the formation of cracks (see chapter 1), and therefore, cracks locally stabilize the low-energy monoclinic VO_2 phase. Meanwhile, the regions far from the crack-edges are not affected by this energy release and remain fully tensile-strained when the film is pristine. All these facts result in a mesoscopic phase separation of strained rutile (metallic) domains framed by

monoclinic (insulating) VO_2, affecting the macroscopic electric transport properties such as current percolation.

Figure 2.2 depicts the evolution with thickness of this phase separation. In terms of structure, figure 2.2a, which is a collection of XRD 2Theta-Theta scans around the substrate's 002 reflection at room temperature and leads to the c-axis lattice parameter determination, shows that VO_2 evolves from rutile (R) thin-films (red curves) to monoclinic (M1) thicker-films through phase coexistence (green curves). Above ~ 80-85 nm and probably depending on the substrate's surface (see chapter 1), VO_2 can keep the R-M1 coexistence or stabilize the bulk-like M1 phase (black curves). However, the XRD peaks position is independent of thickness, and comparing them to bulk (relaxed) VO_2 [95-96] (dashed grey lines labelled R_B for rutile and $M1_B$ for monoclinic), the studied films have a shorter out-of-plane lattice parameter (resulting from a compressive-strain along the c-axis). Hence, this is consistent with having in-plane tensile-strained films, regardless of thickness.

Figure 2.2b shows the dependence of macroscopic electrical transport with the mentioned VO_2 structural phase vs thickness scenario. In order to illustrate the three types of "structural phase state" fig.2.2a depicts a representative resistivity curve for each case, using the same colour code (pure R in red, R-M1 coexistence in green and pure M1 in black). These resistivity curves reflect the fact that as the M1 volume fraction increases from R-M1 coexistence up to pure-M1, the critical temperature of the films also increases but it is below the M-I transition temperature (T_{MI}) of bulk, even for a pure M1 case (black resistivity curve). This result is consistent with having strained VO_2 [refs 2-8] (see introductory chapter), either in the rutile or monoclinic form. Note also that, where structural phase coexistence exists according to the diffraction patterns, the metal-insulator transition shows two jumps at different T rather than one, consistent with a non-homogeneous space-distribution of electronic phases within the film. Moreover, there is a vertical shift of the resistivity curves to larger values (higher resistivities). Since resistivity is, in principle, an intrinsic property of a

material, this vertical shift is suggesting the presence of any element in the films that depends on thickness and reduces the current percolation through the VO_2.

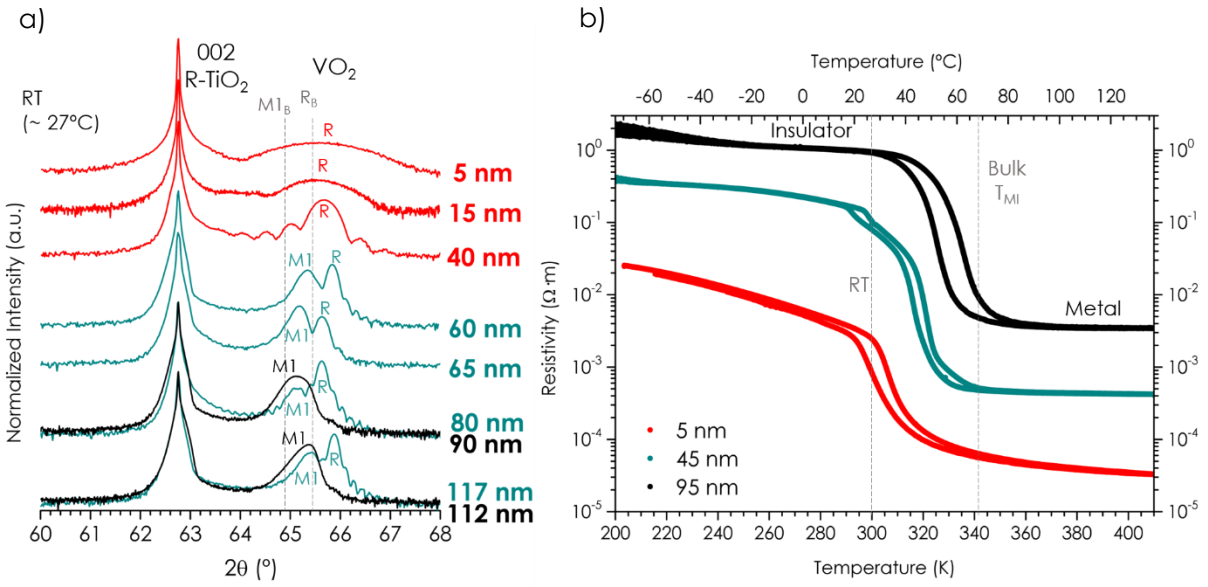

Figure 2.2. Metal-Insulator (MI) transition depending on the structural phase and thickness. **(a)** 2Theta-theta scans around the substrate's 002 reflection of some films with representative different thicknesses, taken at room temperature (RT). Red curves group the thinnest samples, which show pure R phase up to ~35-40 nm. Black curves represent the thickest samples, which under certain conditions, tend to be pure M1 phase from ~80-85 nm. The intermediate range is plotted by green curves. They have two VO_2 peaks associated to the R and M1 phases coexisting in the film. Dashed lines indicate the 2θ peak positions of bulk R (R_B) [95] and bulk M1 ($M1_B$) [96]. The resistivity depending on temperature of samples that are representative from those structural ranges is shown in **(b)**. The temperature of the MI transition (T_{MI}) approximates to the bulk's as the M1 volume fraction increases.

Based on these previous results, we have therefore carried out a microscopic investigation. Inspection by scanning electron microscopy (SEM) and atomic force microscopy (AFM) indicates crack formation as the main mechanism to release the stored elastic energy –fissuring a strained volume reduces its size, so does the elastic energy. Figure 2.3a shows a SEM image of a film of 90 nm thickness, revealing that the film is criss-crossed by an array of cracks, with the zoom-in (fig. 2.3b) showing that the width of the cracks is about 10 nm. Atomic force microscopy of a series of films with different thickness (figure 1.7 of chapter 1) illustrates the relation between thickness and density of cracks: the thicker the film the higher

the crack's density. This is consistent with the known mechanism of strain (elastic)-energy relaxation by cracks: as film thickness increases, so does the accumulated elastic energy, which eventually surpasses the critical value required to create a crack. Further increasing film thickness results in the generation of more cracks, which progressively relax the strain-energy [67-68, 85].

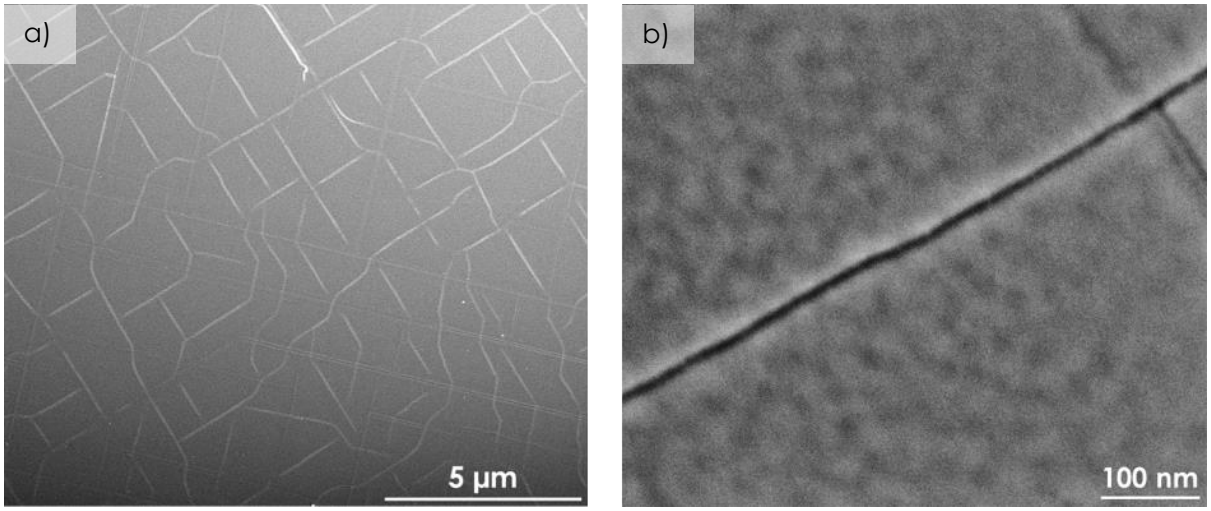

Figure 2.3. Cracking as local strain-energy relaxation mechanism in VO_2 thin films. **(a)** SEM image showing the array of cracks in a 90 nm film and **(b)** zoom-in of one of those cracks.

As anticipated at the beginning of the current section, this scenario leads to still-strained domains delimitated by cracks, surrounded by VO_2 that has released elastic energy –prone to stabilize the lower-energy M1 phase, which should leave some footprint across the metal-insulator transition in these films.

In order to study this distribution of local strain relaxation, we turn to high-resolution transmission electron microscopy (HRTEM) (figure 2.4, already introduced in chapter 1). The HRTEM images of fig. 2.4a-b contain, respectively, the cross-section view of a crack and its magnification seen edge-on (i.e., along the $[110]_R$ direction). A structural contrast can be observed within ~5 nm at each side of the crack, extending through the whole thickness of

the film. The Fast Fourier Transform (FFT) from the strained VO_2 matrix (far away from the crack) is shown in fig. 2.4c. The FFT from the interface of both regions, matrix and crack-edge regions (fig. 2.4d), shows a splitting perpendicularly to it (indicated by arrows) –this is the direction of the strain-energy released by the crack, as expected for a M1-R interface due to the difference in their in-plane lattice spacings. On the other hand, the absence of splitting along the out-of-plane direction indicates that this M1 structure has grown clamped to the R one along this direction.

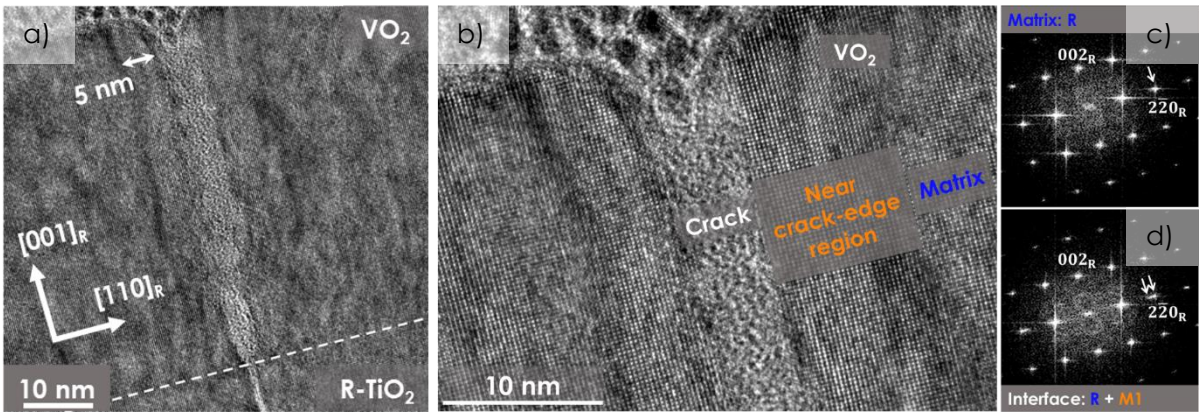

Figure 2.4. VO_2 structural features near and far from a crack-edge. **(a)** HRTEM image of a crack seen edge-on (i.e., along the $[110]_R$ direction) and **(b)** its magnification detailing the crack's surroundings. The FFT obtained **(c)** at the matrix (far from the crack-edge) and **(d)** at the interface with the crack-edge region. The arrows point the spots appearing around the $2\bar{2}0_R$ reflection, indicating a single spot in (c) and a splitted spot in (d).

Since the strain is partially relaxed near the crack boundaries, one may expect to have a locally different M-I transition temperature and therefore, also contrasting resistances between far and near the crack-edge regions.

To test this hypothesis, films were grown on top of Nb-doped TiO_2 substrates (conductive) and measured the current passing through them (thus, probing changes in film's resistance) with conductive AFM (CAFM). In figure 2.5 it is overlapped the AFM-measured topography of the film near the crack with the current map. The composite 3D-image of fig. 2.5a reveals that the current flowing through the thickness of the film is much lower near the

crack than far from it (about two orders of magnitude). This is consistent with the near-crack region being relaxed into the insulating monoclinic state while the rest of the film is still strained into a rutile metallic phase (note that fig. 2.4 and fig. 2.5 are showing results from different samples; thus, the action field of the strain gradient it is not expected to be the same). Figure 2.5b shows an I(V) curve measured inside a domain, far from a crack. Its linear behaviour indicates an ohmic contact between the metallic AFM-tip and the VO_2 below, confirming that indeed the film is metallic far from the cracks.

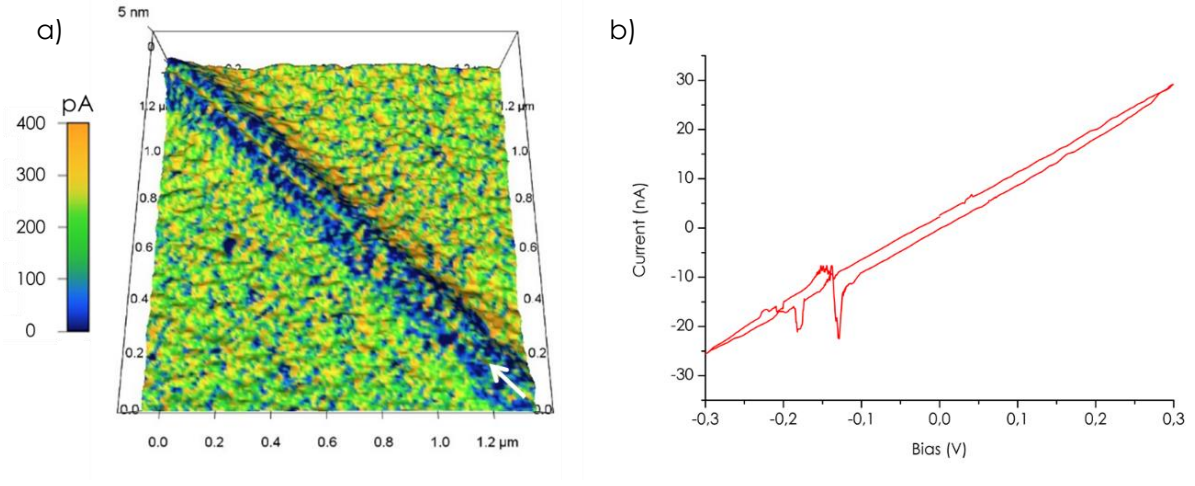

Figure 2.5. VO_2 conduction near and far from a crack-edge in a film of ~36 nm. **(a)** CAFM 3D-image overlapping topography (image relief) and current (colour scale). A white arrow is pointing the crack. The scan is performed at 30 °C, in a perpendicular current configuration with a sample voltage of 77 mV, using a conducting Nb-doped TiO_2 substrate. **(b)** Current versus applied voltage curve of VO_2 inside a domain, far from cracks. The linear dependence indicates that the VO_2 in contact with the tip is metallic.

This sharp conductivity contrast between the film and the crack boundaries will be the basis of the next chapter, where the functional response of these self-patterned electronic structures are described. There is, however, one more notable result from our TEM investigation, and this is the discovery of a new phase that forms a structural tweed.

2.2. NEW INTERMEDIATE PHASE AND TWEED FORMATION IN VO_2

The high-resolution transmission electron microscopy (HRTEM) analysis presented below was performed in regions far from the cracks in a 40 nm thick film; these are the regions that appear metallic and crystallographically rutile-like. Figure 2.6a shows a cross-section HRTEM image of the 40 nm-thick VO_2 film viewed along the $[100]_R$ direction. On a fine (atomic) scale (fig. 2.6b), we notice segments of bright fringes parallel to two prominent directions normal to the arrows labelled x3a and x3b. It can be clearly seen that the fringes triple the periodicity of the dot pattern related to nominal R along the x3a and x3b directions, without any appreciable alteration in the positional order of the atomic columns, which still define a body centered tetragonal lattice consistent with the rutile structure (yellow rectangle). Such fringes are grouped in very small nanodomains 3–6 nm in size.

In agreement with these features, the brightest spots in the FFT can be assigned to the VO_2 rutile structure oriented along the $[100]_R$ zone axis (fig. 2.6c). All other weaker spots (yellow circles) correspond to the tripled periodicity of the $(0\,1\,1)_R$ and $(0\,\bar{1}\,1)_R$ rutile planes and can be, respectively, assigned to the orientational variants denoted by x3a and x3b. Domains with orientations x3a and x3b are related by a mirror plane, m_y, parallel to $(0\,1\,0)_R$ of the underlying rutile ordering (fig. 2.6b,c). A detailed study of the symmetry carried out in these films, shows that the symmetry of this structure must be monoclinic, as reported by Sandiumenge et al. [11].

Figure 2.6d shows a filtered image of the same area obtained by selecting $(0\ \frac{1}{3}\ \frac{1}{3})_R$ and $(0\ \frac{2}{3}\ \frac{2}{3})_R$ spots characteristic of this triple periodicity. The contrast of this image thus maps the spatial distribution of the x3 ordering and defines a tweed texture in which interwoven fringes are attributed to the overlapping of the two orientations along the viewing direction. We can thus infer that, during cooling, the in-plane strained rutile phase undergoes a tweedy texturing transition driven by the symmetry-breaking induced by the x3 order. As

this process preserves the average structure of the precursor rutile template, it is not expected to induce noticeable changes in the X-ray diffraction data presented previously (fig. 2.2a, for instance). Thus, while X-ray diffraction shows this phase to be rutile, and optical microscopy and I(V) curves also show it to be metallic, TEM shows that this is not the standard high-temperature metallic rutile phase of VO_2, but a metallic tweed with a distinct x3 local order. A detailed study of this phase including additional EELS measurements and ab-initio calculations has been performed in the same work by Sandiumenge et al. [11], pointing to the metallic character of the x3M structure.

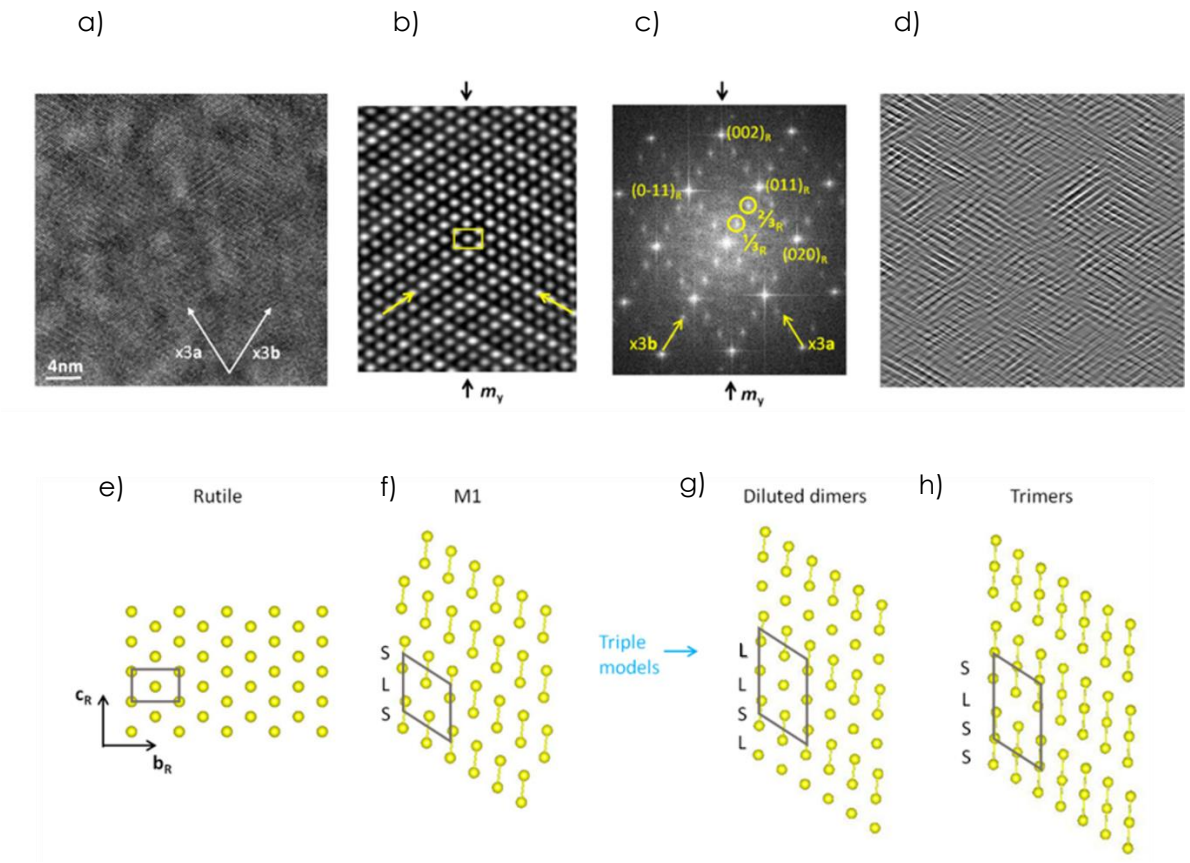

Figure 2.6 [11]. **(a)** HRTEM raw image of the tweed texture observed in the 40 nm -thick film viewed along the rutile $[100]_R$ zone axis. The contrast modulation directions are indicated by arrows labelled x3a and x3b. **(b)** Filtered enlarged view of (a). Arrows indicate the brightest atomic rows defining the contrast modulation. The yellow rectangle highlights the rutile-like body-centered tetragonal arrangement of atomic columns underlying the contrast modulation. The two modulation directions are related by a $(0\ 1\ 0)_R$-type mirror plane, m_y, of the rutile-like lattice. **(c)** FFT pattern obtained from the image shown in (a). The pattern is indexed with reference to the rutile lattice. Superstructure spots arising from the contrast modulation observed in (a)

and (b), $⅓_R$ and $⅔_R$, correspond to $(0\ ⅓\ ⅓)_R$ and $(0\ ⅔\ ⅔)_R$, respectively. The m_y mirror plane is indicated by vertical arrows. Yellow arrows correspond to the modulation directions indicated in (a,b). **(d)** The same image shown in (a), filtered using the $⅓_R$ and $⅔_R$ superstructure spots to highlight the spatial distribution of ordered domains. **(e,f)** Schematic representations of the V-ion arrangement in the rutile and monoclinic M1 lattices projected along the $[1\ 0\ 0]_R$ direction. **(g,h)** Schematic representations of hypothetic V-V dimer arrangements along the c_R-axis direction satisfying the $⅓_R$ and $⅔_R$ superstructure spots observed in the FFT. Long and short V-V distances along the c_R-axis directions are indicated in (f-h) by "L" and "S", respectively. Unit cells are indicated with black lines in (e-h).

In thicker films, the transition towards the standard monoclinic phase brings in an even more complex pattern of phase coexistence. Figure 2.7a shows a HRTEM image of a 80 nm-thick film. The corresponding FFT pattern (fig. 2.7b) is similar to that shown in figure 2.6c, but incorporates a set of additional spots at the $(0\ ½\ ½)_R$, $(0\ 1\ 0)_R$, and $(0\ 0\ 1)_R$ positions. Furthermore, the x3-order spots are more diffuse and the background level is higher, indicating a higher structural disorder than in the 40 nm-thick film. The occurrence of the $(0\ ½\ ½)_R$, $(0\ 1\ 0)_R$, and $(0\ 0\ 1)_R$ spots is consistent with the unit cell doubling associated to the M1 and M2 polymorphs [11, 31]. The double and triple rutile $(0\ 1\ 1)_R$ periodicities observed in the filtered image depicted in figure 2.7c demonstrate the coexistence of [0 1 0] oriented domains of both the M1 and x3-ordered (x3M) phases. The additional spots referred to above are marked in red (fig. 2.7d-g) and indexed in their respective settings in the magnified view of the FFT shown in the right panel of figure 2.7b.

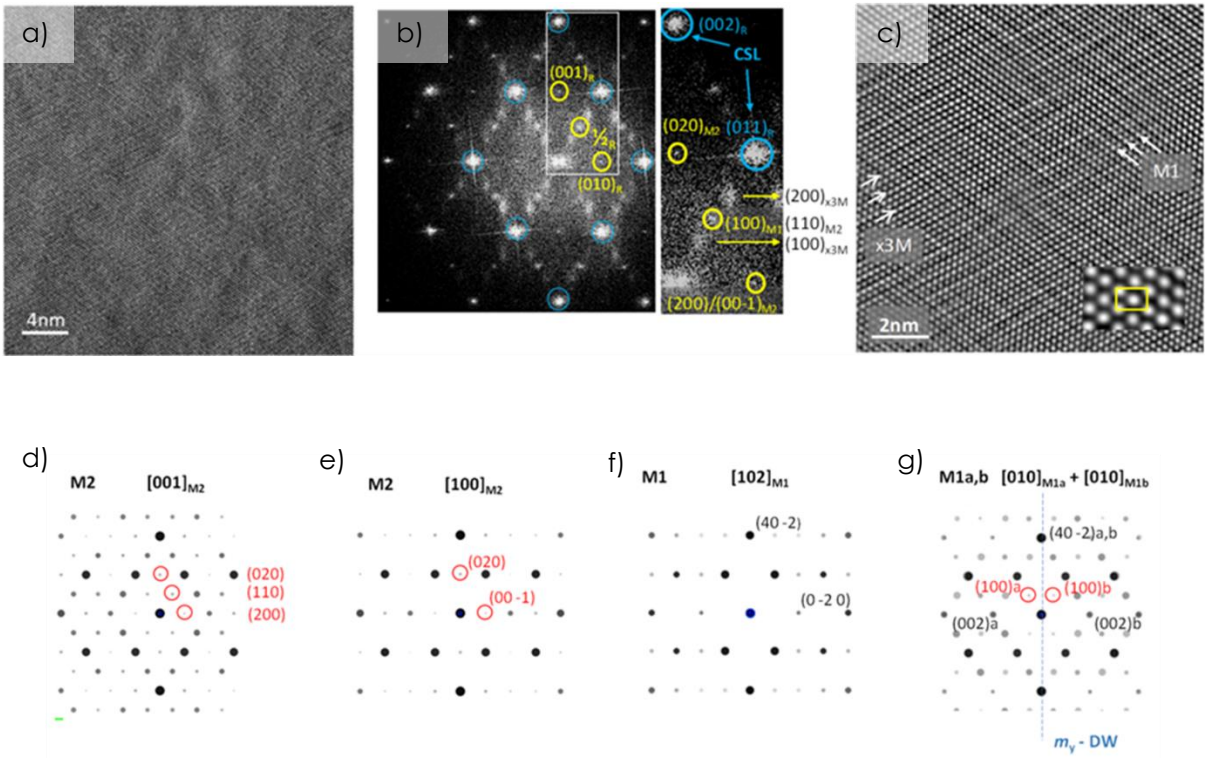

Figure 2.7 [11]. **(a)** HRTEM raw image of the tweed texture observed in the 80 nm -thick film viewed along the rutile $[100]_R$ zone axis. Contrast modulations are weaker and exhibit smaller correlation lengths than in images obtained from the 40 nm -thick film. **(b)** FFT pattern obtained from the image shown in (a). Yellow circles mark additional spots: $(0\ 1\ 0)_R$, $(0\ 0\ 1)_R$, $(0\ ½\ ½)_R$ (labelled $½_R$) with respect to the FFT obtained from the 40 nm -thick film (figure 2.6c). The right panel is an enlarged image of the region enclosed within the white rectangle, indexed in the respective x3M, M1 and M2 settings after the analysis presented in (d-g). The rutile-like spots indicated by blue circles correspond to a coincident site lattice (CSL) defined by overlapping the x3M, M1 and M2 domain orientations coexisting in the tweed. **(c)** Filtered enlarged view of (a). Arrows indicate contrast modulations tripling (x3M) and doubling (M1) the rutile periodicity. The yellow rectangle in the inset highlights the preservation of the body-centered tetragonal arrangement of atomic columns underlying the contrast modulations. **(d-g)** Calculated electron diffraction patterns of M2 **(d,e)** and M1 **(f,g)** domain orientations contributing to the FFT shown in (b). Additional $(0\ 1\ 0)_R$,$(0\ 0\ 1)_R$, $(0\ ½\ ½)_R$ spots are indicated in red color. The orientation of my in (d-f) coincides with the orientation of the mirror plane in the 2/m point group, which makes these orientations hardly discernible from equivalent rutile ones.

According to these observations, the sequence of microstructures observed in the 40 and 80 nm-thick films can be explained by the transformation of the rutile structure into tetragonal-like templates (aka "metrically tetragonal"), formed by coincident site lattices of nanoscale ferroelastic domains of the three monoclinic phases. In the thinner 40 nm film the

dominant phase is a transient monoclinic x3M metallic tweed, whereas the complex structure of the 80 nm thicker film can be described as a cluster composite of x3M, M1, and M2 phases coexisting on an ≈2 nm length scale. Therefore, the electronic phase coexistence in VO_2 occurs at length scales well below those accessed by currently used X-ray spectroscopic imaging techniques, which, combined with the prevalence of the rutile-like structural scaffolding, may explain why this complex structural behaviour had been missed.

2.3. SUMMARY

The canonical MIT of VO_2 refers to bulk material and it is described by a switch in the electronic properties that is coupled to a change in structure. The particular dimerization of V-V chains in the monoclinic M1 phase results in the insulating character of VO_2 while the straight equidistant V-V chains of rutile R allows the metallic behaviour. However, when a mechanical stress is applied the V-V chains distribution will change (and hence the orbital occupancy) so this correlation may not suit anymore. When a substrate like R-TiO_2(001) is used to grow VO_2 films, the mismatch tensile-strain favours the stabilization of R-VO_2 (metallic) at room temperature. As seen in chapter 1, the strain does not relax conventionally with thickness, and the way in which proceeds results in a mesoscopic phase separation toward cracks.

The present chapter has focused on how the microstructure adapts to such high strain in those regions where the film is not yet relaxed. Apparently, standard techniques like XRD showed these domains to be R-VO_2. However, a close-up look through a fine TEM analysis along the $[100]_R$ zone axis has revealed a more complex scenario: these strained domains are not consisted of the standard high-temperature metallic rutile, but a new unreported metastable phase, intermediate between the conventional R and M1 structures, which forms

tweed patterns between 2-6 nm in size. We have named this structure the "x3M" phase because, although a global rutile-like scaffold is preserved, its periodicity is tripled by a local monoclinic symmetry. In addition, x3M is predicted to be metallic by DFT calculations (consistently with optical microscopy contrasts and CAFM measurements inside strained domains). As thickness increases there is a higher structural disorder, the tweed texture decreases its size and reveals phase coexistence consistent with xM3, M1 and M2 within regions of ~2 nm.

Moreover, it has been detailed several features of this new metallic monoclinic x3M phase and its related tweed texture such as,

- In a HRTEM cross-section along the $[100]_R$ zone axis, the tweed texture is only related to the intensities of the atomic columns, but not to the positional order of these atomic columns itself.
- The arrangement of these atomic columns is the nominal rutile-like body-centred tetragonal. However, there is a contrast modulation in this arrangement along a certain directions named x3a and x3b by alternating segments of brighter fringes each 2 darker. Therefore, the brighter fringes are tripling the periodicity of the rutile arrangement.
- The FFT of these features show brighter and weaker spots. The brightest spots are assigned to rutile structure oriented along the zone axis, i.e. $[100]_R$; while the weaker spots triple the periodicity of the $(011)_R$ and $(0\bar{1}1)_R$ rutile planes, thus assigned to the orientational variants x3a and x3b of the x3M phase.
- The x3a and x3b orientations are related by a mirror plane parallel to $(010)_R$ of the rutile arrangement. The tweed texture results from the overlapping of these two orientations in the viewing direction.
- Since there is coincident site lattice between rutile and the x3M, the average structure of rutile remains against the local monoclinic symmetry-breaking, reason why the XRD data does not change noticeably; and this periodicity is related with a diluted

dimerization in a chain where a dimer and an isolated V-atom are alternated in a sequence of long-short-long interatomic distances.

CHAPTER 3.

“Self-Pixelation”

3.0. INTRODUCTION

Since cracks give unique features to the VO_2 films, one could think how to take advantage of them. In chapter 1 and 2, it has shown that phase boundaries either structural (monoclinic/rutile) or electronic (insulating/metallic) are pinned along and parallel to the cracks. Hence, they are not only well localized but also reproducible. Moreover, these fissures stabilize the phase boundaries: the monoclinic-insulating regions surrounding the cracks remain visible in a wide range of temperatures, but the regions become narrower as temperature increases and accordingly, the phase boundaries move –following the lateral strain gradient (see how the position of the dark-metallic/pale-insulating boundaries change in fig. 3.1). Besides, the natural topographic pattern of cracks generally form rectangular domains that somehow remind to pixels with sizes ranging from ~0.25 μm^2 (in films with high-density of cracks) up to 600 μm^2 or even more (in partially cracked or thinnest films). In addition, as it will be shown in this chapter, depending on the biaxial strain distribution, each domain may have its own T_c –what allows different types of "pixel". While still far from technological maturity, all the mentioned features make worthy to study the functionality of this self-pixelation in epitaxial VO_2. This chapter, which led to publication by Rodríguez et al. [12], summarizes the applied exploration.

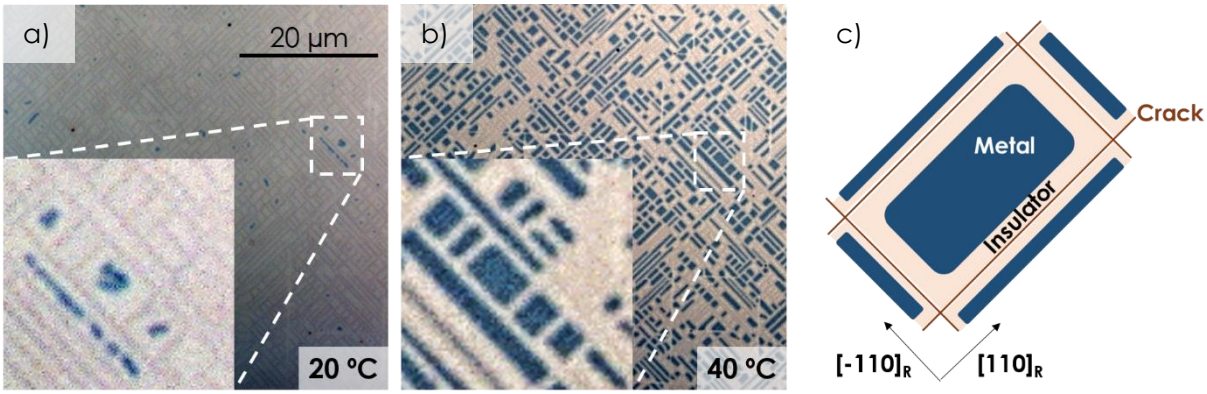

Figure 3.1. Effect of temperature on phase boundaries. Optical images of the same detailed region of a ~ 85 nm thick film at **(a)** 20 °C (below T_c) and **(b)** 40 °C (during the MIT). **(c)** Scheme of a domain. At 20 °C the film is, in average, insulating (pale colour).

The inset in (a) shows that only the fully strained inner regions of a few domains (the farthest from cracks) are metallic (dark regions). In (b), when temperature increases and the MIT is ongoing, much more domains have already transited from insulating to metallic, and their metallic area has increased up to fulfilling the whole domain toward the frame of relaxed VO_2 that surrounds the cracks. Consequently, the metallic/insulating phase boundary has moved.

3.1. EFFECT OF CRACKS ON THE VO_2 PROPERTIES

As seen in previous chapters, the presence of cracks in films of VO_2 has a deep impact in their properties. Normally, the cracking defines a rectangular pattern along the $<110>_R$ crystallographic directions. Since these fissures reach the substrate (fig. 1.6), the resulting VO_2 domains are physically isolated from each other, which certainly, will reduce the possible paths of the current to flow across the in-plane directions. In addition, there is a strain gradient inside the domains generated by the enclosing cracks –due to the elastic energy released perpendicularly to a crack [85, 97]. Because of this strain gradient, the crack-edge region stabilizes the insulating-monoclinic phase of VO_2, while the inner part of the domain is not yet affected by the gradual relaxation and thus, remains at the strained metallic-rutile-like state (fig. 3.1c). As seen in chapter 2, this rutile-like structure is, in fact, the new x3M phase, pure or coexisting with other intermediate phases, forming tweed patterns at the nanoscale [11].

However, the insulating-monoclinic frame becomes wider over time (as well as thermal cycles) from the crack-edge to the inside, occupying a bigger region within the domain in a similar way like happens upon cooling (fig. 3.1 seen in a reverse order, from (b) to (a)). Hence, the strain gradient pushes forward into the domain reducing the volume of strained metallic-rutile-like phase. This spatial evolution must induce the loss of crystal coherence, leading eventually, to structural disorder. If we look back to chapter 1, it is now explained the evolution over time described by the $\bar{1}\bar{1}2_R$ RSMs in figure 1.10.

Furthermore, the strain gradient induces a gradual deformation from the inner region of a domain to the very edge of the crack where irreversible structural distortions due to plasticity can take place. A comprehensive study regarding this topic is in process of being published at the time of writing this thesis, where XRD measurements performed in ICN2 and BESSY II (synchrotron light source) show the effect of these strong strain gradients on the lattice deformation and phase coexistence in the films.

All these consequences related to phase coexistence, strain and strain gradients leave footprints in structural and electrical measurements that can be difficult to interpret without a correlated view.

3.1.1. Effect on microstructure

Figure 3.2 compares the relative volume fraction of rutile (metallic) phase with the resistance as a function of temperature measured simultaneously for the same film (the rutile fraction is calculated from the rutile VO_2 peak intensity at the RSMs around the symmetric 002_R reflection, as shown in the insets of the figure 3.2).

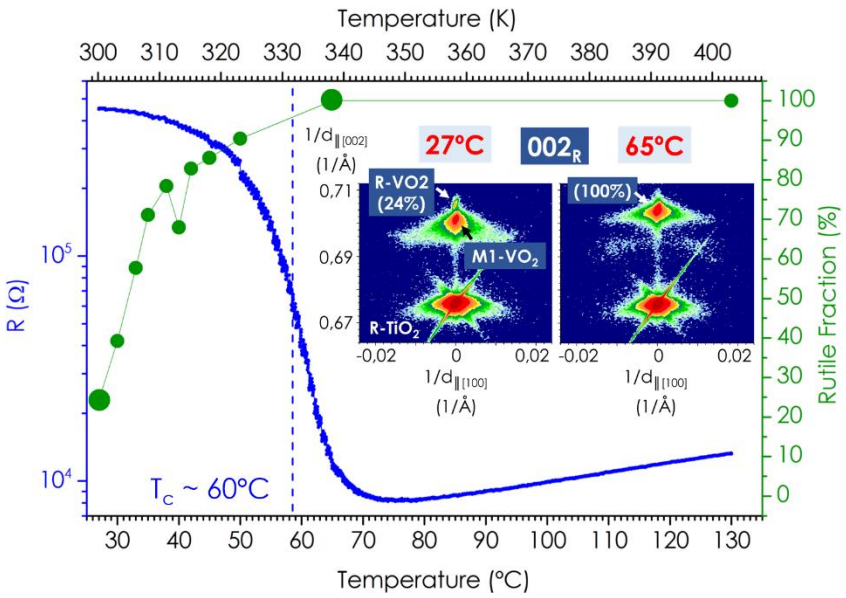

Figure 3.2. Macroscopic electrical transport and the structural phase transition as a function of temperature for a VO_2 film of 85 nm. Resistance (blue curve and axis) was

measured simultaneously with the collection of x-ray RSMs around the 002_R reflection, two examples of which are shown in the inset. The discontinuous vertical line marks the temperature (T) at which d(logR)/dT is maximum, corresponding to the percolative T_c in the electronic transport [98]. The relative volumes of monoclinic and rutile phase (green symbols and axis) were extracted from the integrated intensities of the X-ray peaks (to ease the interpretation it only is represented the rutile phase). Bigger symbols are used to mark the data corresponding to the two representative maps (insets).

This comparison yields the first indication that the macroscopic properties cannot be explained without access to the local microscopic behaviour. Specifically, the result shows that more than 95% of the film needs to be in the rutile (metallic) phase before undergoing the electronic transition to macroscopically metallic transport. Such a high percolation threshold is not consistent with mean-field behaviour, as random-bond models have much lower critical percolation thresholds of 1/3 (in 3D) or 1/2 (in 2D) [98]. Hence, as pointed out in chapter 1, this scenario may lead to an apparent paradox: a macroscopically high-resistance film being at the same time metallic (rutile), in average.

On the other hand, the percolation behaviour must be somehow dependent with the strain gradients toward cracks –because they are regions that stabilize insulating VO_2. At the same time, strain gradients must have some feature in structural characterizations. The 002_R RSMs of insets in fig. 3.2, as well as asymmetric $\bar{1}\bar{1}2_R$ RSMs in previous chapters (fig.I.3d, fig.1.10a-b) show diffraction traces toward the monoclinic peak. These traces are characteristic of our samples and start to appear in films above ~30-35 nm thick. The traces' length and their intensity increases with the density of cracks. Moreover, they are related to irreversible (permanent) deformations in the lattice.

After performing a comprehensive x-ray diffraction study –mentioned before that is in the process of being published, it revealed that involving strong strain gradients, these traces

describe a continuous distortion across the structural transition by means of the intermediate T and M2 (insulating) VO_2 phases, which share the $(111)_R$ contact plane with adjacent rutile domains. Since cracks are contained in $\{110\}_R$ planes and propagated along the $<110>_R$ and $[001]_R$ directions, they are a source of strain gradients [97] and the diffraction traces are related to the insulating T and M2 phases, the whole "structural picture" would be consistent with the effects of crack formation.

Figure 3.3 might be supporting this idea. Contrasts in polarized-light optical microscopy reveal changes in birefringence. An optical image of the same area using natural light (fig. 3.3a) and 45º-polarized light (fig. 3.3b) shows that the insulating regions (pale colours in fig. 3.3a) are actually consisting of two sub-regions (light and dark blue in fig. 3.3b) framing the metallic inner part of the strained domains (orange in fig. 3.3b). Thus, unveiling different optical properties (consistent with the T and M2 phase coexistence reported in our study), along the strain gradient direction. A scheme of this spatial distribution is in fig. 3.3c, emulating the same colours of fig. 3.3b to ease the interpretation.

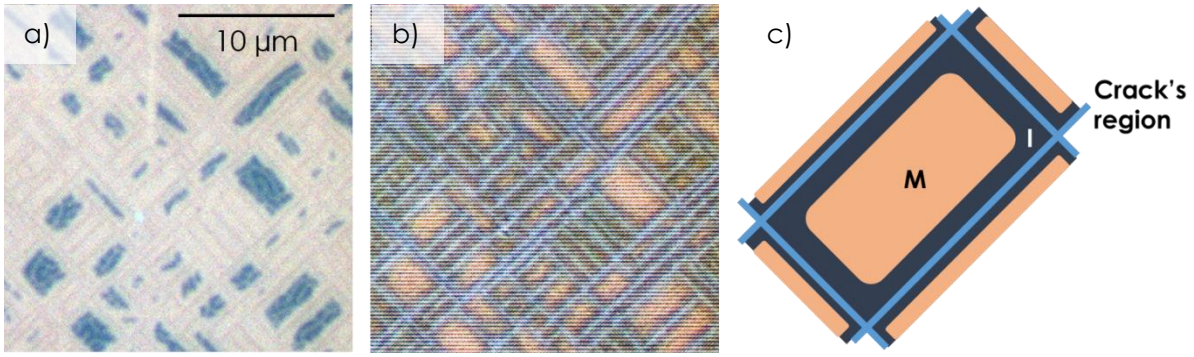

Figure 3.3. Optical microscopy revealing changes in optical properties along the strain gradient direction. **(a)** Image using natural light, showing metallic (dark) and insulating (pale) regions of VO_2 due to changes in optical density. **(b)** Image using 45º-polarized light, were the contrasts evidence changes in birefringence (for instance, due to distortions or changes in the crystal symmetry). **(c)** Scheme to correlate the electronic behaviour (metallic M, insulating I) seen in (a) with changes of birefringence (using the same colours than in (b)).

Consequently, since the cracks extend across the entire surface of the film, if the cracks are decorated by insulating VO_2, the films will still behave macroscopically as insulators. Only when the strain-relaxed gradients near-crack regions have also transitioned into the metallic state (at a higher temperature than the fully strained rutile islands) will there be metallic percolation. All these facts toward strain gradients lead to think that the percolation threshold should increase with the presence of the diffraction traces, and probably, the macroscopic transport could be predicted just by looking at RSMs.

However, during this thesis it was performed only one experiment measuring the electrical and structural transition simultaneously (the one shown in fig. 3.2), and to further validate this hypothesis new experiments should be performed. The determination of the relation between percolation and strain gradients could be worth studying as future work.

Since it is proven that macroscopic properties require a microscopic understanding, we attempted to look at the structure of the strain gradient regions. Given the correlation between structural, electronic and optical properties in VO_2, the local strain relaxation around the cracks may lead to optically visible contrasts, and optical microscopy (fig. 3.4a) and micro-Raman spectroscopy (fig. 3.4b-f) bears this.

As already seen in previous optical images, due to changes in optical density [31] figure 3.4a shows the typical view of insulating edges (pale) following the cracks, framing metallic rectangles (dark). In a similar area, two micro-Raman spectra were taken (fig. 3.4b), one in a highly cracked region (pale) and the other at the inner part of a domain (dark). The spectrum of the dark region (blue curve), which was compared to the spectrum of a rutile (R) TiO_2(001) substrate (inset), revealed R-VO_2 (it is worth noting that the Raman spectrum of R-VO_2 does not have any feature [34], so the spectrum of a R-VO_2 film on a R-TiO_2 substrate will only reveal the substrate's Raman peaks). However, the (orange) spectrum obtained from the

cracked region was consistent with M1-VO_2 [34, 59]. The evolution with temperature of these spectra is shown in fig. 3.4c-d, where it is seen that the dark R-VO_2 domain turned into M1 at ~15 ºC (well-below 68 ºC, the bulk's T_c) meaning a compressive strain along the out-of-plane direction –the c_R lattice parameter of VO_2. On the other hand, the pale M1-VO_2 region turned into R at ~65 ºC (almost the bulk's T_c), meaning that this region has relaxed the c_R lattice parameter. This is consistent with the electronic-structural character in VO_2 under stain, the expected optical contrasts and the existence of a strain gradient toward cracks.

In the case of the M1 micro-Raman spectrum, among many characteristic bands there is an intense peak at ~190 cm^{-1}, which was used to map the spatial distribution of the M1 phase (fig. 3.4e) as well as the distribution of strain gradients (fig. 3.4f). Yellowish colours in fig. 3.4e represent the presence of this peak (black means its absence) across an area with a few domains and cracks. The M1-VO2 distribution defines the cracks and it is constrained to them (there is not M1 inside the domains), as expected.

The shift of a peak, however, is related to changes in the "strength" (the chemical bond length) of the involved atomic bonds. Thus, a shorter bond length results in a blueshift (to higher frequencies) and its elongation leads to a redshift (to lower frequencies). Figure 3.4f shows the same area as the intensity map (fig. 3.4e) but mapping the shift of the studied peak (peak position map). Accordingly, fig. 3.4f shows the distortion (strain gradient) along the out-of-plane (c_R-axis) direction. Yellow represents blueshift (c_R elongation) while dark-orange represents the opposite (black must be understood as the absence of the peak). The map results in a complex distribution of strain around the M1 phase clamped to the cracks, but in general, it seems that the out-of-plane lattice parameter elongates (yellow) toward the inner region of the domains (black, the R-VO_2 boundary).

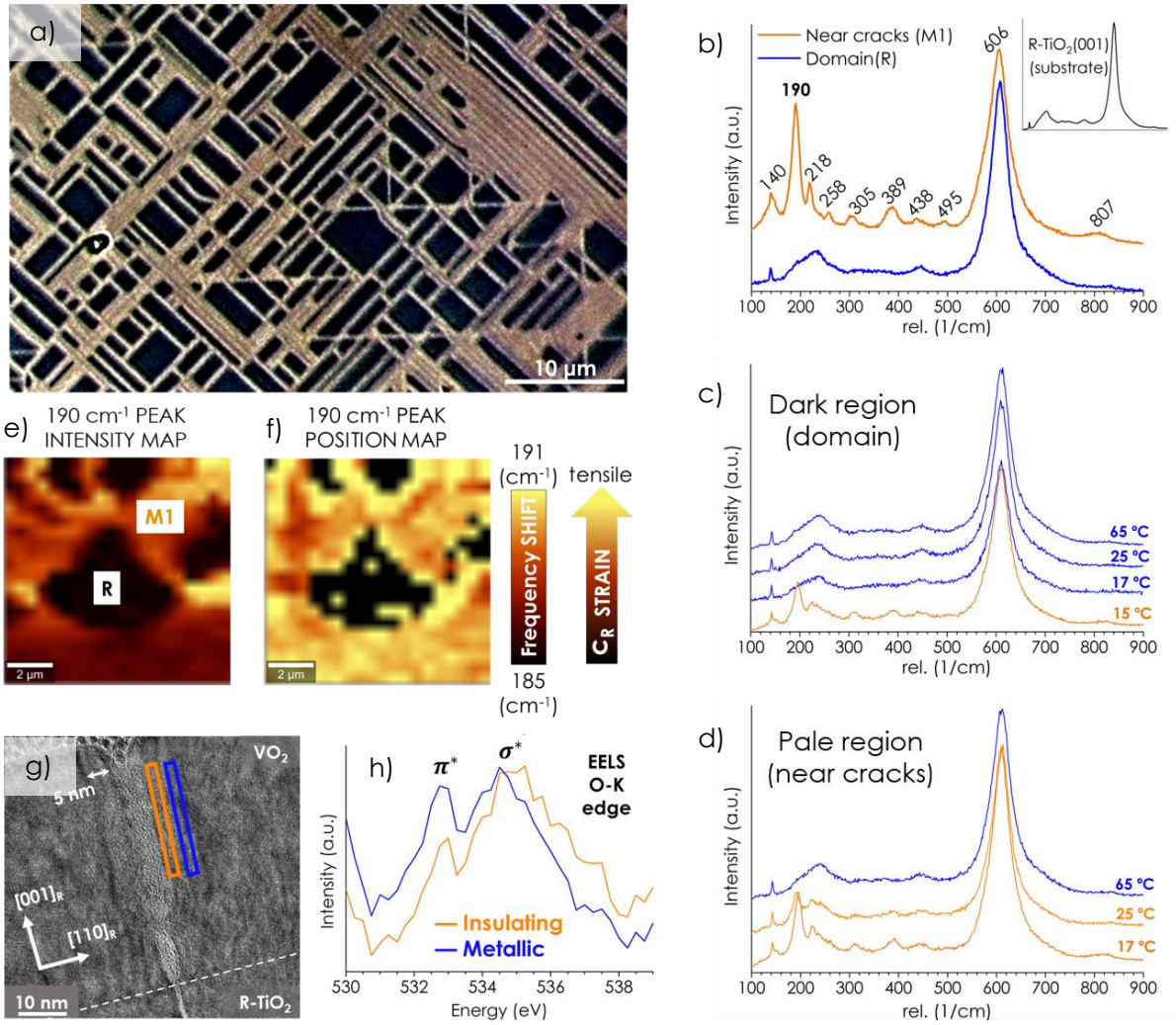

Figure 3.4. Crack-induced MIT and the insulating-M1 phase surrounding the cracks. **(a)** Optical image using natural light showing contrast differences between metallic domains (dark) and insulating near-crack regions (pale). **(b)** Micro-Raman spectroscopy correlating structure with optical contrasts. The inner area of a domain and its framing near-crack region is R and M1, respectively. The evolution with temperature of **(c)** dark and **(d)** pale regions it is shown. The intensity of the characteristic peak of M1-VO_2 around 190 cm^{-1} was used to map **(e)** the M1 presence (yellow) or its absence (black), and its frequency shit to map (f) the strain along the c_R-axis. **(g)** HRTEM cross-section viewed along the $[110]_R$ zone axis showing structural contrast near the crack-edges through the whole film thickness, parallel to $\{111\}_R$ planes. **(h)** O-K EEL spectra obtained from the windows placed near the crack-edge (orange) and farther into the rutile phase (blue), as indicated in (g). These EELS spectra are consistent with the insulating and metallic phases of VO_2.

An inspection of a near-crack region by HRTEM cross-section illustrated in figure 3.4g (also fig. 1.6d of chapter 1), reveals a structural contrast parallel to the crack edge, which is consistent with a M1/R interface as revealed by electron energy loss spectroscopy (EELS).

This technique was used to gain information on O and V states through the O-K (1s → 2p) and V-L (2p → 3d) core edges. In particular, since the O-K edge probes the unoccupied O p density of states (shown in fig. 3.4h), is sensitive to the dimerization of V ions through the strong p-d hybridization [99-101]. Comparison between the two spectra shows that the transition across the interface towards the crack is accompanied by a drop in the intensity of the π* band and a shift of ~ 0.2 eV towards higher energy particularly visible in the σ* band (see fig. I.2d-e of the introductory chapter). Both features are characteristic of the MIT [99]. In other words, the inner region of a domain (blue rectangle in fig. 3.4g) led to a EEL spectrum (blue curve in fig. 3.4h) consistent with metallic VO_2, and the near-crack region (orange rectangle in fig. 3.4g) was consistent with insulating VO_2 (orange curve in fig. 3.4h).

Assembling all the puzzle pieces, seems likely that the structural transformation across the MIT through the T and M2 intermediate phases, might be happening mainly along the strong strain gradients toward cracks, leading to phase boundaries.

3.1.2. Effect on local electronic properties

Atomic force microscopy modes are common techniques to characterize local properties of thin films. In the case of scanning Kelvin probe microscopy (SKPM) –also refered as Kelvin Probe Force Microscopy (KPFM), one can map the work function of the surface by compensating the contact potential difference (CPD) generated between the metallic AFM tip and the sample's surface [102-104]. It is very sensitive to surface phenomena and provides information about composition and electronic state. For example, changes in crystallographic orientation, doping, band bending or charge trapping are detectable for SKPM. Since it measures electrostatic interactions (not current flow) it is a non-contact and non-destructive technique, which makes it suitable for many type of samples and materials (metals, semiconductors, dielectrics, etc), but requires a very clean surface.

On the other hand, conducting atomic force microscopy (CAFM), does measure in contact mode current flow across the sample through two electrodes (one is the metallic AFM tip, and the other typically is a conductive substrate). The current flow depends on the sample's resistance and the applied voltage, as well as contact conditions between the tip and film's surface (contact area, humidity, adsorbates, etc).

Figure 3.5 compares three images at 30 ºC showing the same area of 5x5 μm^2 by performing different microscopies that give access to the local electronic properties of our films. The optical density contrasts (fig. 3.5a) indicate that metallic (dark) domains are framed by the insulating (pale) near-crack regions. However, the corresponding SKPM (fig. 3.5b) and CAFM (fig. 3.5c) maps reveals that each domain has a different surface potential (thus, work function) and conductivity, which is not reflected in such detail by optical microscopy. Among these three techniques, the safest way to stablish the local metal-insulator state is by means of current-vs-voltage spectroscopy, I(V) curves, like the one in fig. 3.5d, taken on the near-crack region marked with a green dot in fig. 3.5c. The I(V) signal is represented by two curves that contain the same information at different scales (see fig. A4).

The measurement shows a rectifying contact between the metallic tip and the material below (thus, semiconductor VO_2), consistent with the optical contrasts in fig. 3.5a (pale, insulating near-crack region); or like shown in figure 2.5b of chapter 2, metallic conduction of VO_2 at the inner region of a domain (still strained because of being far from the crack's strain-gradient field).

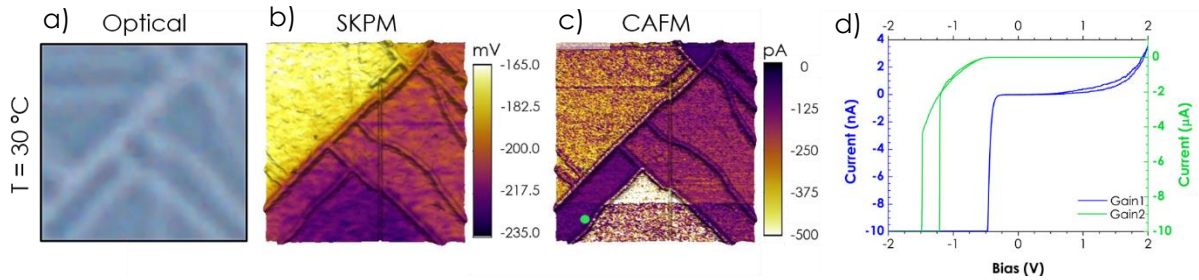

Figure 3.5. Effect of cracks on local electronic properties at 30 °C. The same area of 5x5 μm^2 by **(a)** optical microscopy, **(b)** SKPM and **(c)** CAFM. **(d)** A current vs voltage I(V) curve was taken at the point marked with a green dot in (c), resulting into a rectifying contact between the metallic AFM tip and the near-crack VO_2. The I(V) signal is represented by two curves, depending on the current scale (signal amplification). The CAFM image was mapped applying ~ -0.3 V.

Without having a local reference of the studied region, it is necessary to correlate some of those methods to ensure the metallic or insulating character to the results. The fact that each domain may have its own electronic characteristics relies on the individual strain state within each domain. The cracks enclosing a domain result in a particular contour that generates a unique strain gradient distribution, which determines the local electronic properties of each domain. Since VO_2 is prone to change its oxidation state, it is convenient to avoid electrochemistry and friction (although it is not shown, during this thesis it was observed that contact scans decrease the conductivity of the scanned area). CAFM requires both current flow and scanning in contact, therefore, systematic studies to characterize local electronic properties of the same area were performed by SKPM.

The way strain gradients differentiates the domain's electronic features from its neighbours made wondering how the domains behave across the MIT. Figure 3.6 studies the dependence of the work function with temperature by means of SKPM, in a zone close to regions characterized previously –the ones related to figure 3.4b-f and figure 3.5 (a black square in fig. 3.6a frames the area studied in fig. 3.5). As noted above, it is required some reference to guide the interpretation of the results toward the metal-insulator behaviour, so with this purpose, it was used optical microscopy.

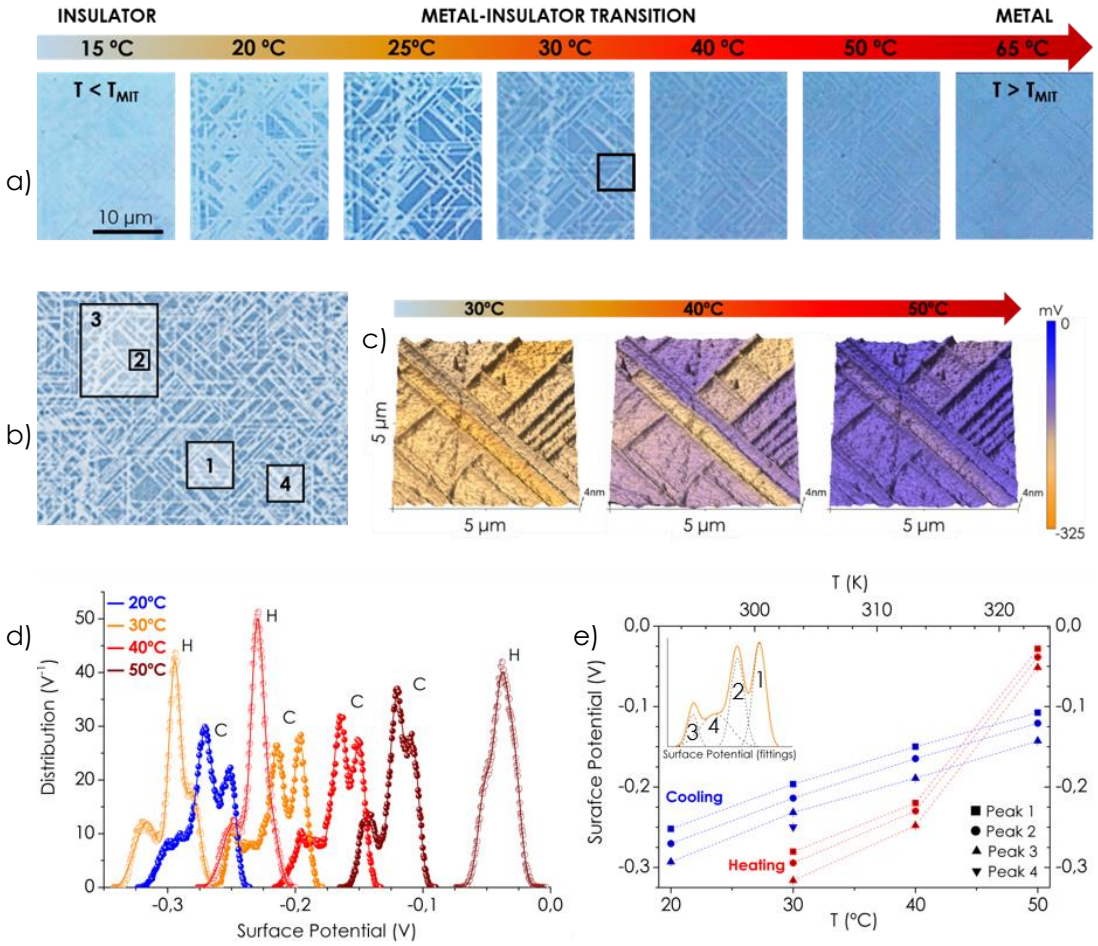

Figure 3.6. Behaviour of the domains across the metal-insulator transition. **(a)** Temperature-dependent optical microscopy images between 15 ºC (insulating state, left image) and 65 ºC (metallic state, right image) showing a representative view of the state of the domains across the MIT, between 20 ºC and 50 ºC. A black square at 30 ºC frames the area studied in figure 3.5. **(b)** Optical microscopy image showing a general view of the 4 regions (black rectangles) studied in this chapter so far. Rectangle 1 refers to fig. 3.4b-f, rectangle 2 refers to fig. 3.5, rectangle 3 refers to (a) and rectangle 4 locates the area where **(c)** a temperature-dependent work function study was performed. Three representative SKPM maps at 30 ºC, 40 ºC and 50 ºC are included to illustrate the **(d)** experimental and fitted surface potential histograms. The positions of the Gaussian peaks used to fit the histograms are plotted in **(e)**, depending on temperature and the cycling period, heating (H) or cooling (C). The relation between Gaussian peaks and peak labelling is detailed in the inset.

Figure 3.6a shows a temperature set of representative optical images, from 15 ºC (insulator) up to 65 ºC (metallic). The general view of figure 3.6b confirms that the four studied regions in this chapter (black rectangles) are equivalent (fig. 3.4b-f as region 1, fig. 3.5 as region 2 and fig. 3.6a as region 3), being consistent with the Raman spectra at 15 ºC

(the domains are M1) and 65 ºC (the near-crack regions are R). Accordingly, the following work function study (in region 4) was carried out within a selected range of temperatures between 20 ºC and 50 ºC.

Figure 3.6c shows these temperature-dependent SKPM maps of a film grown on a conductive substrate of Nb-doped TiO_2(001) connected to bias in this case, with scans at three representative temperatures of the experiment. The height scale is common for the 3 images showing no topography changes across the MIT. The false colour scale is chosen so that blue represents a lower absolute value of the work function (small difference with respect to the metallic tip) while yellow means higher absolute value of the work function.

At 50 °C the surface potential is close to 0 mV (consistent with a metallic state, similar to the tip), while at 30 °C the absolute value of the surface potential is high across the entire surface. Since fig. 3.5a shows dark domains, which means yet metallic, such increase in surface potential might arise from the band energy rearrangement, which likely causes an increase in the metallic VO_2 work function before the opening of the band gap energy (see fig. I.2d-e of the introductory chapter). On the other hand, the SKPM images show that each domain has its own surface potential. The relative differences between them remain regardless of temperature, and those domains with lower surface potential go always ahead to the metallic state (evidenced in fig. 3.6b at 40 ºC). This feature is the strain gradient effect.

In order to quantify this change, the surface potential distributions (histograms) were extracted from all maps, at 20 ºC (blue), 30 ºC (orange), 40 ºC (red) and 50 ºC (brown) performed upon heating (H labels, empty symbols) and cooling (C labels, full symbols) (fig. 3.6d). The histograms were fitted using Gaussian curves, by convoluting 3 peaks except at 30 ºC, where a fourth peak was appropriate. The convoluted curves resulting from the fittings

are included in fig. 3.6d as solid lines over the experimental data, and the Gaussian peaks position is represented in figure 3.6e. (the inset details the peaks identification). Accordingly to histograms (fig. 3.6d), the surface potential changes by about 0.3 V. Taking the surface potential of our tip to be about 5V [104], this would represent a change in surface potential from ~5.3 V (30 ºC) to ~5.0 V (50 ºC), in good agreement with prior studies [81, 105-107]. Moreover, it is worth noting the hysteretic behaviour of the surface potential across this temperature range (a sign of ongoing the MIT), and the different dynamics ruling the heating (likely a power law type) and cooling (linear type with a slope of ~5 mV/ºC). In particular, a power law may be reflecting avalanche dynamics like described for ferroelectric domains switching [108-109] in our films. We tackled the possibility of having a combined time- and space-avalanche dynamics due to the crack-pattern and the induced strain-gradients, and it is being investigated at the time of writing this thesis. This ongoing work could be of great interest to unveil phase coexistence phenomena.

In summary, these observations indicate that each domain switches independently from the others, acting as separate units. Cracks thus act as natural barriers that isolate each domain from its neighbours, and such confinement means that it is, in principle, possible to modify the electronic properties of each individual domain.

3.2. APPLICATION: THE "SELF-PIXELATION" CONCEPT

Since the MIT of VO_2 is sensitive to orbital occupancy [2, 13-14], we wanted to take advantage of the individual behaviour of the domains to make them work as pixels, switching them between ON and OFF states, inducing the MIT by photoexcitation or electric-field (see scheme in fig. 3.7).

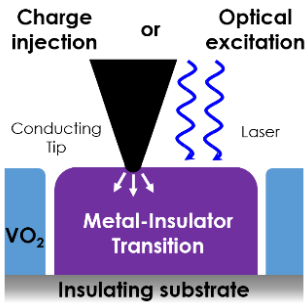

Figure 3.7. Scheme of the pixelation concept. An electrically isolated domain is changing its orbital occupancy by local charge injection using a conducting AFM tip, or by optical excitation using a laser.

Figure 3.8 reveals the result of illuminating an area of our films with a continuous laser (λ = 488 nm; power = 3 mW; exposition = 1 min). It can be seen that the illuminated area has become darker, indicating the transition to the metallic phase. Importantly, each illuminated domain is darker towards the middle but remains unswitched (insulating) towards its edges (the relaxed region surrounding the cracks). This effect can remain from seconds to a day depending on the sample, and is reversible upon cooling.

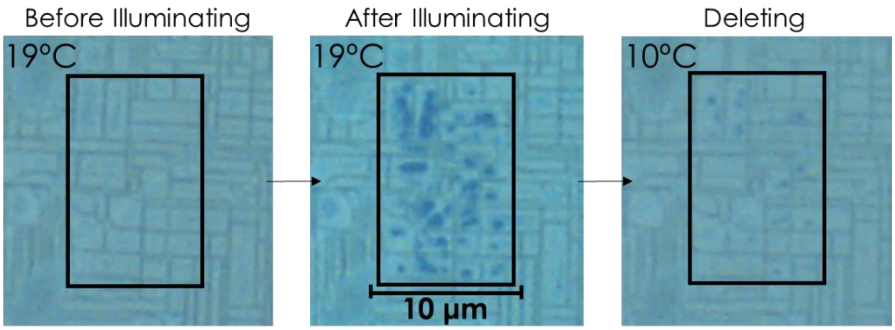

Figure 3.8. Insulator-to-metal transition induced by photoexcitation at 19 °C, using a continuous blue laser (λ = 488 nm) illuminating with a power of 3 mW during 1 min. The optical writing is deleted upon cooling (at 10 °C).

It is also possible to induce the metal-insulator transition by applying an electric field, because charge-injection increases the charge-carrier density and favours the metallic state [110-114]. Here we inject charge by applying a voltage to the conducting-tip of an AFM in contact with an individual domain (fig. 3.9a). The schematic of the experiment and the main

results are shown in figure 3.9. We used a "self-pixelated" VO_2 film of 85 nm grown on insulating TiO_2(001). The surface of the film was grounded (floating for each domain), so the surface potential values have an opposite sign from the ones in figure 3.6c. We measured the surface potential inside and outside an individual island-domain, before and after applying voltage to the AFM tip. The charge-injection and its relaxation behaviour were characterized as a function of temperature and time with a fixed voltage (1 V), and also as a function of both voltage and time at room temperature (RT) (fig. 3.9c).

As temperature increases with no voltage applied, VO_2 switches into the metallic state (fig. 3.9b) and the absolute value of the surface potential decreases (fig. 3.9c), consistent with what was also observed in figure 3.6c for a different film. In the metallic state at temperatures higher than 40 °C, delivering a voltage to the tip has no effect on the surface potential because the film's free carriers screen the tip voltage. At 35 °C or lower temperatures, however, the domain is in the insulating state and applying voltage to the tip does result in charge-injection or extraction from it, as evidenced from the induced change in surface potential.

VO_2 is an n-type conductor [115], so negative voltage injects electrons, increases charge density and pushes the domain towards the metallic state. This shift is evidenced as a lowering of the surface potential after application of negative voltage; the surface potential in a domain written with V = -3 V at RT is the same as that of the high-temperature metallic state. In contrast, positive voltage has the opposite effect of extracting electrons, thereby pushing the already insulating domain into even higher surface potential. In both cases, the voltage-induced changes relax back over time towards the insulating ground state, with exponential time constants sufficiently long (from 6 to 17 minutes depending on temperature and voltage)

for the induced changes to be measurable even by such slow means as scanning probe microscopy.

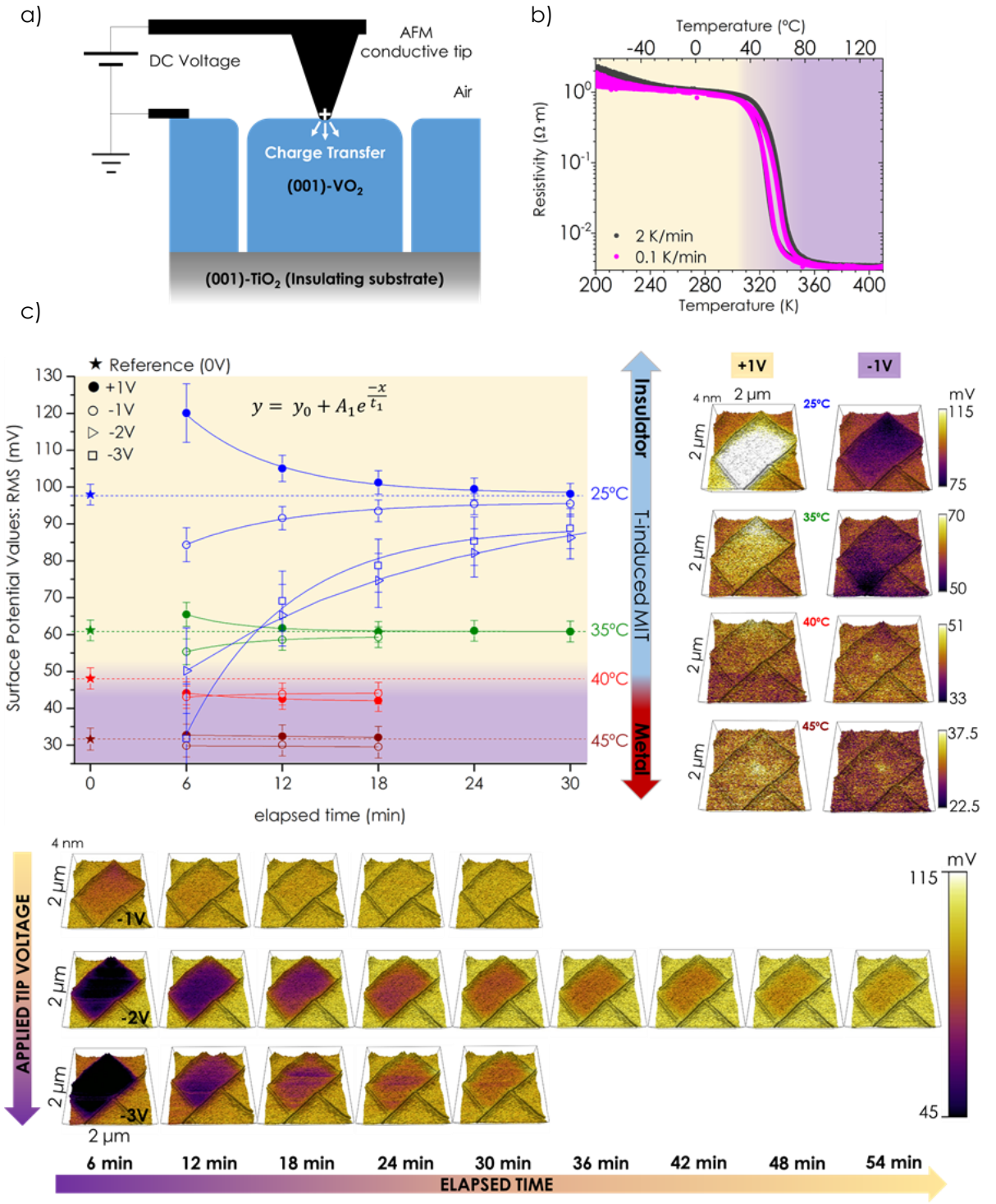

Figure 3.9. Charge-injection into a self-isolated "bit" and its characterization. **(a)** Scheme of the SKPM experiment to study charge-storage in VO2. When the AFM tip contacts the domain's surface a DC voltage is applied to the tip during 10 s. Once

the tip is withdrawn, the tip voltage switches off to 0 V, and a surface potential scan is started immediately. **(b)** Temperature-dependent resistivity of the sample used for the experiment, measured using the temperature rates of 2 K/min (grey curve) and 0.1 K/min (pink curve). The resistivity drop starts ~ 40 °C. The experiment results are represented in **(c)**, where the surface potential RMS values are plotted versus both the temperature and the applied tip voltage. Some of the AFM images used for the analysis are shown.

The transition is not caused by thermal effects (Joule heating from leakage currents), since Joule heating would favour the high-temperature metallic phase for both voltage polarities, whereas we observe that positive voltages favour the insulating phase.

Moreover, the thermalization time constant in thin films should be much faster (microseconds) than the long timescale (minutes) of our measurements, so any heating during the application of the voltage will disappear almost as soon as the voltage is switched off for the Kelvin-probe measurements. The electrostatic origin of the effect is also consistent with the magnitude of the electric field: if we simplify the AFM tip as a conductive sphere with a radius of 50 nm, a voltage of -2 V generates a radial electric field of the order of $\sim 40 \cdot 10^6$ V/m at the contact region, which is of the same order as the reported critical electric fields for inducing the MIT, 10^6-10^7 V/m [112].

Cracking signifies a loss of mechanical integrity and is thus a source of device failure, so it is often studied with a preventive perspective. In recent times, however, cracking is also being embraced as a strategy for device nano-patterning [116].

The self-patterned array of VO_2 is not perfectly regular, and pre-patterning (such as a pre-etching) of the substrates is likely to be necessary in order to achieve perfect registry as required for memory arrays.

3.3. SUMMARY

In bulk VO_2, the MIT occurs abruptly and homogeneously in the material's volume. However, when stress is applied, the response at the mesoscale determines the macroscopic behaviour of the transition. In the case of thin films, the consequences of growing strained VO_2 may have a huge impact, as happens in the samples studied in this work, where mismatch stress induces the films to crack above a critical thickness. This chapter intended to evidence the importance of correlating results from different techniques such as optical and micro-Raman microscopy, TEM, SKPM and I(V) spectroscopy. It summarizes the main consequences of cracking at the local and macroscopic scales, and suggests an application from a conceptual point of view, to take advantage of what in principle, seems a problem.

This application is based on what we have called the "pixelation" concept. It has shown that cracks generates strain gradients within the enclosed VO_2 domains, and the distribution of these gradients depends on the shape of the domain. Consequently, the strain state, and specifically the T_{MIT}, may be different at each domain. This reminds to pixels, where their ON/OFF state would refer to the metallic/insulating state of the domains, which well addressed could be used to "write" and "read" information at the nanoscale. The characterizations regarding these issues have revealed that,

- Cracks stabilize the MIT phase boundaries in a wide range of temperatures. This is because each domain, due to its particular strain gradient distribution, has its own T_{MIT}. Therefore, the collective MIT takes more time than in bulk material, or than in samples with a homogeneous strain distribution.
- The progressive relaxation along the strain gradient makes the phase boundary to move in that direction when temperature changes –in this sense, the phase boundaries can be understood as a moveable "Schottky nanowall". Consequently, it directly affects the macroscopic electrical transport because metallic percolation requires the strain gradient

regions being at the metallic state. It leads to a high percolation threshold, which must depend on the characteristics of the strain gradient toward cracks.

- The strain gradients also affect the VO_2 structure and are strong enough to induce permanent deformations in structure. It can be seen by XRD as traces around the M1 peak, related to a continuous distortion across the MIT mediated by the T and M2 phases. The phase coexistence is given through the $(111)_R$ contact plane, the XRD traces start appearing in samples thicker than 30-35 nm, and their intensity and length increase with the density of cracks (thus, with the reach of the strain gradients).
- Micro-Raman spectroscopy has shown that the M1 phase is only distributed along the cracks, and its out-of-plane lattice parameter is prone to elongate toward the rutile boundaries. Consistently, optical microscopy revealed changes in birefringence suggesting different structures along the strain gradient regions.
- Depending on the strain gradient distribution within a domain, the electronic properties are different from its neighbours. This may lead to domains that, although being all metallic or insulating, have different work functions and conductivities, which in absolute terms, do not provide information about metal or semiconductor VO_2. However, current vs voltage spectroscopy –I(V) curves, is a good tool to stablish unequivocally the metallic or insulating state at the local scale by obtaining, respectively, an linear behaviour (ohmic contact) or a non-linear (rectifying contact).
- Across the MIT, the absolute value of the surface potential (thus, the work function) increases in average ~ 0.3 V toward the insulating state, but each domain has its own surface potential, remaining their relative differences regardless of temperature. Domains with a lower surface potential are always ahead to the metallic state (lower T_{MIT}). This is due to the local effect of strain gradients.
- The average surface potential has hysteretic behaviour but it shows different dynamics at the two parts of the thermal cycle. The heating seems to be ruled by a power law-

like behaviour, which could suggest avalanche dynamics; while the cooling follows a linear-like trend with a surface potential rate of ~5 mV/ºC. At the time of writing this thesis we are exploring this point, and not only the possibility of time-avalanche (T_{MIT} distribution across MIT) but also space-avalanche dynamics (T_{MIT} distribution across domain size).

- The MIT of a domain can also be induced by laser photoexcitation or charge injection applying an electric field with the tip of an AFM. Insulating domains were turned into metallic after illuminating with 3 mW of a continuous 488 nm blue laser during 1 min. The transition can be reverted by decreasing temperature or after some relaxation time, which may take to the order of seconds to days. On the other hand, charge can be injected in a domain by delivering voltages around a few volts. The change in surface potential reflects the carrier type: the absolute value of surface potential increases for positive bias and decreases for the negatives. This is because VO_2 is an n-type semiconductor and therefore, negative voltage injects electrons increasing the charge density, which pushes to the metallic state. Hence, the critical voltage required to induce the MIT should depend on the strain state of the domain (a higher voltage in more relaxed domains). The critical voltage in the reported experiment is -3 V (consistent with reported critical electric fields), and the surface potential relax back to its ground state exponentially, with a time constant of minutes.
- When a domain is already metallic, its free carriers screen the applied tip voltage and no change is observed in the surface potential.
- There is not Joule effect contributing to this voltage-induced MIT.

CHAPTER 4.

Conclusions and future work

The compositional simplicity of VO_2 masks the complexity of its correlated electronic, structural and optical properties. It is a transition metal oxide with strong electron-lattice coupling, making the response of the material sensitive to any tiny perturbation. The interaction between structure and the internal electrostatic fields that it creates within a crystal finds a delicate (and often unstable) balance in this compound. This makes the ground state of VO_2 slippery because it is highly responsive to multiple stimuli, especially stress, voltage or light.

The paradigmatic metal-insulator transition of VO_2, a first-order phase transition at ~ 68 ºC, illustrates these principles. The effect of temperature makes the material jump between two states: at low-temperature the systems finds stability in a semiconducting monoclinic M1 structure; while at high temperature, the ground state is in a metallic tetragonal-rutile R form. However, when any other perturbation is acting on the material, the system readapts to the new conditions by stabilizing intermediate states, either electronic or structural, or both.

Since the MIT in VO_2 depends on the arrangement of V-V chains along the rutile c_R-axis, substrate-induced mechanical stress is a useful tool to explore those metastable phases. In general terms, epitaxy of thin films allows to tune strain by controlling their thickness because the mismatch between substrate and film deforms the structure of the layer, and the stored elastic energy (that will be eventually released) is proportional to the strained material's volume.

However, the optimal growth conditions for making VO_2 films by PLD are narrow, and that makes this part of the process challenging, yet critically important. This is because, in addition to all the possible VO_2 polymorphs, V oxidizes and reduces easily, forming VO_x and Magnéli phases (other phases with different oxygen stoichiometry and therefore different oxidation state of V, departing from nominal +4). Small deviations from nominal growth conditions within tens of degrees of deposition temperature or mTorr of oxygen gas pressure may result in crystallographic quality detriment, polycrystalline films, and mixtures of either

polymorphs or off-stoichiometric compositions. The target, together with the substrate characteristics, will also affect the deposition conditions; and the substrate treatment will determine the interface with the layer –which affects the crystal quality, the properties of the film and the stabilization of the VO_2 phase. Since the collateral effects of strain in VO_2 could be misunderstood as a sign of sub-optimal film's quality, the certainty of having films with a high crystallographic quality took time. One of the main achievements of this work has been to unambiguously unveil these strain features and make robust statements about the phase diagram of VO_2 under strain.

The obtained VO_2 films had grown c_R-axis oriented, coherently on R-TiO_2(001) substrates. The in-plane tensile strain induces the compression of V-V distances along the out-of-plane direction and the first consequence, as expected, is the lowering of the T_{MIT} by the stabilization of the metallic R-like phase at room temperature (instead of being insulating M1). However, as reported elsewhere, above the critical thickness of ~15 nm the films crack under the excessive epitaxial stress, drawing a mostly rectangular pattern across the surface of the film following the rutile $<110>_R$ directions. This work has shown that the cracks are contained in $\{110\}_R$ planes, reaching and even penetrating into the substrate, thereby transforming the single piece of strained film into multiple smaller volumes of strained VO_2. This has both structural and functional consequences.

Cracking reduces the average of the elastic energy of the system. This energy release occurs perpendicularly to the crack's propagation and stabilizes the insulating M1 phase toward cracks, framing the still-strained inner metallic R-like regions within a domain. Therefore, strain does not relax with thickness homogeneously in the film but does it locally following the crack pattern, resulting in phase separation across a wide range of temperatures where each side of the boundary has its own characteristics, dynamics and time evolution.

This work has revealed that metallic strained VO_2 regions are not the conventional rutile phase, but consist of a new structure that triples the rutile periodicity with a monoclinic symmetry, reason why it has been called x3M. This structure alternates a V-V dimer with an isolated V-atom in a sequence of short-long-long interatomic distances along the c_R direction, and it is predicted metallic consistently with the presented experimental results. The x3M platform has coincident site lattices with rutile as well as dimers like M1 or M2 polymorphs; in other words, while the internal symmetry of the x3M is monoclinic, the shape of the unit cell is metrically tetragonal. This strain-stable configuration allows a continuous transition at the nanoscale –or even atomic scale, able to host simultaneously (instead of sequentially) other intermediate phases while preserving the high-symmetry rutile scaffold.

In addition, coexistence of different x3M orientations is seen along the $[100]_R$ zone axis as an interwoven tweed pattern of 2-6 nm in size. The orientational variants are related by the $(010)_R$-type mirror plane, and the tweed size is bigger in thinner samples. When thickness increases, the tweed pattern corresponds to coexistence of xM3, M2 and M1 phases, and the structural disorder is higher.

These facts (revealed by HRTEM) make the x3M phase undistinguishable from tetragonal-rutile by average techniques like XRD. Nevertheless, reciprocal space maps can capture the footprint of the phase coexistence and the related distortions within the film. The RSMs of films above ~35 nm are characterized by diffraction traces coming out of the M1 peak in a certain directions. These traces reflect the presence a progressive deformation of the film's lattice passing through triclinic T and monoclinic M2 structures, sharing the $(111)_R$ contact plane with rutile-like domains. Moreover, the length (deformation degree) and intensity (fraction of the volume involved) of the traces increases with the relaxation state of the film.

I have also found that, the strain state of the films evolves with time or with thermal cycles, from a fully strained highly coherent film to a more relaxed and disordered structure. Thermal cycles re-crack the film and widen the already-formed cracks, which enlarges the action field of the strain gradients by pushing forward and decreasing the volume of fully strained VO_2 within the domains. At the same time, there is a decrease in their optical density (from dark to lighter optical contrast), suggesting gradual loss of metallicity. Eventually, the film's M-I properties disappear due to structural disorder.

Despite the difficulties, we have managed to make a number of interesting and potentially even useful observations. Thanks to the domains' isolation induced by the cracks that separate them, each domain works effectively as an individual pixel, where the switching between ON/OFF states (switching between the metallic and insulating states of the domains) can be induced locally independently of the rest of the film. The MIT can be induced by applying a voltage with the tip of an AFM (charge injection), or by illuminating with a laser (photoexcitation). Since each film has a unique crack pattern, it might be used as unique identifiers (similar to biometric authentication like fingerprint or eye recognition) or QR nanocodes. However, these are still only conceptual applications far from actual functional devices, and there are many issues to solve first. The first and obvious one is that most real devices would require deterministic control over the crack pattern. In addition, we need to ensure that the gradual degradation of the film due to the combination of epitaxial stress and fatigue induced by cycling across the phase transition can be eliminated. Moreover, the films need to be protected to avoid surface oxidation or reduction, which can result in stoichiometrically different VO_x phases with different electronic properties.

Only once the aforementioned problems are solved, applications based on the pixelation concept can be contemplated. Some ideas for steps in that direction are listed below:

► Lithography: design of crack patterns

Although the uniqueness of a crack pattern in a film has advantages, it is also interesting to have control of it, either to replicate patterns or to design them for specific uses. Hence, one of the first challenges would be to induce the nucleation of cracks in a controlled or guided manner. I believe this could be achieved by substrate's pre-lithography, for example [116].

► Capping: avoiding oxidation and control of crack formation

In several works it is already reported the deposition of a very thin layer on top of the film to avoid the oxidation of its surface, which is always a problem in VO_2. However, it would be worth studying the role of this layer in crack formation and structural disorder. Perhaps, there is a critical thickness of this top layer above which crack formation in the film is avoided (and new relaxation mechanisms would be triggered), and below which this top layer is cracked with the film (interesting to have an electrode for each pixel). The mechanical effect introduced by the additional capping layer is a problem that has not yet been studied and is of both fundamental and practical interest.

► Macroscopic stabilization and characterization of M-I phase boundary

It was attempted to create a more macroscopic metal-insulator phase boundary in the film, in order to study its functional properties. The idea was to grow films with a lateral thickness gradient. After testing different growth procedures, I managed to make an adequate sample but there was no time to explore beyond optical microscopy or fast AFM and XRD scans (see figure 4.1). These type of samples together with the standard ones (homogeneous in thickness) were used for avalanche studies to determine the dynamics depending on temperature and domain size, and the preliminary results show a power law behaviour in

some cases. This ongoing work is worth investigating to obtain information about the mechanisms ruling the MIT.

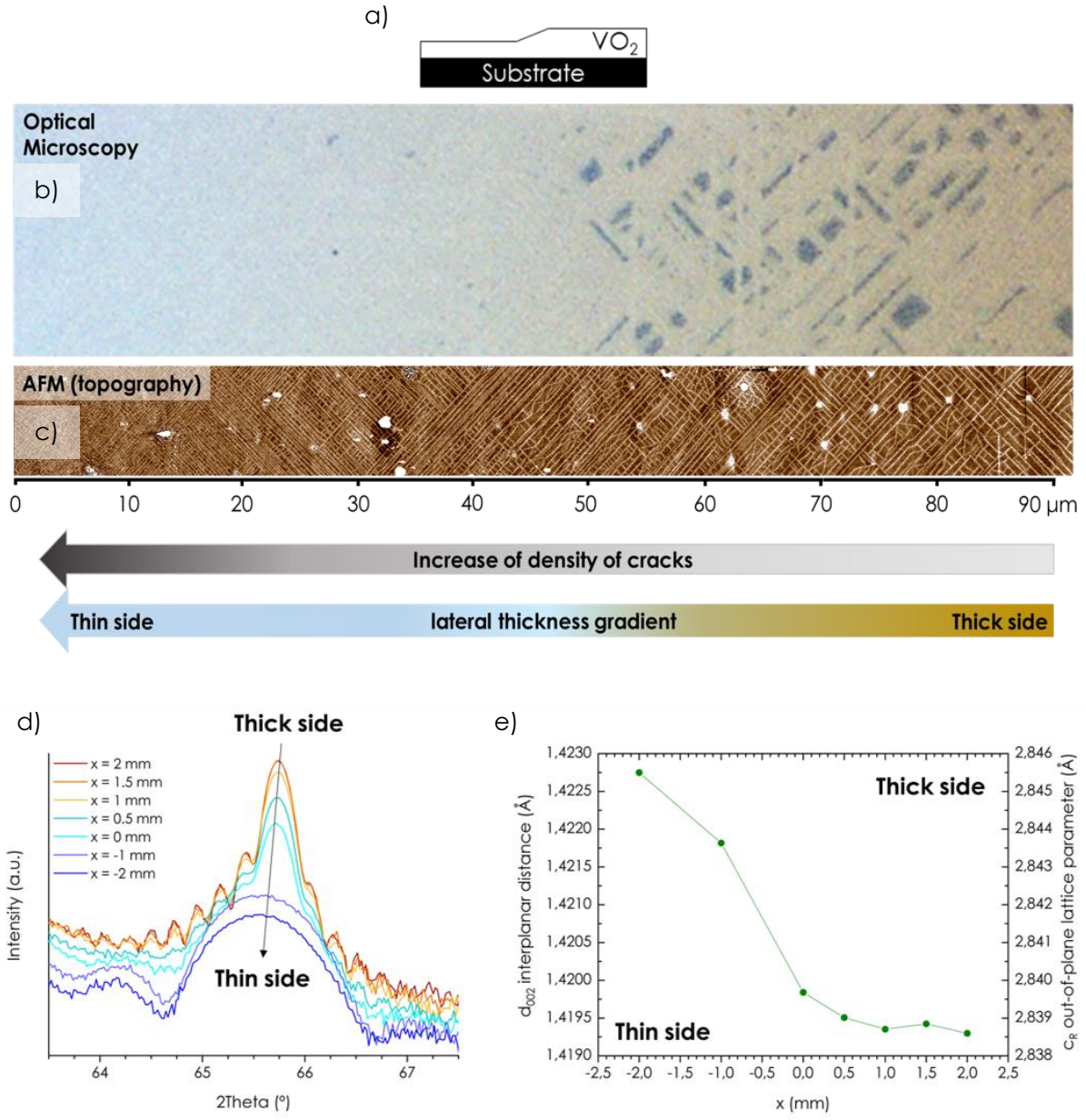

Figure 4.1. Preliminary results in a sample with a lateral thickness gradient that has a thick and thin side around ~85 nm and ~25 nm, respectively. In **(a)** it is depicted a cross-section scheme of the film. The surface of two different regions of the sample along approximately the same lateral thickness gradient range is shown by **(b)** optical microscopy using natural light and **(c)** a sequence of topography AFM images, around the same magnification to ease the comparison of both view types. Some fast XRD measurements were perform across practically the whole sample, along the lateral (x-direction) thickness gradient. **(d)** $2\theta/\omega$ scans around the symmetric 002_R reflection of TiO_2(001) show the VO_2 peak evolution from the thick to the thin side (the arrow direction). The collected out-of-plane information is represented for each peak in terms of **(e)** the related d_{002} interplanar distances and the associated rutile c_R lattice

parameter, showing the evolution along the x-direction. Comparing to bulk R-VO_2 (with c_R ~ 2.851 Å) the out-of-plane parameter of the film is compressed in both sides of the thickness gradient, especially in the thicker side.

► Neuroscience or neuromorphic devides: modelling brain damage

The dynamics of the M-I transition was observed optically, and it displayed avalanche behaviour. Avalanche dynamics exists in other, very different systems, including neural synapses. The aging of our films also reminds to the neuronal behaviour in damaged brains. Therefore, VO_2 might provide a useful platform to simulate and model neuronal processes. This is a topic that was about to be started in collaboration with Dr. Amador Pérez and Dr. Blai Casals, but there was not time enough to go in deep, to develop the ideas and eventually, to perform preliminary experiments. While most of this thesis has been concerned with static properties and/or the induction of the MIT in individual domains, there is a clear scope for future studies focusing on collective dynamics.

► Microfluidics: cracks as filters and transport channels

Besides the pixelation concept, cracks are fissures that can be thought of as channels, opening some chances in microfluidics. The phase separation toward cracks and the possibility of inducing the MIT at each domain makes one wonder whether the related electric fields could capture (or deliver) on the cracks' walls ions, small particles or even smallest viruses (~20 nm in size) flowing through the channels. If that is achieved, the metallic/insulating domains distribution might drive the fluid, opening and closing paths similarly to optical waveguides in optoelectronics, among other possibilities.

The idea itself is out of the scope of this work as well as its real practical implications, and it just intends to inspire new research in the field of microfluidics.

In conclusion, the sensitivity of VO_2 thin films makes them even more challenging to understand than bulk VO_2, but allows access to novel phase coexistence phenomena that opens many possibilities from a fundamental and applicative point of view. This thesis has already covered some of the ground, but the road ahead is still long and, hopefully, rewarding.

ANNEX

A. METHODOLOGIES AND SAMPLES DETAILS

A1. PLD TARGETS

A1.1. Target fabrication

The procedure followed to sinter the V_2O_5 PLD target consisted in grinding the stoichiometric V_2O_5 powder, to press progressively from 5 up to 10 tones and eventually, to bake in air at 650 ºC during 10 hours. It is as shown in figure A1:

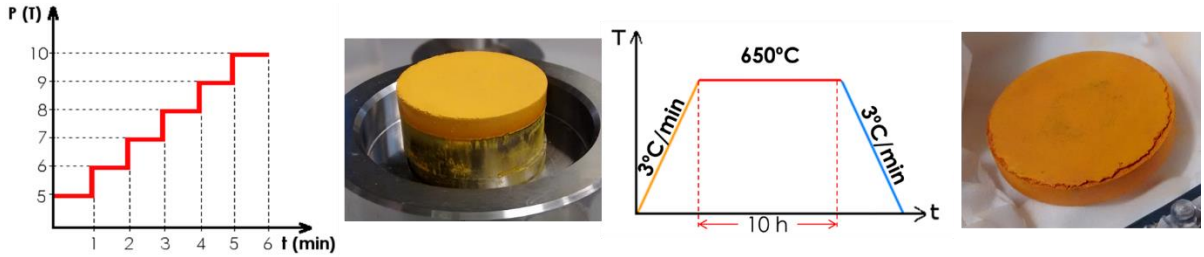

Figure A1. Sintering process of the homemade V_2O_5 target. From left to right, pressing conditions of the V_2O_5 ground powder, the resulting target after pressing and before baking, baking conditions and the resulting target after the baking.

A1.2. Reference XRD patterns

Figure A2 plots the XRD patterns taken as reference to identify peaks of figure 1.1 in the main text. These references are reported in the ICSD database with code numbers 43132 [117], 1536 [118] and 16445 [119], referring to V_2O_5, V_6O_{13} and V_3O_5, respectively.

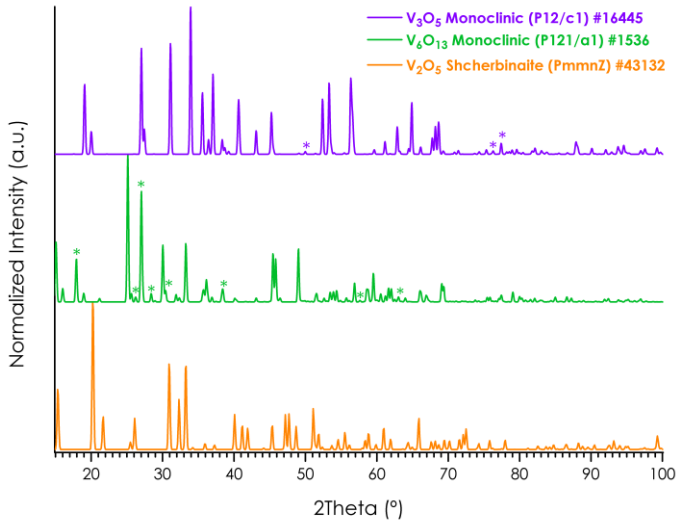

Figure A2. XRD patterns reported in the ICSD database referring to V_2O_5 (orange), V_6O_{13} (green) and V_3O_5 (violet) with ICSD codes 43132, 1536 and 16445, respectively. They have been used to identify the peaks appearing in the experimental XRD patterns of the purchased target, the homemade target and the powder used to fabricate the latter, shown in figure 1.1 of the main text. Here, the star symbols mark the identified peaks of each compound.

A1.3. Samples depending on the target

Figure A3 shows the high resolution XRD scans of two films prepared with the commercial and homemade target. The use of one or another does not make any difference in the quality of the resulting VO_2 films; they are undistinguishable in this sense. Laue oscillations are a sign of high crystallinity and they are present in both type of films. Moreover, the shape, intensity and position of the VO_2 peak is the same independently on the target (the apparent differences are related to differences in thickness, which as shown later, it is something intrinsic of the VO_2 growth, thus not due to the target used).

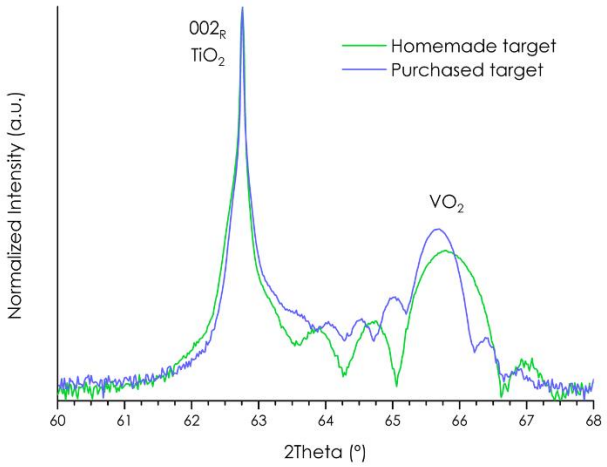

Figure A3. Comparison of V_2O_5 targets by comparing the 2Theta-Theta scans of two resulting VO_2 films of 34 nm (green) and 41 nm (blue), both samples obtained with 1200 pulses under the same growth conditions (the complexity of thickness determination in these films is explained in section 1.1.4 of the main text).

A2. SUBSTRATES

All substrates used in this work have been purchased from CrysTec GmbH.

A2.1. Nb-doped and non-doped TiO_2 lattice parameters

Nb:TiO_2 has larger lattice parameters than TiO_2 (see table A1), however, this deformation is negligible for doping levels below 15% [75]. The Nb-content of the doped substrates used in this thesis is 0.5 wt%, that is 0.43 at.% of Nb (thus, 99.57 at.% Ti). This composition, $(Ti_{0.9957}Nb_{0.0043})O_3$, has much lower Nb content than the minimum reported in table A1, that is already well below the 15% of Nb. Hence, the lattice parameters of Nb(0.5 wt%):TiO_2 are negligibly larger than the ones of non-doped TiO_2.

Table A1. Structural parameters of non-doped rutile TiO_2 [120] and Nb-doped rutile TiO_2 at different compositions [121], $(Ti_{1-x}Nb_x)O_2$.

	COMPOSITION		LATTICE PARAMETERS (Å)		UNIT CELL (Å^3)	REFERENCE
	Ti	Nb	a = b	c	volume	ICSD Code
TiO_2	1	0	4.594	2.959	62.43	23697
Nb:TiO_2 $(Ti_{1-x}\ Nb_x)O_2$	0.952	0.048	4.622	2.976	63.58	97279
	0.912	0.088	4.634	2.989	64.17	97275
	0.84	0.16	4.634	2.989	64.18	97278
	0.736	0.264	4.636	2.990	64.28	97276
	0.712	0.288	4.639	2.990	64.36	97274

A2.2. Nb-doped TiO_2(001) electrical characteristics

Niobium is the most-typical n-type dopant used to tune the electronic properties of stoichiometric TiO_2 by making it conductive (being metallic in a low oxygen partial pressure regime, which depends on temperature) [75, 122]. Substrates suppliers such as Shinkosha Co. [72] and MTI Corp. [73], specify in their website resistivity values of rutile Nb(0.5 wt%):TiO_2 around ~ $3{\cdot}10^{-1}$ Ω·cm (CrysTec had not provided this technical information). An I(V) curve of one of our substrates is shown in figure A4. The current was collected by a conducting Pt/Ir AFM tip that was on the substrate's surface while a bias was applied at the bottom (see the scheme in the inset). The applied bias has a systematic offset of ~ -76 mV, reason why I(0 V) ≠ 0 A. The AFM's cantilever holder has two operational amplifiers with different sensitivities that allow to work from picoamperes up to microamperes. The first amplifier detects the smaller currents (green curve) and actually, it is a zoom of the current signal showed by the second amplifier (blue curve). When the current is higher than 10 nA, the first amplifier saturates and only the second amplifier is able to measure correctly up to its saturation limit, that is 10 μA. Figure A4 shows that CrysTec's substrates are conducting, behaving pretty much like a metal (linear) within ~ [-0.5, +0.5] V of applied voltage, with a

resistivity ~ 10^{-4} Ω·m (calculated supposing an AFM tip diameter of 100 nm and the given substrate thickness of 0.5 mm; see table A2).

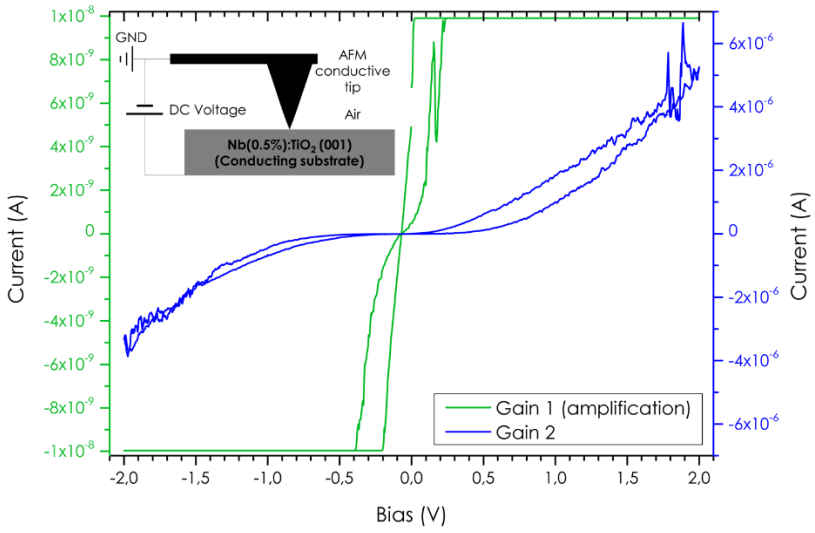

Figure A4. Current versus bias curve on a Nb-doped rutile TiO_2(001) substrate, measured by means of conducting AFM. The inset shows a scheme of the electrical set up. The curves are representing the same current signal but using two different gains. The green curve is the amplification of the blue curve, improving the sensitivity below 10 nA.

A2.3. Substrates Technical data

In table A2 it is detailed the substrates' information that was provided by CrysTec.

Table A2. Characteristics of the TiO_2 substrates used to grow the VO_2 samples.

SUBSTRATE	SIZE (mm)		ORIENTATION			ROUGHNESS
	a x b	c	⊥	Edge	Tolerance	Ra value
Rutile TiO_2 Rutile Nb:TiO_2 (0.5 wt% Nb)	10 x 10 5 x 5	0.5	(001)	‖ (010)	< 0.5 ° (typ. 0.3 °)	< 0.5 nm (typ. 0.25 nm)

A2.4. Substrate Treatments

In this section it is detailed all treatments used to prepare the substrates before growing the VO_2 films, classified in three main groups: no-treatment, cleaning and thermal treatments. In some cases, before any treatment, it was needed to cut substrates by means of a diamond-wire saw (only when needed to cut 10 x 10 mm substrates in 4 pieces of 5 x 5 mm). This procedure makes the substrates dirty. Thus, after the cutting it was required at least, any of the cleaning treatments described below.

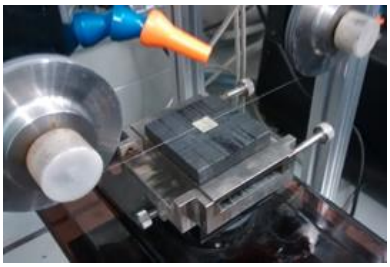

1. NO-TREATMENT

   When substrates were purchased in 5 x 5 mm size, they were not treated in any way.

2. CLEANING TREATMENTS

   2.1. Standard Cleaning (SC)

Using a sonicator, the substrates are first in acetone (99.6%) during 20 min, then in isopropanol (99.9%) during 5 min and rinsed with deionized or ultrapure water (Milli-Q).

   2.2. High-purity HPLC-grade Solvents Cleaning (HPLC)

Using a sonicator, the substrates are in acetone (≥ 99.8%) during 30 min, then in ethanol (≥ 99.9%) during 30 min, rinsed with ultrapure water (Milli-Q) and dried with N_2. Since these solvents are high-pure, they are supposed to be free of metal residues. Thus, no HCl-step is required as part of the cleaning (see thermal treatments below).

3. THERMAL TREATMENTS

3.1. SC + HCl + Furnace thermal treatment:

After a previous SC cleaning, the substrates, without using the sonicator, are now in 37% vol. hydrochloric acid (HCl) during 5 min, rinsed again with deionized or ultrapure water (Milli-Q) and finally dried with N_2.

The HCl-step dissolves and removes possible metal particles [76] on the substrate's surface; therefore, in order to prevent etching, this HCl-step was not performed when cleaning Nb-doped TiO_2 substrates. After, they are ready to go into the tube furnace and start the thermal treatment under the following conditions:

- Gas mass flow = 100 sccm of O_2 (99.995%) during the whole annealing process.

- Heating from RT up to 700 ºC, at 20 ºC/min. Plateau at 700 ºC during 15 h. Cooling from 700 ºC down to RT at 30 ºC/min.

3.2. SC + PLD thermal treatment

After a previous SC cleaning, the substrates were annealed at 700 ºC and 10 mTorr O_2 during 20 min inside the PLD chamber before depositing.

The effect of two treatments detailed above (subsections 2.2 and 3.1) on the surface's roughness parameters of rutile TiO_2(001) substrates are shown in figure A5. The lowest value is achieved after performing a thermal treatment, although this is not much different from the

roughness of a cleaning treatment. In any case, as expected without an HF treatment [76], no terraces have been observed; and the roughness values are below and consistent with the information given by CrysTec (see table A2).

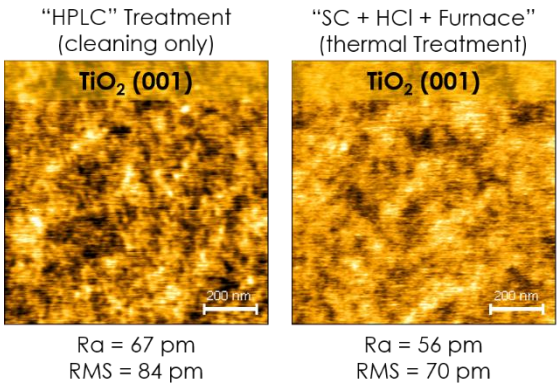

Figure A5. Treatment effect on substrates. AFM topography images showing the surface of a R-TiO_2(001) substrate after (left) an "HPLC" cleaning and (right) after a "SC + HCl + Furnace" thermal treatment. The images' size is 1x1 μm^2, the scale bar is 200 nm and the range of the height false colour bars (not shown) is 500 pm.

The samples obtained during this thesis were grown on substrates that were treated following any of the mentioned procedures (discussed in figure 1.2 of the main text). Regarding the type of substrate, figure A6 merges representative scans selected to show the Nb-doping effect on the VO_2 growth. They compare the same type of films (~70 nm, ~80nm and thicker than 80 nm) grown on HPLC-treated substrates. Films on Nb-doped substrates evolve similarly like the ones on thermally-treated TiO_2 (commented in fig. 1.2 at the main text). This is, stabilizing the M1 phase in films above ~80 nm thick while non-doped TiO_2 allows the R-M1 phase coexistence at thicker films.

Niobium can be consider a point defect in TiO_2 crystals. Nb^{5+} acts as a donor doping when replaces Ti^{4+} in the regular lattice, while on surface, it can also adopt the Nb^{4+} oxidation state [4]. Charge compensation occurs predominantly by electronic or by ionic charge carriers, depending on oxygen and temperature conditions [7]. Since the lattice parameters can be

considered identical in both Nb-doped and non-doped TiO_2, the main difference among them is electronic, causing a similar effect on VO_2 than the thermally-treated substrates.

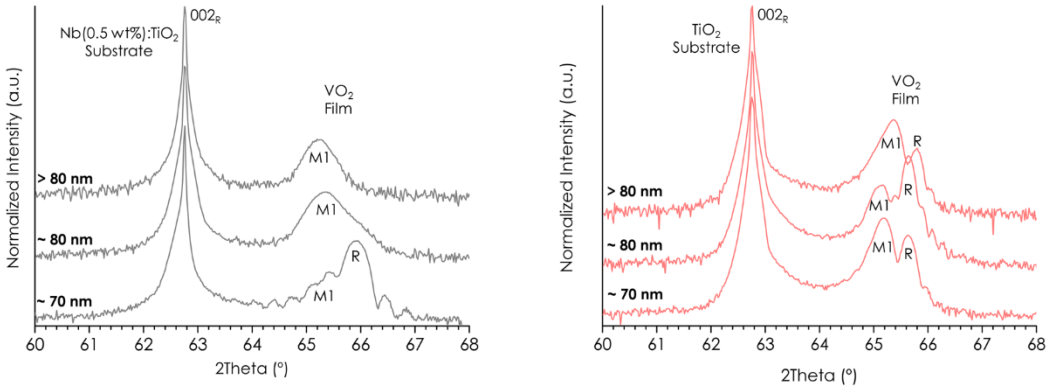

Figure A6. Nb-doping effect on the structural evolution of VO_2 films on Nb-doped (grey curves) and non-doped (salmon curves) TiO_2. Some representative thick films show that Nb makes prone TiO_2 to stabilize M1-VO2 when thickness is above ~80 nm. The substrates were HPLC-treated and the cooling procedure after growing the compared films was the 1-step method (see figure 1.5 in the main text).

A3. THICKNESS UNCERTAINTY

In this thesis, thicknesses have been determined from several ways. Direct observations by performing TEM cross-section and indirect techniques such as XRD or XRR have been used and compared. In the latter case, thicknesses are extracted from Laue oscillations in XRD and Kiessig fringes in XRR. Although their origin is different, the distance between two consecutive oscillations or fringes measure the thickness of the film. The procedure to analyse the data is explained below.

A3.1. Thickness from XRD

Many 2Theta-Theta scans presented Laue oscillations originated by the finite size of the film, its crystallinity. The period of the fringes ΔQ measures the number N of layers with lattice

parameter *a* contributing to the Bragg's intensity of the main peak; thus, the epitaxial thickness of a film [123]:

$$\Delta Q_{Laue} = \frac{2\pi}{N \cdot a} = \frac{2\pi}{\tau_{Laue}} \qquad \text{(eq. A1).}$$

However, X'Pert Epitaxy –the software used to treat the data, directly provides the thickness of a sample and its related error by marking the fringes' position (see right panels of fig. A7). Therefore, the software calculated thicknesses from Laue oscillations.

A3.2. Thickness from XRR

Kiessig fringes result from an interference phenomenon. They are the constructive and destructive interferences appearing by refraction of light (the X-rays) and multiple reflections inside the film between the two interfaces (air-film and film-substrate) separated a distance *d*, similarly to a Fabry-Pérot interferometer. Hence, the crystal structure of the film does not affect the resulting fringes, but the thickness and refractive index of the film do. More concretely, the thickness τ of a layer can be obtained from the period of two adjacent fringes by,

$$\Delta Q_{Kiessig} = \frac{2\pi}{d} = \frac{2\pi}{\tau_{Kiessig}} \qquad \text{(eq. A2).}$$

Using the X'Pert Reflectivity software, the thickness of a film is directly given by the Fourier and Direct methods. The first one shows all the frequencies related to fringes present in the XRR in terms of thickness (see left panels of fig. A7). The second calculates the thickness from the distance between two consecutive fringes.

Despite the theoretical simplicity to obtain thicknesses, the results differ depending on the method used. For instance, the Fourier method shows in mostly all samples a continuous multiple frequency curve, being hard to determine the real thickness, and the direct method gives increasing thicknesses as the incident angle increases.

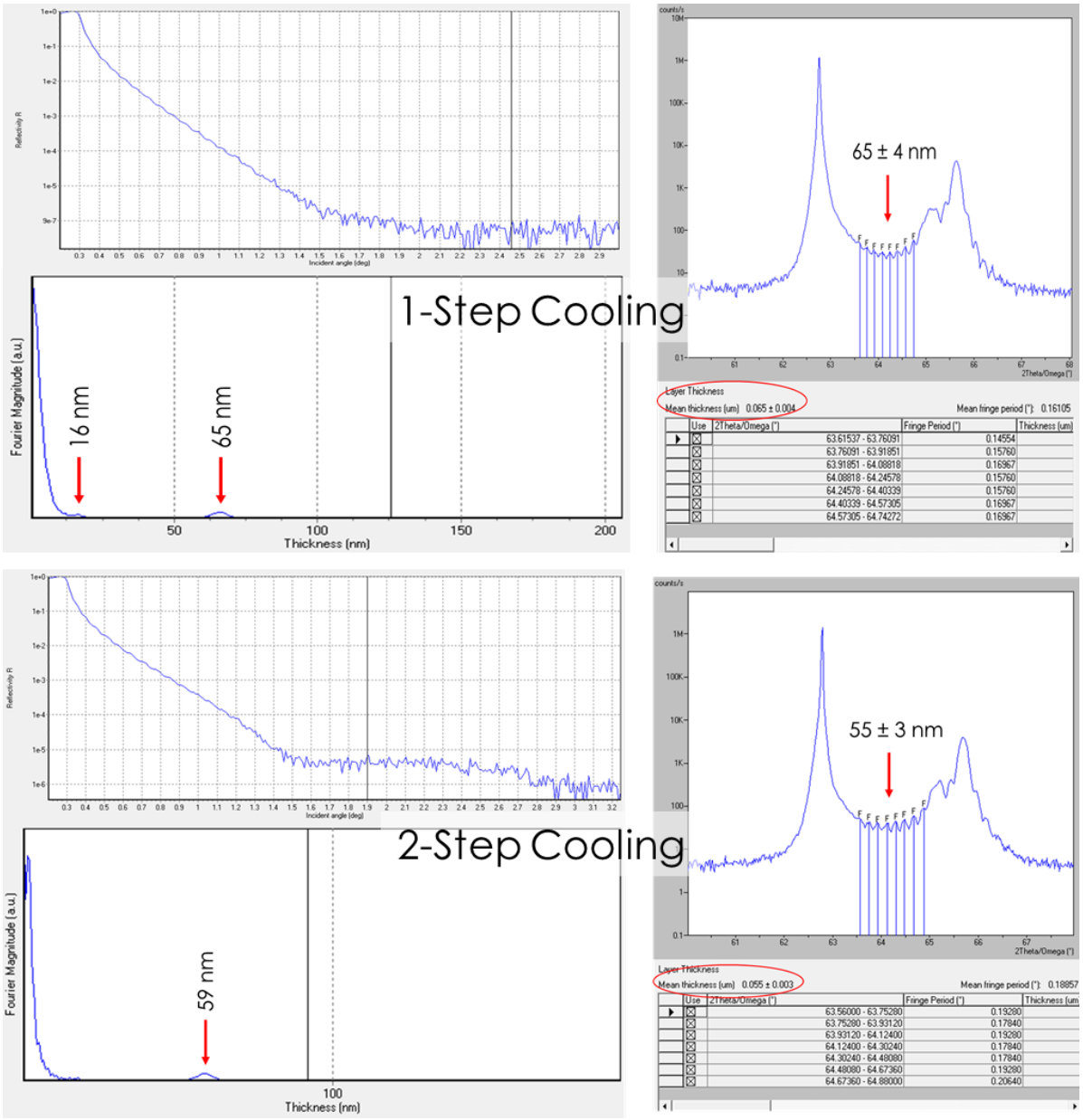

Figure A7. Thickness inconsistencies depending on the characterization technique and the cooling down process. Screenshots showing the software used (X'Pert Reflectivity) to determine thicknesses from XRR (left panels) and XRD 2Theta-Theta scans (right panels). The upper panels depict discrepancies between the results obtained by the two techniques for a sample cooled down with a 1-Step process. Contrary, the panels below show the case of consistent results in a sample cooled down by a 2-Step process.

A3.3. Thickness determination

For all this inconsistencies, the analysis was carried out by comparing thicknesses obtained from 4 methods, on 32 from the 45 samples. The methods were the following:

(a) Fourier method: given by the X'Pert Reflectivity software, already mentioned. It may not be as accurate as simulations or fittings, but it is reliable enough. The results can correspond to the separations of all possible pairs of interfaces within a sample (interfaces where the electron density changes). Therefore, the number of Fourier peaks (related to the angular frequencies ω) can be larger than the layers forming the film. The position Q of the Fourier peaks translates into thickness information while the intensities of the peaks are not clearly defined by the sample properties. The Fast Fourier Transform (FFT) transfers the original (θ, I) data to (Q, I) following equation A3:

$$Q(\omega) = \frac{4\pi}{\lambda}\sqrt{cos^2(\omega_c) - cos^2(\omega)} \qquad \text{(eq. A3)}$$

(b) Direct method: taking advantage of the X'Pert Reflectivity software –which after defining the critical angle θ_c also provides thicknesses (τ) from the distance of a selected pair of consecutive fringes (eq. A4), it was calculated the mean thickness value considering the provided thicknesses from all pairs of consecutive Kiessig fringes (θ_1, θ_2) appearing at the reflectivity curve.

$$\lambda = 2\tau\left[\sqrt{cos^2(\theta_c) - cos^2(\theta_2)} - \sqrt{cos^2(\theta_c) - cos^2(\theta_1)}\right] \qquad \text{(eq. A4)}$$

(c) Maxima-fitting method: the angular position of constructive interferences was used to calculate the thickness by a linear fit (eq. A5).

(d) Minima-fitting method: the angular position of destructive interferences was used to calculate the thickness by a linear fit (eq. A5). This is equivalent to previous method using the minima instead.

$$sin^2\theta = \left(\frac{\lambda}{2\tau}\right)^2 \cdot m^2 + sin^2\theta_c \qquad \text{(eq. A5)}$$

Where θ is the incident angle, λ is the wavelength used (Cu-Kα_1), τ is the thickness and m is the integer number that fits best.

The critical angle is the minimum incident angle above from which the incident light can be refracted (below this angle there is total external reflection and the related evanescence phenomena inside the material). It makes this parameter the basis of grazing incidence XRD, for instance. Since refraction depends on λ, the critical angle does it too. In the case of using X-rays as incident light ($\lambda \sim 1$ Å), the photons only interact with electrons, and consequently, the critical angle only depends on electron density so different critical angles leads to different compositions. In our VO_2 films, it would only be due to changes in oxidation state or interdiffusion, but it was not the case. The XRR scans showed a single intensity-decay around ~0.3 º related to the film's critical angle, indicating a single layer with respect to film's composition.

In many cases, for a single film, the Fourier method (a) led to several thicknesses (being the most recurrent around 2 nm, 10-15 nm and the Laue thickness). The sum of some of them was often consistent toward the expected thickness –calculated from growth rate. However, thicknesses obtained from (b), (c) and (d) were consistent with Laue oscillations, therefore missing some part of the film. Only in several cases, the 4 calculation methods were coincident. Despite the fact that methods (b-d) results in similar thicknesses than Laue oscillations, the missing thickness cannot be an amorphous layer: in that case, it should appear anyway by methods (b-d).

For these reasons, only after having all the results, it was decided that the reliable method to determine an approximate total thickness of these samples would be the Fourier method plus taking into account the trend in the growth rate (provided by TEM observations).

A4. GROWTH RATE DETERMINATION

The resulting thickness-vs-pulses relation has been represented by many parameters such as fluence, the target used to grow, the substrate type, the substrate treatments and the cooling procedure (see fig. A8). After that, the growth rate *GR* was calculated for each case by two different ways:

(1) By a linear fit: $\tau = GR \cdot pulses + \tau_0$ (eq. A6)

(2) Using statistics: Mean value of the experimental growth rate, with its standard deviation.

a)

Growth Rate (GR) and Fluence (F) mean value extracted from the "Thickness vs Pulses" relation

Fluence Range (J/cm²)	points	F ± δF (J/cm²)	mean GR ± δGR (nm/pulse)
[0.75, 1.20]	36	0.864 ± 0.074	0.029 ± 0.006
[1.20, 1.70]	9	1.371 ± 0.120	0.035 ± 0.002

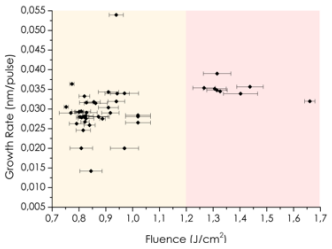

b)

Growth Rate (GR) and Fluence (F) mean value extracted from the "Thickness vs Pulses" relation

	Calculation	points	F ± δF (J/cm²)	GR ± δGR (nm/pulse)	τ₀ ± δτ₀ (nm)	Adj. R²
All measured samples	τ = GR·pulses + τ₀	45	0.965 ± 0.222	0.027 ± 0.001	4.017 ± 2.836	0.896
	GR Mean Value			0.030 ± 0.006	-	-

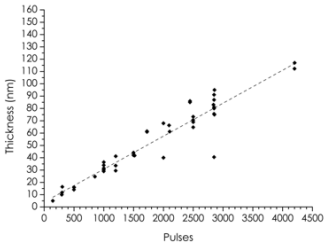

c)

Growth Rate (GR) and Fluence (F) mean value extracted from the "Thickness vs Pulses" relation

Target	Calculation	points	F ± δF (J/cm²)	GR ± δGR (nm/pulse)	τ₀ ± δτ₀ (nm)	Adj. R²
Homemade	τ = GR·pulses + τ₀	21	0.839 ± 0.057	0.025 ± 0.003	4.578 ± 5.471	0.830
	Mean Value			0.028 ± 0.005	-	-
Purchased	τ = GR·pulses + τ₀	24	1.076 ± 0.252	0.028 ± 0.001	3.759 ± 2.891	0.942
	Mean Value			0.033 ± 0.006	-	-

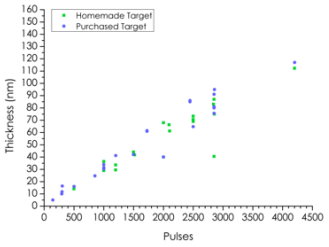

d)

Growth Rate (GR) and Fluence (F) mean value extracted from the "Thickness vs Pulses" relation

Substrate	Calculation	points	F ± δF (J/cm²)	GR ± δGR (nm/pulse)	τ₀ ± δτ₀ (nm)	Adj. R²
TiO_2	τ = GR·pulses + τ₀	37	0.973 ± 0.232	0.027 ± 0.002	4.486 ± 3.205	0.895
	Mean Value			0.031 ± 0.006	-	-
Nb:TiO_2	τ = GR·pulses + τ₀	8	0.929 ± 0.177	0.026 ± 0.003	2.951 ± 5.967	0.905
	Mean Value			0.029 ± 0.006	-	-

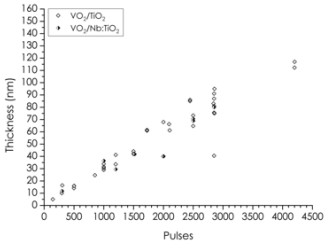

Figure A8. Growth rate calculations depending on **(a)** fluence ranges, **(b)** the whole set of samples measured by XRR, **(c)** the target and **(d)** substrate doping-type.

Fluence is a parameter expected to determine the ablation process. Surprisingly, the growth rate is not affected by changes in this parameter –at least in this fluence range (fig. A8a).

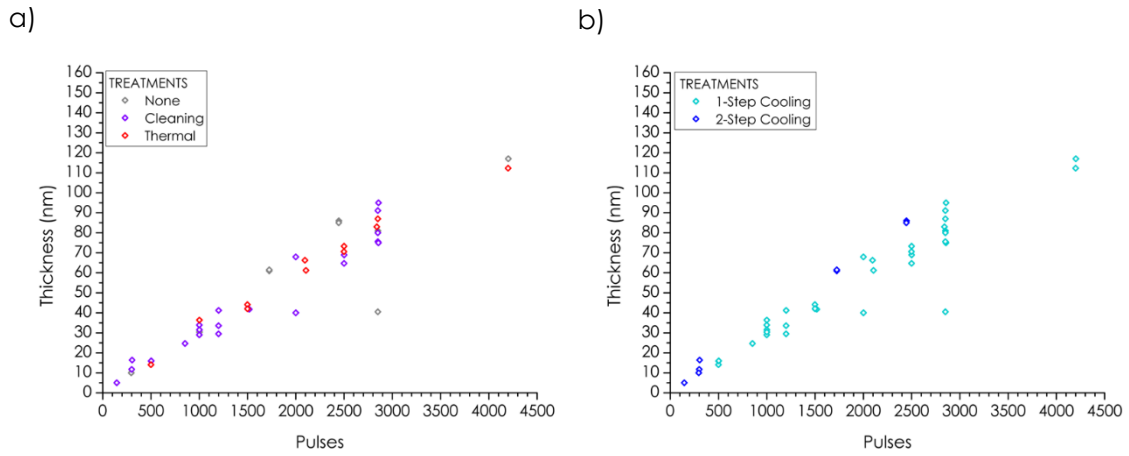

Figure A9. Growth rate calculations depending on **(a)** substrate and **(b)** cooling treatment types. Table A3 summarizes the results on graphs.

The plots, either in fig. A8 or fig. A9, show that thickness dispersion increases with the number of pulses. Since these thicknesses have been obtained by XRR measurements and the problematic of thickness determination has been already explained in detail (section A3), it was likely to have a higher error in thicker films, but of course, other uncontrollable small effects might be contributing to dispersion.

Table A3. Growth rate calculations related to data in figure A9.

	Growth Rate (GR) and Fluence (F) mean value extracted from the "Thickness vs Pulses" relation					
Treatment	Calculation	points	F ± δF (J/cm^2)	GR ± δGR (nm/pulse)	$\tau_0 \pm \delta\tau_0$ (nm)	Adj. R^2
None	$\tau = GR \cdot pulses + \tau_0$	9	1.146 ± 0.249	0.025 ± 0.006	10.152 ± 13.513	0.698
	Mean Value			0.031 ± 0.007	-	-
Cleaning	$\tau = GR \cdot pulses + \tau_0$	25	0.971 ± 0.213	0.027 ± 0.002	2.555 ± 2.817	0.923
	Mean Value			0.031 ± 0.007	-	-
Thermal	$\tau = GR \cdot pulses + \tau_0$	11	0.806 ± 0.024	0.027 ± 0.001	5.524 ± 2.923	0.979
	Mean Value			0.030 ± 0.003	-	-
1-step cooling	$\tau = GR \cdot pulses + \tau_0$	36	0.884 ± 0.152	0.026 ± 0.002	3.253 ± 3.537	0.885
	Mean Value			0.029 ± 0.004	-	-
2-steps cooling	$\tau = GR \cdot pulses + \tau_0$	9	1.291 ± 0.142	0.034 ± 0.001	1.734 ± 0.967	0.997
	Mean Value			0.038 ± 0.006	-	-

Table A4. Growth rate calculations depending on substrate and cooling treatments (part II). The calculations are detailed for each treatment.

Treatment		Growth Rate (GR) and Fluence (F) mean value extracted from the "Thickness vs Pulses" relation					
		Calculation	points	F ± δF (J/cm^2)	GR ± δGR (nm/pulse)	$\tau_0 \pm \delta\tau_0$ (nm)	Adj. R^2
	None	$\tau = GR \cdot pulses + \tau_0$	9	1.146 ± 0.249	0.025 ± 0.006	10.152 ± 13.513	0.698
		Mean Value			0.031 ± 0.007	-	-
Cleaning	HPLC	$\tau = GR \cdot pulses + \tau_0$	21	0.997 ± 0.222	0.027 ± 0.002	2.647 ± 3.122	0.916
		Mean Value			0.032 ± 0.007	-	-
	SC	$\tau = GR \cdot pulses + \tau_0$	4	0.830 ± 0.041	0.027 ± 0.002	-1.691 ± 4.005	0.986
		Mean Value			0.026 ± 0.001	-	-
Thermal	SC+HCl + Thermal	$\tau = GR \cdot pulses + \tau_0$	8	0.807 ± 0.025	0.027 ± 0.001	4.834 ± 3.782	0.979
		Mean Value			0.029 ± 0.001	-	-
	SC + PLD-Thermal	$\tau = GR \cdot pulses + \tau_0$	3	0.801 ± 0.026	0.024 ± 0.004	10.233 ± 7.660	0.936
		Mean Value			0.031 ± 0.005	-	-
1-step cooling	None 1-step cooling	$\tau = GR \cdot pulses + \tau_0$	4	0.896 ± 0.092	0.026 ± 0.011	-3.948 ± 31.810	0.619
		Mean Value			0.025 ± 0.007	-	-
	HPLC 1-step cooling	$\tau = GR \cdot pulses + \tau_0$	17	0.944 ± 0.198	0.028 ± 0.003	1.259 ± 4.777	0.882
		Mean Value			0.029 ± 0.004	-	-
2-steps cooling	None 2-steps cooling	$\tau = GR \cdot pulses + \tau_0$	5	1.345 ± 0.072	0.035 ± 0.000	0.064 ± 0.860	0.999
		Mean Value			0.035 ± 0.001	-	-
	HPLC 2-steps cooling	$\tau = GR \cdot pulses + \tau_0$	4	1.224 ± 0.190	0.054 ± 0.019	-2.839 ± 5.181	0.695
		Mean Value			0.042 ± 0.009	-	-

The first conclusion is that, although thickness' uncertainty increases with pulses, the relation between thickness and pulses is always lineal. Second, the growth rate does not seem to depend on any of the mentioned parameters: the errors of the different growth rates make overlap the growth rates themselves. Therefore, since there is not any clear dependence on treatments, it is realistic to use the common growth rate of (0.030 ± 0.006) nm/pulse (fig. A8b), which is the mean value and its standard deviation (more accurate at thicker films because of the increasing dispersion with thickness).

B. EQUIPMENT AND EXPERIMENTAL CONDITIONS

B1. PULSED LASER DEPOSITION

The ablation was performed in ICN2 by a KrF excimer laser, Lambda Physik COMPex 201, emitting at 248 nm wavelength. It was used a pure oxygen atmosphere during deposition and the cooling down post-deposition.

B2. OPTICAL MICROSCOPY

For a general view of cracks distribution and the related M-I state, most of the films were checked at room temperature by using a Zeiss Axio Observer Z1m optical microscope, with both natural and 45 º-polarized light, in reflection mode. Objectives of 5x, 10x, 20x, 50x and 100x were used. Since metals and insulators interact quite differently with light, images taken using natural light gave information related to changes in electronic properties (optical density, a measure of light attenuation or intensity lost, is higher in metals than in semiconductors or insulators), while polarized light images revealed additional contrast in birefringence related to structural changes.

B3. X-RAY DIFFRACTION

In order to check epitaxy and the structural parameters of our samples, all films were characterized by XRD in a Malvern-Panalytical X'pert Pro MRD, the lab diffractometer, equipped with a 2x Ge(110) monochromator (Cu Kα1 radiation, λ= 1.5406 Å) and a four-angle goniometer. Out-of-plane and in-plane lattice parameters were obtained from symmetric and asymmetric RSMs around the 002_R and $\bar{1}\bar{1}2_R$ reflections respectively, as well as $2\theta/\omega$ scans around the symmetric 002_R reflection, all of them with respect to the R-TiO_2(001) rutile substrates. Thicknesses were estimated from the spacing between interference fringes (Kiessig fringes) in XRR, which were often compared to thicknesses obtained from Laue

oscillations appearing in the symmetric $2\theta/\omega$ scans. In the experiments where the SPT was characterized across the thermal-induced MIT, the sample temperature was controlled by using a DHS1100C Anton Paar sample stage (with non-ambient analysis).

B4. TRANSMISSION ELECTRON MICROSCOPY

The TEM characterizations performed in this thesis were carried out using different microscopes, as part of several collaborations. They were a Thermo Fisher Scientific Titan Cube 60-300, a Thermo-Fisher Scientific FEI double aberration-corrected monochromated Titan Themis Z, and Hitachi HF3300 field emission gun. The lamellae were prepared by focused ion beam (FIB) procedures, and the high-resolution (HR)TEM images were acquired at 300 kV, and EELS was performed in scanning (S)TEM mode. A more detailed explanation about cross-sectional sample preparation and images acquisition at each case is detailed in our published works [11, 12].

B5. SCANNING ELECTRON MICROSCOPY

In a few samples, SEM was also used to check the surface characteristics in secondary electrons mode by means of a FEI Magellan 400L XHR and a FEI Quanta 650FEG ESEM microscopes. The latter was also used in back-scattered electrons mode to see possible changes in crystal orientation (tilts) toward cracks.

B6. ATOMIC FORCE MICROSCOPY

An Asylum MFP-3D Classic AFM was used to characterize the surface of the samples and their local electronic properties at the nanoscale. All experiments were performed in air room conditions, and the samples' temperature was controlled by a heater/cooler holder of the microscope. In general, topography images were taken in AC operation, mainly as part of the

information obtained from the electrical SKPM mode used to probe, but in some specific cases CAFM was also performed. Most of the experiments, like the ones shown in this manuscript, were carried out probing with Pt/Ir conductive-tips, provided by Nanosensors (PPP-EFM type), with a work function of ~ 5.1 eV [104].

B6.1. Scanning Kelvin Probe Microscopy [104]

SKPM technique measures local changes in the work function difference between the AFM's tip and the material below, as it is based on the contact potential principle (eq. B1). When the metallic tip (the reference electrode) and the sample are electrically contacted form an oscillating capacitor. The tip deflects due to the electrical force related to the contact potential difference (CPD), which can be compensated by an external bias that cancels it out, thus, measuring at each point the electrical surface potential of the sample. This AFM mode allows either the sample or the tip groundings. Depending on the electronic circuit configuration, the external DC voltage (V_{DC}) applied to compensate the contact potential difference (V_{CPD}) will be positive or negative (eq. B2-B3), which has to be taken into account in the work function (ϕ) interpretation.

CPD generated when tip and sample are in thermodynamic equilibrium after contact (electrically contacted):

$$\phi_{tip} - \phi_{sample} = -eV_{CPD} \qquad \text{(eq. B1).}$$

CPD compensation when an opposite external bias is applied:

To the tip $\qquad V_{DC} = V_{CPD} = \frac{\phi_{tip} - \phi_{sample}}{|e|} \qquad$ (eq. B2),

or to the sample $\qquad V_{DC} = -V_{CPD} = \frac{\phi_{tip} - \phi_{sample}}{|e|} \qquad$ (eq. B3).

Therefore, for a given tip, the local work function of the sample ϕ_{sample} is a straightforward value (e is the electron charge). On the other hand, despite the general concept of work function refers to the minimum energy required to remove an electron from the solid, it is slightly different in metals than in semiconductors since it involves the Fermi level. In both scenarios however, changes in work function depict a band bending, which is especially interesting in the case of VO_2, where it is expected M-I domains and strain gradients altering the local band structure.

The SKPM method used in this work was in lift mode, which means that each scanned line was probed twice: the first trace detects topography in standard tapping mode and the second trace detects the electrical surface potential (i.e. CPD) by lifting the tip up at a constant distance over the topography line recorded at the first step. This lift height was ~20 nm and the scan frequency was between 1 or 2 Hz.

B6.2. Conducting atomic force microscopy

Local electrical current maps and current-voltage I-V curves were measured in this contact mode. The used cantilever holder was Dual Gain ORCA™, which contains two amplifiers that represent the collected current I in two ranges: from 1 pA up to 10 nA, and larger currents up to 10 μA. However, this holder forces the tip to be always grounded while the voltage is applied on the sample. Since the measurements were performed in a perpendicular current configuration, they show the amount of current passing through the thickness of film. Therefore, films for CAFM measurements were grown on conducting Nb-doped TiO_2 substrates. The sample voltage (up to 10 V) was a DC voltage in current maps while I-V curves were performed using a triangular sample voltage.

Despite the possibilities that current maps bring, it was not used as a routine characterization technique because in general, it was noticed that scans in contact turn the scanned area into more resistive (irrespectively of the tip and even the working operation

mode, standard CAFM or Resiscope™, of two different equipment). Only current maps taken in a first scan might be representative, hence it is not possible to study the local conductivity across the MIT. On the other hand, this resistive effect has not been observed in I-V curves –where although being in contact no lateral friction is involved, and allow determining the metallic or semiconducting local state of VO_2.

B7. MICRO-RAMAN SPECTROSCOPY

Micro-Raman spectroscopy was performed in order to identify the VO_2 structure as well as detecting its changes, by comparing our results with reported spectra. The equipment used to do so was a WITec Alpha 300r spectrometer working with a 488 nm (blue) and 633 nm (red) excitation wavelengths, and 1800 $gr \cdot nm^{-1}$ grating (resulting in a spectral resolution of 1/3 $cm^{-1} \cdot pixel^{-1}$). The laser spot was focused on the sample with a 100x objective, providing a lateral spatial resolution below 500 nm. While XRD averages the structure over the whole film, the phonon spectra collected by the Raman microscope access to the local symmetry with microscopic (optical) resolution. These experiments were performed with the supervision of Dr. Elena del Corro in the ICN2 laboratories.

B8. MACROSCOPIC ELECTRICAL TRANSPORT

Temperature-dependent macroscopic electrical transport measurements were carried out in Van der Pauw 4-probe configuration. The resistance as a function of temperature, R(T), was measured in a closed-cycle cryostat (ARS) with a Lake Shore 336 temperature controller using 4 temperature sensors: DT-670C-SD (sensor A), DT-670B-SD (sensor B), Pt-103 (sensor C) and an E-type thermocouple. Sensors A and C were located close to the sample at the hot stage (see fig. B1), and sensor C was used for the feedback. The resistance was measured by

a Keithley Multimeter 2100 in its (manual) range of 10 MΩ, which has a resolution of 10 Ω and a test DC current of 500 nA.

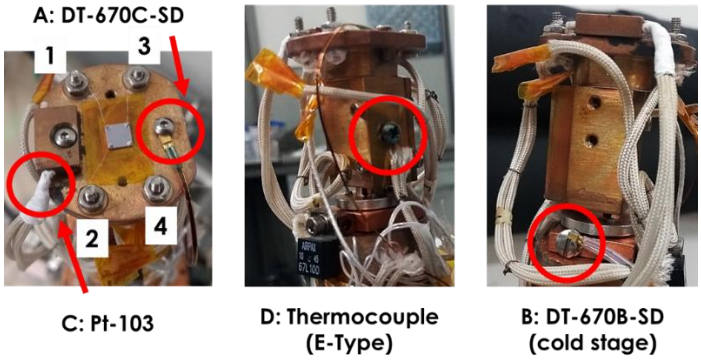

Figure B1. Pictures of the cryostat's sample stage showing the position of the temperature sensors (red circles) and the numbering of the four electrical contacts.

Once the two R_H and R_V resistances are measured (see fig. B2), the software calculates the film's sheet resistance (R_S) by solving the Van der Pauw equation (eq. B4) and estimates the resistivity (ρ) for a certain film thickness (t) by eq. B5:

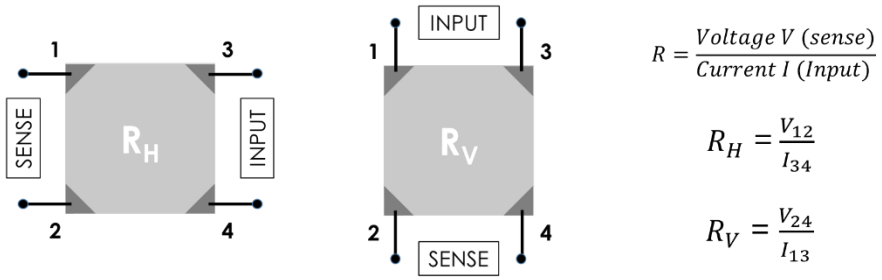

Figure B2. Scheme of Van der Pauw 4-probe measurements in a sample. The four contacts are numbered to define the resistance measurement configurations.

$$e^{-\pi\frac{R_H}{R_S}} + e^{-\pi\frac{R_V}{R_S}} = 1 \qquad \text{(eq. B4)}$$

$$\rho = R_S \cdot t \qquad \text{(eq. B5)}$$

C. ACRONYMS AND SYMBOLS USED

ACRONYMS	DEFINITION
AFM	Atomic Force Microscopy
CAFM	Conducting Atomic Force Microscopy
CPD	Contact Potential Difference (as concept)
EEL(S)	Electron Energy Loss (Spectroscopy)
HRTEM	High Resolution Transmission Electron Microscopy
M-I	Metal-Insulator
MIT	Metal-Insulator Transition
PLD	Pulsed Laser Deposition
RSM(s)	Reciprocal Space Map(s)
RT	Room Temperature
SEM	Scanning Electron Microscopy
SKPM	Scanning Kelvin Probe Microscopy
SPT	Structural Phase Transition
STEM	Scanning Transmission Electron Microscopy
TEM	Transmission Electron Microscopy
XPS	X-ray Photoelectron Spectroscopy
XRD	X-Ray Diffraction
XRR	X-Ray Reflectivity

SYMBOLS	DEFINITION
a_R, b_R, c_R	a, b, c rutile R lattice parameters
a_{M1}, b_{M1}, c_{M1}	a, b, c monoclinic M1 lattice parameters
e	Electron charge (-1.60219·10^{-19} C)
L	Long distance
M1	Monoclinic structure (with space group $P2_1/c$)
$M1_B$	Bulk M1 lattice parameters
M2	Monoclinic structure (with space group C2/m)
M3	Monoclinic structure (with space group P2/m)
Nb	Niobium
$NbTiO_2$, Nb:TiO_2	Niobium doped Titanium Dioxide
R	Rutile (tetragonal) structure (with space group $P4_2/mnm$)
R_B	Bulk R lattice parameters
S	Short distance
T	Temperature
T	Triclinic structure (with space group $P\bar{1}$)
Ti	Titanium
T_c	Critical temperature (equivalent to T_{MIT})
T_{MI} or T_{MIT}	Temperature of the metal-insulator transition
TiO_2	Titanium dioxide
V	Vanadium
V	Voltage
V_{CPD}	Contact Potential Difference (as magnitude)
VO_2	Vanadium dioxide
x3M	Monoclinic structure (with point group 2/m)
ϕ	Work function

ACKNOWLEDGMENTS

Thanks to my ICN2 colleagues, group members and friends:
Sara Martí, Dani Rueda, Rocío Rodríguez, Antonio Benítez, Andrea Bonaccini, Adriana Figueroa, Carlos Marchante, Noemí Contreras, Sonia García, Jose de la Cruz, Nathan Schaefer, Christian Schäfer, Juan Luis Marte, Alejandro Gómez, Marius Vasile, Juan Sierra, Antonio Pablo Pérez, Francisco Belarre, Marcos Rosado, Guillaume Sauthier, Javier Saiz, Ainhoa Ayastuy, Andrés Ballesteros, María Eugenia Herrera, Emma Gómez, Sandra Domene, Inma Caño, Mireia Rivera, Javier Gonzálvez, Javier Dameá, Dámaso Torres, Arkadi Dolgov, Marina Dengra, Manfred and Carles.

Marta Delgà, Pilar Bernícola, Raquel Rodríguez, Carles Rubio, Víctor Fuentes, Anna Magrasso, Núria Bagés, Annalisa Calò, Jackeline Narváez, Kumara Cordero, Fabián Vázquez, Federico Gramazio, James Zapata, Amir Abdollahi, Raquel Núñez, Elzbieta Pach, Irene Sánchez, Adrián Crespo, Xin Wen, Ying Liu, Blai Casals, David Pesquera, Martí Checa, Gabriele de Luca, Christina Stefani, Pablo Vales, Saptam Ganguly, Irena Spasojevic, Arindom Chaterjee, Umesh Bhaskar, José Caicedo Roque, Jéssica Padilla Pantoja, Alba Mingorance, Elena del Corro, Anabel Rodríguez, Pau París, Ismael, Dani, Rafael León, Marc Maymó, Raúl Pérez, Manuela Dietrich, Markos Paradinas, César Moreno, Albert Verdaguer Prats and Felip Sandiumenge Ortiz.

Als meus amics i companys de l'UB:
Eloi Cordomí, Ignasi Reichardt, Elena Prieto, Nacho Moreno, Joan Camuñas, Quico Cortès, Lluc García, Verònica Vidal, Carlos García, Alicia Ruíz, Marc Torres, Omar Olmedo, Isaura, Malu, Manu, Sandra García, Javier García, Eulàlia Fontova, Vanessa Brenes, José Miguel Delgado, Alejandro Ruíz, Harold Moreno, Marta Lluscà, Arevik Musheghyan Avetisyan, Eric Langenberg, Emerson Coy i Jofre Ventura.

Gracias de corazón a Manuel Varela, Cèsar Ferrater, Joan Bertomeu, Maite Fraile, Juan Marcos Fernández y al personal administrativo de la secretaria de postgrado de la Facultad de Física de la UB. Me gustaría mencionar de forma especial a Mª Carmen Polo Trasancos (sin tu ayuda y apoyo esto no hubiera sido posible).

El meu agraïment infinit (per ser-hi simplement, sempre i tant incondicionalment) a Cristian Ayala Alonso, Sílvia Royo del Tormo, Roger Bordoy Molina, Xavier Serch i

Andreu, Alejandro Mateo Tarafa, Teresa García Gálvez, Sergio Alonso Nicolás, Catarina Pinho Siquara, Sonia Martínez Sánchez, Sarah González Díaz, Isabel Acosta Castillo, María Moles de Cara, Gemma Monté Rubio, Carles Sallarès Castejón i Ariadna Sallarès Monté (i la Pamina també!).

De una forma especial y con mucho cariño quiero dar las gracias a Luis Blanco Patús y Elisabeth Ventura, a Oriol González, Mark Murray, Hèctor Rodríguez, Toni Rodríguez, Andrés Navarro, Marta y Míriam Rey Calero, Irene Planas, Biel Miñana, Mary Mateo y Francisco Fontanals, Jaume Fontanals, Pedro Martínez, Julia Herrador, Ana María Maricalva, Julia, i al "Consell de Sàvies" (en especial a Teresa Pages).

M'agradaria dedicar-li també a cinc persones que per diferents motius són importants, i malauradament, quatre d'elles ens van deixar durant el transcurs d'aquesta tesis. Són l'Ana María Gil i en Pedro Requena, Ramón Roya, la Carme Molina i en Miquel Bordoy.

A mi familia:
A mi madre Asunción y a mi Omnipresente José. A mi abuela Dolores Blanco. A mis hermanos Juan Carlos, Maribel e Irene. A mis sobrinos Eloi, Silvia e Irene. A mi cuñado Joaquín Peribáñez. A mis primos (en especial a Toñín Domínguez, Philippe y Jaime Domingo) y a mis tíos Antonio, Félix, Dolores y Angelita Domínguez. También a mi tío Ramón Domingo. A mis mascotas de ahora y siempre: el pequeño Piti; y mi gatos Cuqui y Casper (siempre estaréis presentes), Nina (mi princesa), y mis esquivos Gatalina e Isidoro.
También a Carmen Alonso, Jose Luis Ayala, Eric Ayala y Joel Ayala.

To my supervisors, Gustau Catalan and José Santiso.

To Neus Domingo, Amador Pérez, Borja Sepúlveda, César Magén, J. Miguel A. Pruneda, Shelly Conroy, Kalani Moore, Prof. Etienne Snoeck, Prof. Lukas Eng, Carles Frontera, Belén Ballesteros, Mónica Burriel, Paco Martínez and Louis Pacheco (from CSInstruments).

And many others that in one way or another, helped me, guided me, taught me, opened my eyes and at the end, contributed to make this true.

REFERENCES

[1] Berglund, C. N.; Guggenheim, H. J. Electronic properties of VO2 near the semiconductor-metal transition. *Phys. Rev*. 1969, *185*, 1022–1033.

[2] Zhou, Y.; Ramanathan, S. GaN/VO2 heteroepitaxial pn junctions: Band offset and minority carrier dynamics. *J. Appl. Phys*. 2013, *113*, 213703.

[3] Wentzcovitch, R. M.; Schulz, W. W.; Allen, P. B. VO2: Peierls or Mott-Hubbard? A view from band theory. *Phys. Rev. Lett*. 1994, *72*, 3389–3392.

[4] Eyert, V. The metal-insulator transitions of VO2: A band theoretical approach. *Ann. Phys*. 2002, *11*, 650–704.

[5] Liu, W.-T.; Cao, J.; Fan, W.; Hao, Z.; Martin, M. C.; Shen, Y. R.; Wu, J.; Wang, F. Intrinsic optical properties of vanadium dioxide near the insulator−metal transition. *Nano Lett*. 2011, *11*, 466–470.

[6] Chen, S.; Liu, J.; Luo, H.; Gao, Y. Calculation evidence of staged Mott and Peierls transitions in VO2 revealed by mapping reduced-dimension potential energy surface. *J. Phys. Chem. Lett*. 2015, *6*, 3650–3656.

[7] Fan, L. L.; Wu, Y.; Si, C.; Zou, C.; Qi, Z.; Li, L.; Pan, G.; Wu, Z. Oxygen pressure dependent VO2 crystal film preparation and the interfacial epitaxial growth study. *Thin Solid Films* 2012, *520*, 6124–6129.

[8] Mlyuka, N.; Niklasson, G.; Granqvist, C. Thermochromic multilayer films of VO2 and TiO2 with enhanced transmittance. *Sol. Energy Mater. Sol. Cells* 2009, *93*, 1685–1687.

[9] Saitzek, S.; Guinneton, F.; Guirleo, G.; Sauques, L.; Aguir, K.; Gavarri, J.-R. VO2 thin films deposited on silicon substrates from V2O5 target: Limits in optical switching properties and modelling. *Thin Solid Films* 2008, *516*, 891–897.

[10] Yang, Z.; Ko, C.; Ramanathan, S. Oxide electronics utilizing ultrafast metal-insulator transitions. *Annu. Rev. Mater. Res.* 2011, 41, 337–367.

[11] Sandiumenge, F.; Rodríguez, L.; Pruneda, M.; Magen, C.; Santiso, J.; Catalan, G. Metallic diluted dimerization in VO2 tweeds. *Adv. Mater.* 2021, *33*, 2004374.

[12] Rodríguez, L.; del Corro, E.; Conroy, M.; Moore, K.; Sandiumenge, F.; Domingo, N.; Santiso, J.; Catalan, G. Self-pixelation through fracture in VO2 thin films. *ACS Appl. Electron. Mater.* 2020, *2*, 1433–1439.

[13] Hong, B.; Hu, K.; Tao, Z.; Zhao, J.; Pan, N.; Wang, X.; Lu, M.; Yang, Y.; Luo, Z.; Gao, C. Polymorph separation induced by angle distortion and electron delocalization effect via orbital modification in VO2 epitaxial thin films. *Phys. Rev. B* 2017, *95*, 075433.

[14] Aetukuri, N. P.; Gray, A.; Drouard, M.; Cossale, M.; Gao, l.; H. Reid, A.; Kukreja, R.; Ohldag, H.; A. Jenkins, C.; Arenholz, E.; P. Roche, K.; Durr, H.; G. Samant, M.; Parkin, S. Control of the Metal–Insulator Transition in Vanadium Dioxide by Modifying Orbital Occupancy. *Nat. Phys.* 2013, *9*, 661–666.

[15] D'Elia, A.; Rezvani, S.; Cossaro, A.; Stredansky, M.; Grazioli, C.; Li, B.; Zou, C.; Coreno, M.; Marcelli, A. Strain Induced Orbital Dynamics Across the Metal Insulator Transition in Thin VO2/TiO2(001) Films. *J. Supercond. Novel Magn.* 2020, *33*, 2383–2388.

[16] Grandi, F.; Amaricci, A.; Fabrizio, M. Unraveling the Mott-Peierls intrigue in vanadium dioxide. *Phys. Rev. Res.* 2020, *2*, 013298.

[17] Atkin, J. M.; Berweger, S.; Chavez, E. K.; Raschke, M. B.; Cao, J.; Fan, W.; Wu, J. Strain and temperature dependence of the insulating phases of VO2 near the metal-insulator transition. *Phys. Rev. B* 2012, *85*, 020101.

[18] Mitsuishi, T. On the phase transformation of VO2. *Jpn. J. Appl. Phys.* 1967, *6*, 1060.

[19] Kawada, I.; Kimizuka, N.; Nakahira, M. Crystallographic investigations of the phase transition of VO2. *J. Appl. Crystallogr.* 1971, *4*, 343–347.

[20] Ghedira, M.; Vincent, H.; Marezio, M.; Launay, J. Structural aspects of the metal-insulator transitions in V0.985Al0.015O2. *J. Solid State Chem.* 1977, *22*, 423–438.

[21] Lee, S.; Ivanov, I. N.; Keum, J. K.; Lee, H. N. Epitaxial stabilization and phase instability of VO2 polymorphs. *Sci. Rep.* 2016, *6*, 19621.

[22] Marezio, M.; McWhan, D. B.; Remeika, J. P.; Dernier, P. D. Structural aspects of the metal-insulator transitions in Cr-doped VO2. *Phys. Rev. B* 1972, *5*, 2541–2551.

[23] Qiu, H.; Yang, M.; Dong, Y.; Xu, H.; Hong, B.; Gu, Y.; Yang, Y.; Zou, C.; Luo, Z.; Gao, C. The tetragonal-like to rutile structural phase transition in epitaxial VO2/TiO2 (001) thick films. *New J. Phys.* 2015, *17*, 113016.

[24] Andersson, G. Studies on vanadium oxides. I. Phase Analysis. *Acta chem. Scand*. 1954, *8*, 1599–1606.

[25] Griffiths, C. H.; Eastwood, H. K. Influence of stoichiometry on the metal-semiconductor transition in vanadium dioxide. *J. Appl. Phys.* 1974, *45*, 2201–2206.

[26] Schwingenschlögl, U.; Eyert, V. The vanadium Magnéli phases VnO2n−1. *Ann. Phys.* 2004, *13*, 475–510.

[27] Park, J. H.; Coy, J. M. M.; Kasirga, T. S.; Huang, C.; Fei, Z.; Hunter, S. J.; Cobden, D. H. Measurement of a solid-state triple point at the metal–insulator transition in VO2. *Nature* 2013, *500*, 431–434.

[28] Futaki, H.; Aoki, M. Effects of Various Doping Elements on the Transition Temperature of Vanadium Oxide Semiconductors. *Jpn. J. Appl. Phys.* 1969, *8*, 1008.

[29] Cao, J.; Ertekin, E.; Srinivasan, V.; Fan, W.; Huang, S.; Zheng, H.; Yim, J.; Khanal, D.; Ogletree, D.; Grossman, J.; Wu, J. Strain engineering and one-dimensional organization of metal-insulator domains in single-crystal vanadium dioxide beams. *Nat. Nanotechnol.* 2009, *4*, 732–737.

[30] Fan, L. L.; Chen, S.; Luo, Z. L.; Liu, Q. H.; Wu, Y. F.; Song, L.; Ji, D. X.; Wang, P.; Chu, W. S.; Gao, C.; Zou, C. W.; Wu, Z. Y. Strain dynamics of ultrathin VO2 film grown on TiO2 (001) and the associated phase transition modulation. *Nano Lett.* 2014, *14*, 4036–4043.

[31] Tselev, A.; Strelcov, E.; Luk'yanchuk, I. A.; Budai, J. D.; Tischler, J. Z.; Ivanov, I. N.; Jones, K.; Proksch, R.; Kalinin, S. V.; Kolmakov, A. Interplay between Ferroelastic and

Metal-Insulator Phase Transitions in Strained Quasi-Two-Dimensional VO2 Nanoplatelets. *Nano Lett.* 2010, *10*, 2003–2011.

[32] Mott, N. F. The basis of the electron theory of metals, with special reference to the transition metals. *Proc. Phys. Soc*. 1949, *A62*, 416–422.

[33] Morin, F. J. Oxides which show a metal-to-insulator transition at the Neel temperature. *Phys. Rev. Lett.* 1959, *3*, 34–36.

[34] Chang, S.-J.; Hong, W.-K.; Kim, H. J.; Lee, J. B.; Yoon, J.; Ko, H. C.; Huh, Y. S. Probing the photothermally induced phase transitions in single-crystalline vanadium dioxide nanobeams. *Nanotechnology* 2013, *24*, 345701.

[35] Fan, W.; Huang, S.; Cao, J.; Ertekin, E.; Barrett, C.; Khanal, D.; Grossman, J.; Wu, J. Superelastic metal-insulator phase transition in single-crystal VO2 nanobeams. *Phys. Rev. B* 2009, *80*, 241105.

[36] Kasirga, T. S.; Sun, D.; Park, J. H.; Coy, J. M.; Fei, Z.; Xu, X.; Cobden, D. H. Photoresponse of a strongly correlated material determined by scanning photocurrent microscopy. *Nat. Nanotechnol.* 2012, *7*, 723–727.

[37] Lee, S.; Hippalgaonkar, K.; Yang, F.; Hong, J.; Ko, C.; Suh, J.; Liu, K.; Wang, K.; Urban, J. J.; Zhang, X.; Dames, C.; Hartnoll, S. A.; Delaire, O.; Wu, J. Anomalously low electronic thermal conductivity in metallic vanadium dioxide. *Science* 2017, *355*, 371–374.

[38] Li, Z.; Wu, J.; Hu, Z.; Lin, Y.; Chen, Q.; Guo, Y.; Liu, Y.; Zhao, Y.; Peng, J.; Chu, W. ; Wu, C.; Xie, Y. Imaging metal-like monoclinic phase stabilized by surface coordination effect in vanadium dioxide nanobeam. *Nat. Commun.* 2017, *8*, 15561.

[39] Park, J. H.; Coy, J. M. M.; Kasirga, T. S.; Huang, C.; Fei, Z.; Hunter, S. J.; Cobden, D. H. Measurement of a solid-state triple point at the metal–insulator transition in VO2. *Nature* 2013, *500*, 431–434.

[40] Wei, J.; Wang, Z.; Chen, W.; Cobden, D. H. New aspects of the metal-insulator transition in single-domain vanadium dioxide nanobeams. *Nat. Nanotech.* 2009, *4*, 420–424.

[41] Liu, W.-T.; Cao, J.; Fan, W.; Hao, Z.; Martin, M. C.; Shen, Y. R.; Wu, J.; Wang, F. Intrinsic Optical Properties of Vanadium Dioxide near the Insulator−Metal Transition. *Nano Lett.* 2011, *11*, 466–470.

[42] Gui, Z.; Fan, R.; Chen, X.; Wu, Y. A New Metastable Phase of Needle-like Nanocrystalline VO2·H2O and Phase Transformation. *J. Solid State Chem.* 2001, *157*, 250–254.

[43] Fisher, B.; Patlagan, L. Switching VO2 Single Crystals and Related Phenomena: Sliding Domains and Crack Formation. *Materials* 2017, *10*, 554.

[44] Balakrishnan, V.; Ko, C.; Ramanathan, S. In situ studies on twinning and cracking proximal to insulator–metal transition in self-supported VO2/Si3N4 membranes. *J. Mater. Res.* 2012, *27*, 1476–1481.

[45] Cao, J.; Fan, W.; Zhou, Q.; Sheu, E.; Liu, A.; Barrett, C.; Wu, J. Colossal thermal-mechanical actuation via phase transition in single-crystal VO2 microcantilevers. *J. Appl. Phys.* 2010, *108*, 083538.

[46] Bowman, R. M.; Gregg, J. M. VO2 thin films: growth and the effect of applied strain on their resistance. *J. Mater. Sci.: Mater. Electron.* 1998, *9*, 187–191.

[47] Osmolovskaya, O.; Murin, I.; Smirnov, V.; Osmolovsky, M. Synthesis of vanadium dioxide thin films and nanopowders: a brief review. *Rev. Adv. Mater. Sci.* 2014, *36*, 70–74.

[48] Gray, A. X.; Jeong, J.; Aetukuri, N. P.; Granitzka, P.; Chen, Z.; Kukreja, R.; Higley, D.; Chase, T.; Reid, A. H.; Ohldag, H.; Marcus, M. A.; Scholl, A.; Young, A. T.; Doran, A.; Jenkins, C. A.; Shafer, P.; Arenholz, E.; Samant, M. G.; Parkin, S. S. P.; Dürr, H. A. Correlation-Driven Insulator-Metal Transition in Near-Ideal Vanadium Dioxide Films. *Phys. Rev. Lett.* 2016, *116*, 116403.

[49] Molaei, R.; Bayati, M. R.; Narayan, J. Thin film epitaxy and near bulk semiconductor to metal transition in VO2/NiO/YSZ/Si(001) heterostructures. *J. Mater. Res.* 2012, *27*, 3103–3109.

[50] Song, F.; White Jr, B. Growth of ultra thin vanadium dioxide thin films using magnetron sputtering. arXiv preprint arXiv:1608.03911, 2016.

[51] Kumar, R. T. R.; Karunagaran, B.; Mangalaraj, D.; Narayandass, S. K.; Manoravi, P.; Joseph, M. Characteristics of amorphous VO2 thin films prepared by pulsed laser deposition. *J. Mater. Sci.* 2004, *39*, 2869–2871.

[52] Wu, J.; Gu, Q.; Guiton, B. S.; de Leon, N. P.; Ouyang, L.; Park, H. Strain-induced self organization of metal-insulator domains in single-crystalline VO2 nanobeams. *Nano Lett.* 2006, *6*, 2313–2317.

[53] Galy, J.; Miehe, G. Ab initio structures of (M2) and (M3) VO2 high pressure phases. *Solid State Sci.* 1999, *1*, 433–448.

[54] Guo, H.; Chen, K.; Oh, Y.; Wang, K.; Dejoie, C.; Syed Asif, S. A.; Warren, O. L.; Shan, Z. W.; Wu, J.; Minor, A. M. Mechanics and dynamics of the strain-induced M1–M2 structural phase transition in individual VO2 nanowires. *Nano Lett.* 2011, *11*, 3207–3213.

[55] Yang, H. W.; Sohn, J. I.; Yang, J. H.; Jang, J. E.; Cha, S. N.; Kim, J.; Kang, D. J. Unusual M2-mediated metal-insulator transition in epitaxial VO2 thin films on GaN substrates. *EPL* 2015, *109*, 27004.

[56] Quackenbush, N. F.; Paik, H.; Wahila, M. J.; Sallis, S.; Holtz, M. E.; Huang, X.; Ganose, A.; Morgan, B. J.; Scanlon, D. O.; Gu, Y.; Xue, F.; Chen, L.-Q.; Sterbinsky, G. E.; Schlueter, C.; Lee, T.-L.; Woicik, J. C.; Guo, J.-H.; Brock, J. D.; Muller, D. A.; Arena, D. A.; Schlom, D. G.; Piper, L. F. J. Stability of the M2 phase of vanadium dioxide induced by coherent epitaxial strain. *Phys. Rev. B* 2016, *94*, 085105.

[57] Shiga, D.; Minohara, M.; Kitamura, M.; Yukawa, R.; Horiba, K.; Kumigashira, H. Emergence of metallic monoclinic states of VO2 films induced by K deposition. *Phys. Rev. B* 2019, *99*, 125120.

[58] Laverock, J.; Jovic, V.; Zakharov, A. A.; Niu, Y. R.; Kittiwatanakul, S.; Westhenry, B.; Lu, J. W.; Wolf, S. A.; Smith, K. E. Observation of weakened V-V Dimers in the monoclinic metallic phase of strained VO2. *Phys. Rev. Lett.* 2018, *121*, 256403.

[59] Yang, M.; Yang, Y.; Hong, B.; Wang, L.; Hu, K.; Dong, Y.; Xu, H.; Huang, H.; Zhao, J.; Chen, H.; Song, L.; Ju, H.; Zhu, J.; Bao, J.; Li, X.; Gu, Y.; Yang, T.; Gao, X.; Luo, Z.; Gao, C. Suppression of structural phase transition in VO2 by epitaxial strain in vicinity of metal-insulator transition. *Sci. Rep.* 2016, *6*, 23119.

[60] Tselev, A.; Meunier, V.; Strelcov, E.; Shelton, W.; A Luk'yanchuk, I.; Jones, K.; Proksch, R.; Kolmakov, A.; Kalinin, S. Mesoscopic metal-insulator transition at ferroelastic domain walls in VO2. *ACS Nano* 2010, *4*, 4412–4419.

[61] Li, X.; Gloter, A.; Gu, H.; Cao, X.; Jin, P.; Colliex, C. Role of epitaxial microstructure, stress and twin boundaries in the metal–insulator transition mechanism in VO2/Al2O3 heterostructures. *Acta Mater.* 2013, *61*, 6443–6452.

[62] Marezio, M.; Dernier, P. D.; Santoro, A. Twinning in Cr-doped VO2. *Acta Cryst.* 1973, *A29*, 618–621.

[63] Fillingham, P. J. Domain structure and twinning in crystals of vanadium dioxide. *J. Appl. Phys.* 1967, *38*, 4823–4829.

[64] Li, J.; Gauntt, B. D.; Dickey, E. C. Microtwinning in highly nonstoichiometric VOx thin films. *Acta Mater.* 2010, *58*, 5009–5014.

[65] Yang, T.-H.; Aggarwal, R.; Gupta, A.; Zhou, H.; Narayan, R. J.; Narayan, J. Semiconductor-metal transition characteristics of VO2 thin films grown on c- and r-sapphire substrates. *J. Appl. Phys.* 2010, *107*, 053514.

[66] Zhao, Y.; Hwan Lee, J.; Zhu, Y.; Nazari, M.; Chen, C.; Wang, H.; Bernussi, A.; Holtz, M.; Fan, Z. Structural, electrical, and terahertz transmission properties of VO2 thin films grown on c-, r-, and m-plane sapphire substrates. *J. Appl. Phys.* 2012, *111*, 5, 053533.

[67] Nagashima, K.; Yanagida, T.; Tanaka, H.; Kawai, T. Stress relaxation effect on transport properties of strained vanadium dioxide epitaxial thin films. *Phys. Rev. B* 2006, *74*, 172106.

[68] Kawatani, K.; Kanki, T.; Tanaka, H. Formation mechanism of a microscale domain and effect on transport properties in strained VO2 thin films on TiO2(001). *Phys. Rev. B* 2014, *90*, 054203.

[69] Sohn, J. I.; Joo, H. J.; Ahn, D.; Lee, H. H.; Porter, A. E.; Kim, K.; Kang, D. J.; Welland, M. E. Surface-stress-induced Mott transition and nature of associated spatial phase transition in single crystalline VO2 nanowires. *Nano Lett.* 2009, *9*, 3392–3397.

[70] Liu, K.; Lee, S.; Yang, S.; Delaire, O.; Wu, J. Recent progresses on physics and applications of vanadium dioxide. *Mater. Today* 2018, *21*, 875–896.

[71] Scanlon, D. O.; Dunnill, C. W.; Buckeridge, J.; Shevlin, S. A.; Logsdail, A. J.; Woodley, S. M.; Catlow, C. R. A.; Powell, M. J.; Palgrave, R. G.; Parkin, I. P.; Watson, G. W.; Keal, T. W.; Sherwood, P.; Walsh, A.; Sokol, A. A. Band alignment of rutile and anatase TiO2. *Nat. Mater.* 2013, *12*, 798–801.

[72] https://www.shinkosha.com/english/product/epi_substrate/epi_substrate_03/

[73] https://www.mtixtl.com/xtlflyers/TO.pdf

[74] Sandim, H.; Santos, C.; Suzuki, P.; Otero, M.; Padilha, A. Electrical resistivity of an oxide dispersion strengthened niobium alloy (Nb-0.5 wt%TiO2-ODS). *Int. J. Refract. Met. Hard Mater.* 1998, 16, 143–147.

[75] Wrana, D.; Rodenbücher, C.; Krawiec, M.; Jany, B. R.; Rysz, J.; Ermrich, M.; Szot, K.; Krok, F. Tuning the surface structure and conductivity of niobium-doped rutile TiO2 single crystals via thermal reduction. *Phys. Chem. Chem. Phys.* 2017, *19*, 30339–30350.

[76] Martens, K.; Aetukuri, N.; Jeong, J.; Samant, M. G.; Parkin, S. S. P. Improved metal-insulator-transition characteristics of ultrathin VO2 epitaxial films by optimized surface preparation of rutile TiO2 substrates. *Appl. Phys. Lett.* 2014, *104*, 081918.

[77] Fan, L. L.; Chen, S.; Wu, Y. F.; Chen, F. H.; Chu, W. S.; Chen, X.; Zou, C. W.; Wu, Z. Y. Growth and phase transition characteristics of pure M-phase VO2 epitaxial film prepared by oxide molecular beam epitaxy. *Appl. Phys. Lett.* 2013, *103*, 131914.

[78] Benmoussa, M.; Ibnouelghazi, E.; Bennouna, A.; Ameziane, E. Structural, electrical and optical properties of sputtered vanadium pentoxide thin films. *Thin Solid Films* 1995, *265*, 22–28.

[79] Zaumseil, P. High-resolution characterization of the forbidden Si 200 and Si 222 reflections. *J. Appl. Crystallogr.* 2015, *48*, 528–532.

[80] Hwang, B.-H. Calculation and measurement of all (002) multiple diffraction peaks from a (001) silicon wafer. *J. Phys. D: Appl. Phys.* 2001, *34*, 2469–2474.

[81] Ko, C.; Yang, Z.; Ramanathan, S. Work Function of Vanadium Dioxide Thin Films Across the Metal-Insulator Transition and the Role of Surface Nonstoichiometry. *ACS Appl. Mater. Interfaces* 2011, *3*, 3396–3401.

[82] Beke, S.; Giorgio, S.; Kőrösi, L.; Nánai, L.; Marine, W. Structural and optical properties of pulsed laser deposited V2O5 thin films. *Thin Solid Films* 2008, *516*, 4659–4664.

[83] Komar, P.; Jakob, G. CADEM: calculate X-ray diffraction of epitaxial multilayers. *J. Appl. Crystallogr.* 2017, *50*, 288–292.

[84] Jen, S.-H.; Bertrand, J. A.; George, S. M. Critical tensile and compressive strains for cracking of Al2O3 films grown by atomic layer deposition. *J. Appl. Phys.* 2011, *109*, 084305.

[85] Thouless, M. D. Crack Spacing in Brittle Films on Elastic Substrates. *J. Am. Ceram. Soc.* 1990, *73*, 2144–2146.

[86] Goehring, L.; Morris, S. W. Cracking mud, freezing dirt, and breaking rocks. *Phys. Today* 2014, *67*, 39–44.

[87] Miedema, M. Mud-crack pattern evolution in iterated drying cycles. Department of Physics, University of Toronto, 2015.

[88] *The Merck Index - An Encyclopedia of Chemicals, Drugs, and Biologicals*. O'Neil, M. J. ed.; Royal Society of Chemistry: Cambridge, UK, 2013, p. 1841.

[89] Gregg, J. M.; Bowman, R. M. The effect of applied strain on the resistance of VO2 thin films. *Appl. Phys. Lett.* 1997, *71*, 3649–3651.

[90] Kittiwatanakul, S.; Wolf, S. A.; Lu, J. Large epitaxial bi-axial strain induces a Mott-like phase transition in VO2. *Appl. Phys. Lett.* 2014, *105*, 073112.

[91] Cui, Y.; Ramanathan, S. Substrate effects on metal-insulator transition characteristics of rf-sputtered epitaxial VO2 thin films. *J. Vac. Sci. Technol. A* 2011, *29*, 041502.

[92] Nakano, M.; Shibuya, K.; Okuyama, D.; Hatano, T.; Ono, S.; Kawasaki, M.; Iwasa, Y.; Tokura, Y. Collective bulk carrier delocalization driven by electrostatic surface charge accumulation. *Nature* 2012, *487*, 459–462.

[93] Lee, D.; Chung, B.; Shi, Y.; Kim, G.-Y.; Campbell, N.; Xue, F.; Song, K.; Choi, S.-Y.; Podkaminer, J. P.; Kim, T. H.; Ryan, P. J.; Kim, J.-W.; Paudel, T. R.; Kang, J.-H.; Spinuzzi, J. W.; Tenne, D. A.; Tsymbal, E. Y.; Rzchowski, M. S.; Chen, L. Q.; Lee, J.; Eom, C. B. Isostructural metal-insulator transition in VO2. *Science* 2018, *362*, 1037–1040.

[94] Matthews, J.; Blakeslee, A. Defects in epitaxial multilayers: I. Misfit dislocations. *J. Cryst. Growth* 1974, *27*, 118–125.

[95] McWhan, D. B.; Marezio, M.; Remeika, J. P.; Dernier, P. D. X-ray diffraction study of metallic VO2. *Phys. Rev. B* 1974, *10*, 490–495.

[96] Andersson, G. Studies on vanadium oxides. II. The Crystal Structure of Vanadium Dioxide. *Acta Chem. Scand.* 1956, *10*, 623–628.

[97] Huang, Y.; Zhang, L.; Guo, T.; Hwang, K.-C. Mixed mode near-tip fields for cracks in materials with strain-gradient effects. *J. Mech. Phys. Solids*, **1997**, *45*, 439 – 465.

[98] Catalan, G.; Bowman, R.; Gregg, J. Metal-insulator transitions in NdNiO3 thin films. *Phys. Rev. B* 2000, *62*, 7892.

[99] Abbate, M.; de Groot, F. M. F.; Fuggle, J. C.; Ma, Y. J.; Chen, C. T.; Sette, F.; Fujimori, A.; Ueda, Y.; Kosuge, K. Soft-x-ray-absorption studies of the electronic-structure changes through the VO2 phase transition. *Phys. Rev. B* 1991, *43*, 7263–7266.

[100] Gray, A. X.; Jeong, J.; Aetukuri, N. P.; Granitzka, P.; Chen, Z.; Kukreja, R.; Higley, D.; Chase, T.; Reid, A. H.; Ohldag, H.; Marcus, M. A.; Scholl, A.; Young, A. T.; Doran, A.; Jenkins, C. A.; Shafer, P.; Arenholz, E.; Samant, M. G.; Parkin, S. S. P.; Dürr, H. A. Correlation-driven insulator-metal transition in near-ideal vanadium dioxide films. *Phys. Rev. Lett.* 2016, *116*, 116403.

[101] Koethe, T. C.; Hu, Z.; Haverkort, M. W.; Schüßler-Langeheine, C.; Venturini, F.; Brookes, N. B.; Tjernberg, O.; Reichelt, W.; Hsieh, H. H.; Lin, H.-J.; Chen, C. T.; Tjeng, L. H. Transfer of Spectral Weight and Symmetry across the Metal-Insulator Transition in VO2. *Phys. Rev. Lett.* 2006, *97*, 116402.

[102] Palermo, V.; Palma, M.; Samorì, P. Electronic Characterization of Organic Thin Films by Kelvin Probe Force Microscopy. In *Scanning Probe Microscopies Beyond Imaging*; P. Samorì ed.; Wiley-VCH, 2006; pp 390–429.

[103] Villeneuve-Faure, C.; Makasheva, K.; Boudou, L.; Teyssedre G. Space Charge at Nanoscale: Probing Injection and Dynamic Phenomena Under Dark/Light Configurations by Using KPFM and C-AFM. In *Electrical Atomic Force Microscopy for Nanoelectronics*; U. Celano ed.; Springer, 2019, pp 267–301.

[104] Kaja, K. Development of nano-probe techniques for work function assessment and application to materials for microelectronics. Ph.D. Thesis, Université Joseph-Fourier, France, 2010.

[105] Sohn, A.; Kanki, T.; Tanaka, H.; Kim, D.-W. Visualization of local phase transition behaviors near dislocations in epitaxial VO2/TiO2 thin films. *Appl. Phys. Lett.* 2015, *107*, 171603.

[106] Sohn, A.; Kim, H.; Kim, D.-W.; Ko, C.; Ramanathan, S.; Park, J.; Seo, G.; Kim, B.-J.; Shin, J.-H.; Kim, H.-T. Evolution of local work function in epitaxial VO2 thin films spanning the metal-insulator transition. *Appl. Phys. Lett.* 2012, *101*, 191605.

[107] Sohn, A.; Kanki, T.; Sakai, K.; Tanaka, H.; Kim, D.-W. Fractal Nature of Metallic and Insulating Domain Configurations in a VO2 Thin Film Revealed by Kelvin Probe Force Microscopy. *Sci. Rep.* 2015, *5*, 10417.

[108] Salje, E. K. H.; Xue, D.; Ding, X.; Dahmen, K. A.; Scott, J. F. Ferroelectric switching and scale invariant avalanches in BaTiO3. *Phys. Rev. Mater.* 2019, *3*, 014415.

[109] Casals, B.; van Dijken, S.; Herranz, G.; Salje, E. K. H. Electric-field-induced avalanches and glassiness of mobile ferroelastic twin domains in cryogenic SrTiO3. *Phys. Rev. Res.* 2019, *1*, 032025.

[110] Stefanovich, G.; Pergament, A.; Stefanovich, D. Electrical switching and Mott transition in VO2. *J. Phys.: Condens. Matter* 2000, *12*, 8837.

[111] Chen, F.H.; Fan, L. L.; Chen, S.; Liao, G. M.; Chen, Y. L.; Wu, P.; Song, L.; Zou, C. W.; Wu, Z. Y. Control of the metal–insulator transition in VO2 epitaxial film by modifying carrier density. *ACS Appl. Mater. Inter.* 2015, *7*, 6875–6881.

[112] Ruzmetov, D.; Gopalakrishnan, G.; Deng, J.; Narayanamurti, V.; Ramanathan, S. Electrical triggering of metal-insulator transition in nanoscale vanadium oxide junctions. *J. Appl. Phys.* 2009, *106*, 083702.

[113] Chae, B.-G.; Kim, H.-T.; Youn, D.-H.; Kang, K.-Y. Abrupt metal–insulator transition observed in VO2 thin films induced by a switching voltage pulse. *Physica B* 2005, *369*, 76–80.

[114] Li, Z.; Wu, J.; Hu, Z.; Lin, Y.; Chen, Q.; Guo, Y.; Liu, Y.; Zhao, Y.; Peng, J.; Chu, W.; Wu, C.; Xie, Y. Imaging metal-like monoclinic phase stabilized by surface coordination effect in vanadium dioxide nanobeam. *Nat. Commun.* 2017, *8*, 15561.

[115] Zhou, Y.; Ha, S. D.; Ramanathan, S. Computation and learning with metal-insulator transitions and emergent phases in correlated oxides. In *Cmos and Beyond: Logic Switches For Terascale Integrated Circuits*; Liu, T.-J. K., Kuhn, K. eds.; Electronic, optoelectronic devices, and nanotechnology; Cambridge Univ. Press: Cambridge, 2015; pp 209–235.

[116] Nam, K. H.; Park, I.H.; Ko, S. H. Patterning by controlled cracking. *Nature* 2012, *485*, 221.

[117] Shklover, V.; Haibach, T.; Ried, F.; Nesper, R.; Novák, P. Crystal Structure of the Product of Mg2+ Insertion into V2O5 Single Crystals. *J. Solid State Chem.* 1996, *123*, 317–323.

[118] Kawada, I.; Ishii, M.; Saeki, M.; Kimizuka, N.; Nakano-Onoda, M.; Kato, K. Structural re-investigation of the low-temperature phase of V6O13. *Acta Cryst.* 1978, B*34*, 1037–1039.

[119] Åsbrink, S. The crystal structure of and valency distribution in the low-temperature modification of V3O5. The decisive importance of a few very weak reflexions in a crystal-structure determination. *Acta Cryst.* 1980, B*36*, 1332–1339.

[120] Abrahams, S. C.; Bernstein, J. L. Rutile: Normal Probability Plot Analysis and Accurate Measurement of Crystal Structure. *J. Chem. Phys.* 1971, *55*, 3206–3211.

[121] Okrusch, M.; Hock, R.; Schüssler, U.; Brummer, A.; Baier, M.; Theisinger, H. Intergrown niobian rutile phases with Sc- and W-rich ferrocolumbite: An electron-microprobe and Rietveld study. *Am. Mineral.* 2003, *88*, 986–995.

[122] Shin, J.-Y.; Joo, J. H.; Adepalli, K. K.; Samuelis, D.; Maier, J. The effects of n-type doping on lithium storage in TiO2. *Phys. Chem. Chem. Phys.* 2016, *18*, 8963–8970.

[123] Schierle, E. Antiferromagnetism in thin films studied by resonant magnetic soft x-ray scattering. PhD thesis. Freie Universität Berlin, Germany, 2007.